© 2018 by Amartya Bose. All rights reserved.

PHASE SPACE AND PATH INTEGRAL APPROACHES TO QUANTUM DYNAMICS

BY

AMARTYA BOSE

DISSERTATION

Submitted in partial fulfillment of the requirements
for the degree of Doctor of Philosophy in Chemistry
in the Graduate College of the
University of Illinois at Urbana-Champaign, 2018

Urbana, Illinois

Doctoral Committee:

Professor Nancy Makri, Chair
Professor Martin Gruebele
Professor So Hirata
Research Assistant Professor Lucas Wagner

Abstract

Exact quantum dynamical simulation of processes in highly coupled condensed phase reactions is extremely challenging. The work reported in this dissertation builds on top of two different approaches. First, we present methods for calculating the multidimensional Wigner function. We start with a simple and approximate method which utilizes classical trajectories. This fits well with the subsequent classical propagation involved in a quasiclassical simulation. We use this method to study molecular Hamiltonians in both normal mode and Cartesian coordinates. Despite the simplicity of this method, there can be systems which are extremely anharmonic, where the method can be extremely slow to converge when there is no obviously good starting point. To overcome this problem, we propose a numerically exact path integral based method which can be systematically converged to any desired level of accuracy at increasing computational cost. Both these methods can be used with quantum classical simulation frameworks.

Second, we present developments of rate theory methods. We extend the existing reactive flux rate methods to exact quantum classical methods. Two different initial conditions are proposed. If the transients are important, we show that the so-called "non-equilibrium" initial condition can help us unify the fast timescales as well as the long timescale dynamics governed by the rate. On the other hand, if the transients are of less importance, we propose a "near equilibrium" initial condition that can very effectively get rid of most of the transients. This initial condition captures the system-solvent interaction without increasing the complexity of the algorithm.

Finally, we present a method of incorporating the concept of blip summation into the quantum-classical path integral (QCPI) method. This gives additional speedup on top of all the other advancements that make QCPI a very attractive method for doing exact quantum dynamics in condensed phase.

This work is dedicated to the memory of my grandparents, Santwana Sen and Somesh Sen.

Acknowledgements

Research is not something that can either be learnt all by oneself or done all alone. The work reported in this dissertation could not have been done without the support and guidance of Professor Nancy Makri. It has been a huge honour for me to have spent these years working with her and learning from her, not just in a course setting. She has taught me how to think about the field, how to formulate problems and search for their answers. I do hope to be able to learn more from her in the future and imbibe some of the scientific spirit and outlook that she has taught me over numerous discussions.

I would like to thank Professor Martin Gruebele for the opportunity to do undergraduate research with him over a summer. Taking courses from him and talking to him about science are some of the things that I will remember. I have learned a lot from his infectious enthusiasm and piercing insight into a wide range of scientific disciplines. Professor So Hirata was instrumental in getting me interested in electronic structure theory. I would also like to thank Professor Lucas Wagner for agreeing to be on my committee at the eleventh hour. I would not have been here were it not for the environment that I received at IITK. I would like to thank Professor K. Srihari for being sources of encouragement. I am especially indebted to Professor Debabrata Goswami for introducing me to the wonderful world of research in general and spectroscopy in particular.

I have had the pleasure of overlapping with many people in the Makri group over the years. It has been a very fun journey. I remember the extensive discussions with Peter Walters, Thomas Allen, Tuseeta Banerjee and Sambarta Chatterjee on science and basically everything under the sun. Over the past year it has been great getting to know Jessi Hartman, Sohang Kundu and Reshmi Dani. Jacob Faucheaux and I started our graduate school journeys together, sharing TA-duties and classes. Somewhere down the way, our friendship became strong enough that we knew that we could share our joys and frustrations and depend on the other to help keep us sane. This entire journey would not have been possible without the friendship of all of these people.

Though I tend to be a loner most of the times, I have been extremely lucky to find great friends. Undergraduate days would have been well nigh impossible to bear were it not for Arnab, Shubhayu, Raziman, Lohani and Sid. We have shared a lot of our formative years together. They continue to support me through a lot even today. I would in particular like to thank Shayak. I know we have not really been great at keeping in touch of late, but I am sure we'll get better. It is funny how friendships are formed. Since first meeting her through Shubhayu, Lagnojita has become a good friend. How boring would these days be without being able to give her hell for being perpetually busy, even when she is not! On a more serious note, I would like to thank her for all the random discussions. Such friends are

hard to find.

None of this would have been possible without the love, support and blessings of my family, my parents Sudeshna Bose, Amarnath Bose and my brother Aditya Bose. It is my parents' encouragement and advice that has paved the way for me. The past decade that I have been away from home would not have been nearly as successful had it not been for their help and innumerable sacrifices. What began as extremely long phone calls from my college in 2007 and has transformed into the daily hour long video calls home today has kept me going despite distances. (When you are almost half the world away from your family, it makes you wonder if the technology that connects you to them doesn't deserve just as much gratitude. However I shall refrain from thanking the machines, for they are only that after all, aren't they?)

Table of Contents

List of Figures

List of Tables

List of Abbreviations

AS	Adiabatic switching
ASW	Adiabatic switching Wigner function
PES	Potential energy surface
PIMC	Path integral Monte Carlo
PI-Wigner	Path integral Wigner method
QCPI	Quantum-classical path integral
HBR	Harmonic Back Reaction
bQCPI	Blip-summed quantum-classical path integral
QuAPI	Quasi-adiabatic path integral
TLS	Two-level system
WKB	Wentzel-Kramers-Brillouin approximation
ZPE	Zero-point energy

Chapter 1

Background and introduction

> The underlying physical laws necessary for the mathematical theory of a large part of physics and the whole of chemistry are thus completely known, and the difficulty is only that the exact application of these laws leads to equations much too complicated to be soluble. It therefore becomes desirable that approximate practical methods of applying quantum mechanics should be developed, which can lead to an explanation of the main features of complex atomic systems without too much computation.
>
> *P. A. M. Dirac, 1929*[1]

Quantum mechanics, as the set of physical laws behind chemistry, has been well understood since the first half of the last century. In fact, aspects of this theory are simpler than its elder sibling, classical mechanics. Quantum physics is a linear theory and therefore does not show chaotic dynamics, which can lead to numerical instabilities in simulations. The problem with simulations of microscopic particles lies in the fact that quantum dynamics shows an exponential growth with the number of dimensions.

This has led to a huge proliferation of approximate methods, both analytical and numerical. The large dimensionality of condensed phase problems, that is the bane of quantum dynamics, also happens to provide a saving grace. Generally, when many uncorrelated degrees of freedom interact, the average result washes away fine details and can often be well represented by Gaussian processes. This is formally expressed as the central limit theorem and the key observation behind the so-called linear response family of approximations. One of the most famous applications of the linear response approximation[2] is the Marcus theory[3,4] for electron transfer in solvents. The other simplifying observation is that when describing thermal processes in condensed phase systems, fine quantum effects like interference and coherence are washed away, leaving behind dynamics that is mostly classical, with "minor" corrections from quantum mechanics. Of course, this is not the entire story. There are tunneling processes, which are only describable through quantum mechanics, and there can be processes like superfluidity and superconductivity, which are macroscopic manifestations of quantum mechanical phenomena. The latter, being a different domain of research with its own sophisticated methods and set of approximations, is beyond the scope of the current work. However, we need to be able to account for tunneling. It is the basis of all bond breaking and making, and consequently all of chemistry.

The understanding that classically forbidden processes like tunneling occur only in a very small dimensional

subspace of the space spanned by all the degrees of freedom, allows for development of methods based on the idea of system-solvent separation. The low dimensional system is treated at some level of quantum mechanics, whereas the high dimensional solvent (constituted by all the degrees of freedom left over after defining the system) is treated using classical trajectories. This makes it feasible to get accurate dynamical information about the system despite the presence of a condensed phase environment. We will differentiate between two ways of treating the environment: using classical mechanics, which uses the idea that most of the dynamics in condensed phase is classical, or through a harmonic bath utilizing linear response. The latter allows for exact quantum mechanical solutions,[5–8] whereas the former allows for approximate treatment of the solvent beyond the linear response regime. There are various numerical methods which study the dynamics of a quantum system in a classical solvent.[9–12] In this work, we would focus solely on the quantum-classical path integral method (QCPI),[13–17] which is a rigorous method that under convergence treats the interaction between the quantum system and the classical solvent without any approximations.

The solvent or the environment (both the terms are used interchangeably in this thesis) is made up of quantum mechanical atoms. Yet, as we mentioned, most of the quantum mechanics is washed away in a thermal process. The emergence of classical phenomena out of quantum mechanics has been a topic of intense study over the years. The path integral representation of quantum mechanics[18,19] is an especially useful starting point because it shares the common language of paths with classical mechanics. Instead of just considering the subset of paths with stationary action[20] (expressed by the Euler-Lagrange equation), path integral quantum mechanics associates a complex amplitude of unit norm with every path. Processes are described as a sum over the amplitudes of *all* the paths. This now allows us to understand the classical limit of quantum mechanics in a simpler manner. When Planck's constant is smaller than the scales relevant to the physics, almost all paths but the classical trajectories have wildly fluctuating phases. They cancel each other thus giving dynamics which is adequately represented by the classical trajectories.

However despite the classical nature of the dynamics of the solvent, there are minor corrections from quantum mechanics which are needed to make the classical description of the solvent degrees of freedom acceptable. These corrections stem from zero-point energy (ZPE) and non-negligible effects of quantum dispersion. Isotope effect, for instance, is a result of change of ZPE because of the mass of the particle. There are Monte Carlo based methods for exactly calculating the thermal density matrix of a multidimensional system. However, that lacks a full phase space description, and cannot therefore be used for launching classical trajectories. The rigorous method of deriving this form of mechanics which incorporates quantum effects in classical trajectories is done by taking the explicit limit of small $\hbar$ and is called semiclassical dynamics. Van Vleck[21] first proposed a form for the semiclassical propagator in coordinate space as a boundary value problem in 1928. The expression was later modified to handle caustics by Gutzwiller.[22] A different semiclassical expression was proposed by Herman and Kluk.[23] Miller[24] demonstrated the equivalence of the two at the semiclassical level by deriving the Herman-Kluk propagator from the Van Vleck propagator by applying the modified Filinov filtering procedure. A subsequent linearization of the difference between the forward and backward paths of time propagation of a density matrix leads to a form where the dynamics is exactly classical, but the starting distribution is a phase space representation of the quantum density matrix called the Wigner function.[25–27] This however is not the only way of deriving the Wigner function, which is a different representation of quantum mechanics. It is possible to do full quantum mechanics using the Wigner function as the starting pos-

tulate, with equations of motion called the Moyal series.[28] Classical mechanics can be shown to be the first order truncation of the infinite Moyal series. The quasiclassical dynamics stemming therefrom is variously called Wigner method[29] or linearized semiclassical dynamics.[27,30,31] This Wigner distribution is represented as a multidimensional Fourier transform of the operator in question, the density matrix in this case. Thus, the problem of calculating the Wigner transform is, in general, intractible in multiple dimensions. There are a variety of methods for approximating the Wigner distribution,[26,32–34] none of which can be systematically improved. In Part I, we present two methods for calculating the Wigner function. The first method described in Chapter 2 is approximate and very simple. It is based on classical trajectories, which makes it especially attractive for the subsequent classical propagation. We explore some interesting properties of this resultant distribution, which we call the adiabatic switching Wigner (ASW) distribution and show how to apply it to study molecular systems described by Hamiltonians in normal mode and Cartesian coordinates. The second method, reported in Chapter 5 is a numerically exact method, where we have developed a path integral based Monte Carlo technique to estimate the Wigner function. This does not suffer as badly from the "sign" problem as a naïve Monte Carlo procedure would while evaluating the required Fourier transform.

In Part II, we return to the system-solvent decomposition and exact quantum dynamics. Recent work on QCPI has substantially improved the scaling of the algorithm. While it is increasingly becoming possible to directly simulate ultrafast dynamics with relative ease, tackling "slow" chemical reactions in sluggish media still proves to be challenging with very long non-Markovian memories. For many of these very slow reactions, the early transients in the dynamics are unimportant, and these reactions are well characterized by the single rate constant. In fact, rate theories have been a cornerstone of chemistry since very early days. The quest to calculate the rate of reactions has been a long standing one starting with the Arrhenius equation. There have been extremely successful approximations over the years. Very early on there were the transition state theories of classical mechanics,[25,35] Fermi's Golden Rule and Redfield equations. Marcus theory[3,4] for rates of electron transfer in solvents is an extremely powerful and widely used perturbative expression for the short time rate. In processes where transients have an impact, this rate could be different from the true time scales. Generally rate is governed by the characteristic time scale of the post-transient exponential decay to equilibrium. Possibly one of the first fully quantum rate theory was given by Miller.[36] It relates the rate with various quantum correlation functions involving the flux operator.[37] Since calculating these correlation functions exactly is difficult, various semiclassical approximations were developed.[30,36,38–45] Topaler and Makri[46] have developed an exact complex-time method for calculating this correlation function and consequently the exact rate for a two-level system coupled with a harmonic bath.

So, the logical next step is to use QCPI to calculate the exact quantum rate for an atomistic solvent. This proves to be problematic since we need to calculate the equilibrium of a quantum system described by a coordinate space representation interacting with a solvent described by the quasi-classical phase space. In Chapter 6, we show how it is possible to side-step this issue, and in the process develop a method that can retain information about the transients, which can be important in case of ultrafast reactions where the timescales are not well separated. Then in Chapter 7 we explore other possibilities for calculating the rate more efficiently. Both these methods can be used with QCPI and applied to atomistic solvents. New method developments involving the path integral based Wigner function method are still in progress. These developments would make it possible not only to calculate the rate but any arbitrary

correlation function with QCPI.

With all these developments, it is easy to forget that the efficiency is still, to a large extent, governed by the base on which everything else is built — in this case QCPI. If we can speed up QCPI, then we automatically speed up both the direct dynamics and the rate methods. In the final chapter, based on developments not reported in this thesis, we show the possibility of enhancing QCPI with a new reformulation called blip summation, first implemented by Makri.[47–50] Previous developments have already made QCPI a very attractive method for doing exact quantum dynamics. This incorporation of blip summations makes it even more viable, while keeping all the benefits intact.

References

[1] P. A. M. Dirac, "Quantum Mechanics of Many-Electron Systems", Proc. R. Soc. London A Math. Phys. Eng. Sci. **123**, 714–733 (1929).

[2] N. Makri, "The Linear Response Approximation and Its Lowest Order Corrections: An Influence Functional Approach", J. Phys. Chem. B **103**, 2823–2829 (1999).

[3] R. A. Marcus, "Theory of electron-transfer reaction rates of solvated electrons", J. Chem. Phys. **43**, 3477–3489 (1965).

[4] R. A. Marcus, "On the Theory of Electron-Transfer Reactions. VI. Unified Treatment for Homogeneous and Electrode Reactions", J. Chem. Phys. **43**, 679–701 (1965).

[5] D. E. Makarov and N. Makri, "Tunneling dynamics in dissipative curve-crossing problems", Phys. Rev. A **48**, 3626–3635 (1993).

[6] D. E. Makarov and N. Makri, "Path integrals for dissipative systems by tensor multiplication. Condensed phase quantum dynamics for arbitrarily long time", Chem. Phys. Lett. **221**, 482–491 (1994).

[7] N. Makri and D. E. Makarov, "Tensor propagator for iterative quantum time evolution of reduced density matrices. I. Theory", J. Chem. Phys. **102**, 4600–4610 (1995).

[8] N. Makri and D. E. Makarov, "Tensor propagation for iterative quantum time evolution of reduced density matrices. II. Numerical methodology", J. Chem. Phys. **102**, 4611–4618 (1995).

[9] M. H. Beck, A. Jäckle, G. A. Worth, and H.-D. Meyer, "The multiconfiguration time-dependent Hartree (MCTDH) method: a highly efficient algorithm for propagating wavepackets", Phys. Rep. **324**, 1–105 (2000).

[10] J. C. Tully and R. K. Preston, "Trajectory surface hopping approach to nonadiabatic molecular collisions: The reaction of H^+ with D_2", J. Chem. Phys. **55**, 562–572 (1971).

[11] D. S. Sholl and J. C. Tully, "A generalized surface hopping method", J. Chem. Phys. **109**, 7702–7710 (1998).

[12] J. R. Schmidt, P. V. Parandekar, and J. C. Tully, "Mixed quantum-classical equilibrium: Surface hopping", J. Chem. Phys. **129**, 044104 (2008).

[13] R. Lambert and N. Makri, "Quantum-classical path integral. I. Classical memory and weak quantum nonlocality", J. Chem. Phys. **137**, 22A552 (2012).

[14]R. Lambert and N. Makri, "Quantum-classical path integral. II. Numerical methodology", J. Chem. Phys. **137**, 22A553 (2012).

[15]T. Banerjee and N. Makri, "Quantum-classical path integral with self-consistent solvent-driven reference propagators", J. Phys. Chem. B **117**, 13357–13366 (2013).

[16]P. L. Walters and N. Makri, "Iterative quantum-classical path integral with dynamically consistent state hopping", J. Chem. Phys. **144**, 044108 (2016).

[17]P. L. Walters and N. Makri, "Quantum-Classical Path Integral Simulation of Ferrocene-Ferrocenium Charge Transfer in Liquid Hexane", J. Phys. Chem. Lett. **6**, 4959–4965 (2015).

[18]R. P. Feynman, "Space-time approach to non-relativistic quantum mechanics", Rev. Mod. Phys. **20**, 367–387 (1948).

[19]R. P. Feynman, A. R. Hibbs, and D. F. Styer, *Quantum Mechanics and Path Integrals* (Dover Publications, 2010), p. 384.

[20]H. Goldstein, C. P. Poole, and J. L. Safko, *Classical Mechanics* (Addison Wesley, 2002).

[21]J. H. Van Vleck, "The Correspondence Principle in the Statistical Interpretation of Quantum Mechanics", Proc. Natl. Acad. Sci. U. S. A. **14**, 178–188 (1928).

[22]M. C. Gutzwiller, "Periodic orbits and classical quantization conditions", J. Math. Phys. **12**, 343–358 (1971).

[23]M. F. Herman and E. Kluk, "A semiclasical justification for the use of non-spreading wavepackets in dynamics calculations", Chem. Phys. **91**, 27–34 (1984).

[24]W. H. Miller, "An alternate derivation of the Herman-Kluk (coherent state) semiclassical initial value representation of the time evolution operator", in Mol. phys. Vol. 100, 4 (Feb. 2002), pp. 397–400.

[25]E. Wigner, "Calculation of the Rate of Elementary Association Reactions", J. Chem. Phys. **5**, 720–725 (1937).

[26]J. A. Poulsen, G. Nyman, and P. J. Rossky, "Practical evaluation of condensed phase quantum correlation functions: A Feynman-Kleinert variational linearized path integral method", J. Chem. Phys. **119**, 12179–12193 (2003).

[27]W. Miller, "Generalization of the linearized approximation to the semiclassical initial value representation for reactive flux correlation functions", J. Phys. Chem. A **103**, 9384–9387 (1999).

[28]J. E. Moyal and M. S. Bartlett, "Quantum mechanics as a statistical theory", Math. Proc. Cambridge Philos. Soc. **45**, 99 (1949).

[29]E. J. Heller and R. C. Brown, "Errors in the Wigner Approach to Quantum Dynamics", J. Chem. Phys. **75**, 1048–1050 (1981).

[30]H. Wang, X. Sun, and W. H. Miller, "Semiclassical approximations for the calculation of thermal rate constants for chemical reactions in complex molecular systems", J. Chem. Phys. **108**, 9726–9736 (1998).

[31]X. Sun, H. Wang, and W. H. Miller, "Semiclassical theory of electronically nonadiabatic dynamics: Results of a linearized approximation to the initial value representation", J. Chem. Phys. **109**, 7064–7074 (1998).

[32]Q. Shi and E. Geva, "Semiclassical Theory of Vibrational Energy Relaxation in the Condensed Phase", J. Phys. Chem. A **107**, 9059–9069 (2003).

[33]P. Frantsuzov, A. Neumaier, and V. A. Mandelshtam, "Gaussian resolutions for equilibrium density matrices", Chem. Phys. Lett. **381**, 117–122 (2003).

[34]P. A. Frantsuzov and V. A. Mandelshtam, "Quantum statistical mechanics with Gaussians: Equilibrium properties of van der Waals clusters", J. Chem. Phys. **121**, 9247–9256 (2004).

[35]P. Pechukas, "Transition State Theory", Annu. Rev. Phys. Chem. **32**, 159–177 (1981).

[36]W. H. Miller, "Quantum mechanical transition state theory and a new semiclassical model for reaction rate constants", J. Chem. Phys. **61**, 1823 (1974).

[37]W. H. Miller, S. D. Schwartz, and J. W. Tromp, "Quantum mechanical rate constants for bimolecular reactions", J. Chem. Phys. **79**, 4889–4898 (1983).

[38]H. Wang, W. H. Thompson, and W. H. Miller, ""Direct" Calculation of Thermal Rate Constants for the F + H 2 → HF + F Reaction", J. Phys. Chem. A **102**, 9372–9379 (1998).

[39]C. Venkataraman and W. H. Miller, "The Quantum Instanton (QI) Model for Chemical Reaction Rates: The "Simplest" QI with One Dividing Surface †", J. Phys. Chem. A **108**, 3035–3039 (2004).

[40]C. Venkataraman and W. H. Miller, "Chemical reaction rates using the semiclassical Van Vleck initial value representation", J. Chem. Phys. **126**, 094104 (2007).

[41]W. H. Miller, "Spiers Memorial Lecture Quantum and semiclassical theory of chemical reaction rates", Faraday Discuss. **110**, 1–21 (1998).

[42]T. Yamamoto, H. Wang, and W. H. Miller, "Combining semiclassical time evolution and quantum boltzmann operator to evaluate reactive flux correlation function for thermal rate constants of complex systems", J. Chem. Phys. **116**, 7335–7349 (2002).

[43]Y. Zhao and W. H. Miller, "Semiclassical initial value representation for the Boltzmann operator in thermal rate constants", J. Chem. Phys. **117**, 9605–9610 (2002).

[44]T. Yamamoto and W. H. Miller, "Semiclassical calculation of thermal rate constants in full Cartesian space: The benchmark reaction $D + H_2 \rightarrow DH + H$", J. Chem. Phys. **118**, 2135–2152 (2003).

[45]X. Sun, H. Wang, and W. H. Miller, "On the semiclassical description of quantum coherence in thermal rate constants", J. Chem. Phys. **109**, 4190–4200 (1998).

[46]M. Topaler and N. Makri, "Quantum rates for a double well coupled to a dissipative bath: Accurate path integral results and comparison with approximate theories", J. Chem. Phys. **101**, 7500–7519 (1994).

[47]N. Makri, "Exploiting classical decoherence in dissipative quantum dynamics: Memory, phonon emission, and the blip sum", Chem. Phys. Lett. **593**, 93–103 (2014).

[48]N. Makri, "Blip decomposition of the path integral: Exponential acceleration of real-time calculations on quantum dissipative systems", J. Chem. Phys. **141**, 134117 (2014).

[49]N. Makri, "Blip-summed quantum–classical path integral with cumulative quantum memory", Faraday Discuss. **195**, 81–92 (2016).

[50]N. Makri, "Iterative blip-summed path integral for quantum dynamics in strongly dissipative environments", J. Chem. Phys. **146**, 134101 (2017).

Part I

Wigner function

Chapter 2

Wigner phase space distribution via classical adiabatic switching

2.1 Introduction

This chapter is based on the paper, A. Bose and N. Makri, "Wigner phase space distribution via classical adiabatic switching", J. Chem. Phys. **143**, 114114 (2015).

Quantum mechanical simulation of the time evolution of condensed phase and biological systems is infeasible due to the computational cost scaling exponentially with the degrees of freedom. Classical molecular dynamics simulations provide a simple and computationally efficient alternative for doing such computations using Newtonian trajectories. The major corrections to classical dynamics calculations in large systems typically arise from quantization of the initial density matrix and, in many cases, nonadiabatic effects, usually associated with transitions among Born-Oppenheimer states. Quantum coherence effects, which are extremely important in small systems, are usually washed out in large biological molecules or in processes occurring in liquid environments. Quantization of the initial density matrix is necessary when the zero-point energy (ZPE) is not negligible and quantum dispersion leads to distributions that differ substantially from the Boltzmann function. In order to capture the system's dynamics via classical trajectories, the quantized density matrix needs to be converted to a phase space function. There are two similar methods for performing such calculations: the linearized semiclassical initial value representation[2–4] (which is also known as the Wigner method[5,6] and which has been derived by linearizing the path integral expression[7]), where a phase space function is obtained via the Wigner transform of the initial density, and forward-backward semiclassical dynamics[8–10] (FBSD), where the phase space function is given by the coherent state transform[11] with appropriate corrections. The Wigner density is also required in methods that employ quantum-classical Liouville dynamics.[12,13] Many mixed quantum-classical methods, like the quantum-classical path integral (QCPI) methodology,[14–17] require the knowledge of the phase space distribution of the environment degrees of freedom unless zero-point energy can be neglected.

The first step in all the methods mentioned above is the evaluation of the required phase space transform of the density operator, and considerable effort has been devoted to the development of techniques for this task. Several approaches are available for evaluating coherent state representations of the density, including local harmonic approximations,[18] semiclassical propagation in imaginary time,[19] and numerically exact path integral representations.[20,21] Evaluation of the Wigner function presents a more challenging task. Various approximate schemes have been proposed, including local[22] variationally optimized[7] Gaussian approximations, imaginary time semiclassical evolution,[23]

and the thermal Gaussian approximation[24,25] (which consists of frozen Gaussian dynamics[26] in imaginary time) along with extensions that capture quantum corrections.[27] These techniques have been successfully applied to condensed phase systems.[28–31]

The Wigner transform[5] of a density operator $\hat{\rho}$ is given by the Fourier-type integral $\mathrm{W}(x_0, p_0)$

$$\mathrm{W}(x_0, p_0) = \frac{1}{\sqrt{2\pi\hbar}} \int_{-\infty}^{\infty} \left\langle x_0 + \tfrac{1}{2}\Delta x \middle| \hat{\rho} \middle| x_0 - \tfrac{1}{2}\Delta x \right\rangle e^{-\frac{ip_0 \cdot \Delta x}{\hbar}} \, \mathrm{d}\Delta x \tag{2.1.1}$$

(We use one-dimensional notation for convenience; the generalization of Equation 2.1.1 to many dimensions is straightforward.) The oscillatory nature of the Fourier transform makes numerical evaluation of the Wigner function an extremely challenging task. In particular, the "sign problem" that arises from the oscillatory Fourier factor prohibits the use of Monte Carlo methods,[32] leaving no practical alternatives for exact evaluation of the integral in systems of many degrees of freedom.

In this chapter, we develop a very simple, approximate method for obtaining the Wigner transform of a density operator, which is applicable to a pure state as well as the Boltzmann density. The basic idea is to use the exact Wigner density for a zeroth order Hamiltonian to populate the phase space of the system and to evolve these phase space points by classical trajectories, gradually switching on the perturbation potential. According to the classical adiabatic theorem, a trajectory that lies on a phase space torus that corresponds to a particular eigenstate will maintain a constant action, remaining on the eigenstate of the evolving Hamiltonian as long as the adiabatic switching procedure[33,34] is carried out very slowly. By adjusting the weight of each trajectory to account for the change in the Boltzmann population resulting from the energy change of the trajectory, we are able to adiabatically evolve the zeroth order phase space density to the one that closely approximates the Wigner function of a more complex Hamiltonian. Since most uses of the Wigner function are in connection with classical trajectories, the adiabatic switching step is very easily incorporated in such calculations and requires little additional effort. Perhaps, the most appealing feature of our method is the simplicity of the algorithm, which (unlike other methods, such as the thermal Gaussian approximation[24,25,27]) is based exclusively on classical trajectory input. Yet, we find the results to be very accurate, and the resulting Wigner distribution is in all of our test cases nearly indistinguishable from the one obtained by accurate integration of Equation 2.1.1. An additional benefit of our method is that by its very construction, the generated Wigner distribution is invariant under classical trajectory propagation, leading to rigorous preservation of thermodynamic averages.

In Section 2.2, we motivate the idea, starting with eigenstates of harmonic and anharmonic Hamiltonians and proceeding to the thermal density matrix. Test calculations on various one-dimensional and dissipative systems are presented in Section 2.3, and some concluding remarks are given in Section 2.4.

2.2 Classical adiabatic theorem and Wigner density for pure states

2.2.1 Harmonic oscillator eigenstates

Consider a harmonic oscillator $\hat{\mathrm{H}}^{(0)}$ of frequency ω_0

$$\hat{\mathrm{H}}^{(0)} = \frac{\hat{p}^2}{2m} + \frac{1}{2}m\omega_0^2\hat{x}^2 \tag{2.2.1}$$

along with its ground state wavefunction $\Psi_0^{(0)}$ of energy $\mathrm{E}_0^{(0)} = \frac{1}{2}\hbar\omega_0$. The Wigner function of the density operator $\left|\Psi_0^{(0)}\right\rangle\left\langle\Psi_0^{(0)}\right|$ is given by the expression

$$\mathrm{W}_0^{(0)} = \pi^{-1}\exp\left[-\frac{1}{\hbar}\left(m\omega_0 x_0^2 + \frac{p_0^2}{m\omega_0}\right)\right] \tag{2.2.2}$$

The function can be rewritten as

$$\mathrm{W}_0^{(0)} = \pi^{-1}\exp\left(-\frac{\mathcal{E}\left(x_0, p_0\right)}{\mathrm{E}_0^{(0)}}\right) \tag{2.2.3}$$

where

$$\mathcal{E}\left(x_0, p_0\right) = \frac{1}{2}m\omega_0^2 x_0^2 + \frac{p_0^2}{2m} \tag{2.2.4}$$

is the energy of the classical system at (x_0, p_0). Equation 2.2.3 indicates that the Wigner density drops to $1/e$ of its maximum value at phase space points x_0, p_0 whose energy equals the ground state energy of the system. These points form an ellipse, shown schematically in the Figure 2.1(a), whose intersection with the position axis is the classical turning points of the oscillator. Next, consider a harmonic oscillator $\hat{\mathrm{H}}$ of frequency $\omega = \alpha\omega_0$,

$$\hat{\mathrm{H}} = \frac{\hat{p}^2}{2m} + \frac{1}{2}m\omega^2\hat{x}^2 \tag{2.2.5}$$

for which the ground state energy is $\mathrm{E}_0 = \frac{1}{2}\alpha\hbar\omega_0$. The phase space points that correspond to this energy are shown in Figure 2.1(b). Compared to the ellipse for the oscillator with frequency ω_0, the new ellipse is squeezed by a factor of $\sqrt{\alpha}$ along x and stretched by the same factor along the p axis. However, the phase space area remains the same, equal to the action of the ground state, i.e., $\mathrm{S}_0 = \mathrm{S}_0^{(0)} = \frac{1}{2}\hbar$.

Now, suppose the harmonic oscillator $\hat{\mathrm{H}}^{(0)}$ is used as the zeroth order Hamiltonian, while the target system is the harmonic oscillator Hamiltonian $\hat{\mathrm{H}}$ of frequency $\omega = \alpha\omega_0$. Imagine launching a trajectory from a phase space point (x_0, p_0) on the $1/e$ contour of the Wigner function for $\hat{\mathrm{H}}^{(0)}$, i.e., with energy equal to $\frac{1}{2}\hbar\omega_0$, while gradually increasing the oscillator frequency to $\alpha\omega_0$.

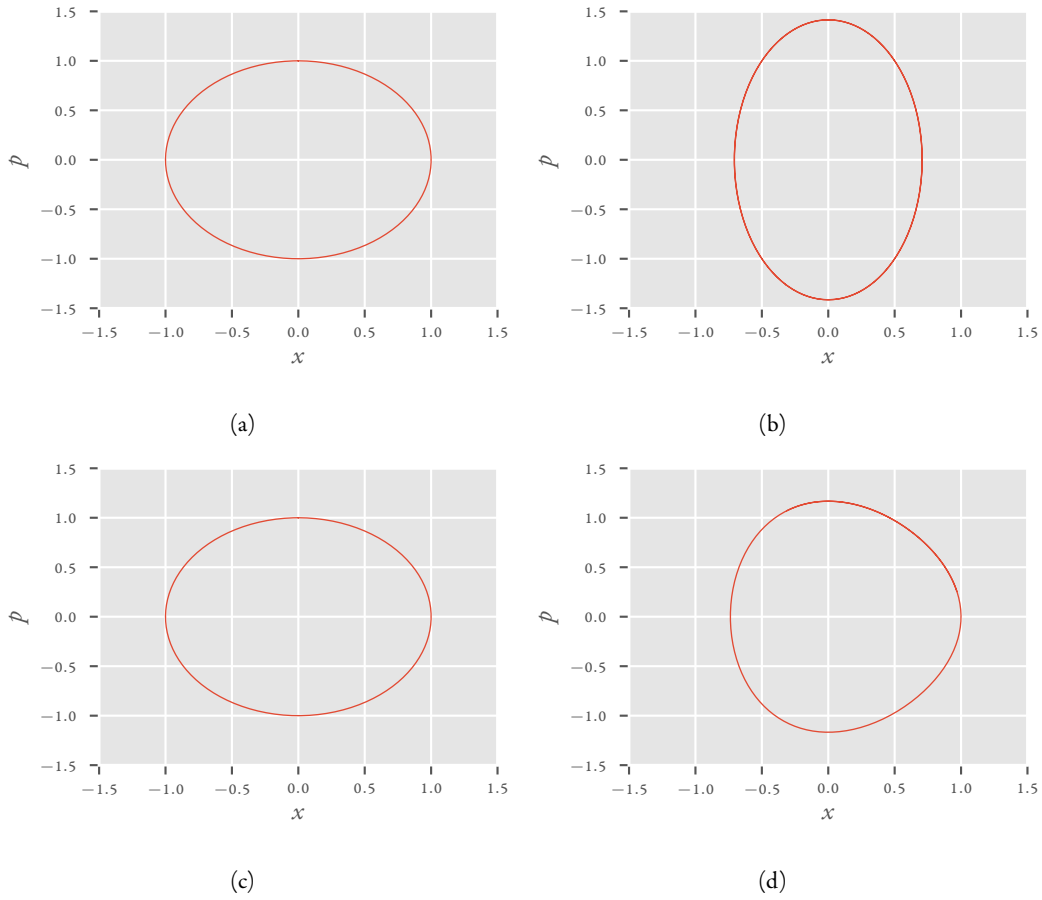

Figure 2.1: Deformation of energy boundary from the zeroth-order to the target Hamiltonian in two cases. (a) and (b) Frequency doubling ($\alpha = 2$) for a harmonic oscillator. (c) and (d) Addition of anharmonic terms to a harmonic oscillator.

If this process is carried out infinitely slowly, the classical adiabatic theorem guarantees that the action of the trajectory will remain unchanged as its energy slowly changes to $\frac{1}{2}\hbar\omega$. Thus, the trajectory that initially traversed the ellipse of Figure 2.1(a) will eventually be found to traverse the ellipse of Figure 2.1(b). The evolution of such a trajectory is shown in Figure 2.2 for a switching time interval equal to 20 oscillation periods. (This switching time, which is not sufficiently long for accuracy, is chosen for clarity of illustration.)

If the above procedure is repeated with many trajectories whose initial conditions trace out the ellipse of Figure 2.1(a), these trajectories will be found to trace out the ellipse of Figure 2.1(b) at the end of the adiabatic switching process. Thus, the $1/e$ contour of the Wigner density for the zeroth order Hamiltonian is transformed to the $1/e$ density contour of the Wigner function that corresponds to the target Hamiltonian $\hat{H}$. The above argument can be extended to phase space points selected to correspond to any density contour of the Wigner function. Thus, one sees

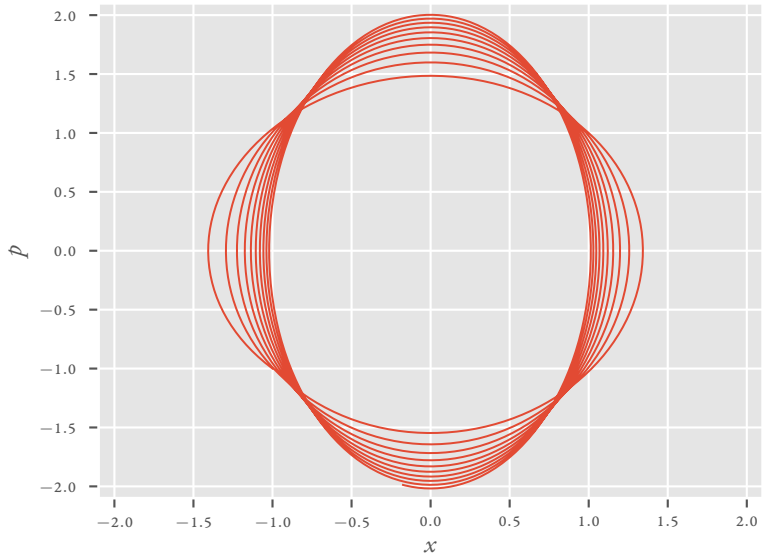

Figure 2.2: Evolution of a trajectory for a harmonic system upon a slow doubling of its frequency.

that the Wigner density of the zeroth order Hamiltonian will be transformed exactly to the correct Wigner density of the target harmonic system if the perturbation potential is switched on infinitely slowly.

The above ideas can be extended to excited states of a harmonic oscillator. The n^{th} eigenfunction of $\hat{\mathrm{H}}^{(0)}$ is given in terms of Hermite polynomials according to the expression

$$\Upsilon_n^{(0)}(x) = \left(\frac{m\omega_0}{\pi\hbar 2^{2n}(n!)^2}\right)^{\frac{1}{4}} e^{-\frac{m\omega_0}{2\hbar}x^2} \mathrm{H}_n\left(\sqrt{\frac{m\omega_0}{\hbar}}x\right) \tag{2.2.6}$$

The corresponding density matrix is

$$\langle x'|\hat{\rho}_n|x''\rangle = \left(\frac{m\omega_0}{\pi\hbar 2^{2n}(n!)^2}\right)^{\frac{1}{2}} e^{-\frac{m\omega_0}{2\hbar}\left(x'^2+x''^2\right)} \mathrm{H}_n\left(\sqrt{\frac{m\omega_0}{\hbar}}x'\right) \mathrm{H}_n\left(\sqrt{\frac{m\omega_0}{\hbar}}x''\right) \tag{2.2.7}$$

and its Wigner transform is

$$\begin{aligned} \mathrm{W}_n^{(0)}(x_0,p_0) = \frac{1}{\sqrt{2\pi\hbar}} \left(\frac{m\omega_0}{\pi\hbar 2^{2n}(n!)^2}\right)^{\frac{1}{2}} e^{-\frac{m\omega_0}{2\hbar}x_0^2} \int e^{-\frac{m\omega_0}{8\hbar}\Delta x_0^2} \mathrm{H}_n\left(\sqrt{\frac{m\omega_0}{\hbar}}\left(x_0+\frac{1}{2}\Delta x_0\right)\right) \\ \times \mathrm{H}_n\left(\sqrt{\frac{m\omega_0}{\hbar}}\left(x_0-\frac{1}{2}\Delta x_0\right)\right) e^{-i\frac{p_0}{\hbar}\Delta x_0}\,\mathrm{d}\Delta x_0 \end{aligned} \tag{2.2.8}$$

Rescaling the coordinates as before, i.e., introducing $x = x_0/\alpha$ (thus $\Delta x = \Delta x_0/\alpha$) and $p = \alpha p_0$,

$$\begin{aligned}
\mathrm{W}_n^{(0)}(x_0, p_0) &= \frac{1}{\sqrt{2\pi\hbar}} \left(\frac{m\alpha\omega_0}{\pi\hbar 2^{2n}(n!)^2} \right)^{\frac{1}{2}} e^{-\frac{m\alpha\omega_0}{2\hbar}\frac{x_0^2}{\alpha}} \int e^{-\frac{m\alpha\omega_0}{8\hbar}\frac{\Delta x_0^2}{\alpha}} \mathrm{H}_n\left(\sqrt{\frac{m\alpha\omega_0}{\hbar}} \left(\frac{x_0}{\sqrt{\alpha}} + \frac{1}{2}\frac{\Delta x_0}{\sqrt{\alpha}} \right) \right) \\
&\times \mathrm{H}_n\left(\sqrt{\frac{m\alpha\omega_0}{\hbar}} \left(\frac{x_0}{\sqrt{\alpha}} - \frac{1}{2}\frac{\Delta x_0}{\sqrt{\alpha}} \right) \right) e^{-i\frac{\sqrt{\alpha}p_0}{\hbar}\frac{\Delta x_0}{\sqrt{\alpha}}} \mathrm{d}\frac{\Delta x_0}{\sqrt{\alpha}} \\
&= \frac{1}{\sqrt{2\pi\hbar}} \left(\frac{m\omega}{\pi\hbar 2^{2n}(n!)^2} \right)^{\frac{1}{2}} e^{-\frac{m\omega}{2\hbar}x^2} \times \int e^{-\frac{m\omega}{8\hbar}\Delta x^2} \mathrm{H}_n\left(\sqrt{\frac{m\omega}{\hbar}} \left(x + \frac{1}{2}\Delta x \right) \right) \\
&\times \mathrm{H}_n\left(\sqrt{\frac{m\omega}{\hbar}} \left(x - \frac{1}{2}\Delta x \right) \right) e^{-i\frac{p}{\hbar}\Delta x} \mathrm{d}\Delta x
\end{aligned} \tag{2.2.9}$$

The last expression is recognized as $\mathrm{W}_n(x,p)$, the Wigner function for the Hamiltonian of frequency $\omega = \alpha\omega_0$.

2.2.2 Semiclassical eigenstates

Next, consider the "primitive" Wentzel-Kramers-Brillouin (WKB) approximation to the wavefunction of a one-dimensional anharmonic Hamiltonian,

$$\psi_{\mathrm{WKB}}(x) = \frac{e^{\frac{i}{\hbar}\int \sqrt{2m(\mathcal{E}-\mathrm{V}(x))}\mathrm{d}x}}{\sqrt{2m\left(\mathcal{E}-\mathrm{V}(x)\right)}} \tag{2.2.10}$$

Evaluating the Wigner integral, Equation 2.1.1, in the limit $\hbar \to 0$ via the stationary phase method, and using $p\left(x+\frac{\Delta x}{2}\right) + p\left(x-\frac{\Delta x}{2}\right) = 2p(x)$, one finds that the Wigner density within the "primitive" WKB approximation has the form

$$\frac{\delta\left(p - \sqrt{2m\left(\mathcal{E}-\mathrm{V}(x)\right)}\right)}{\sqrt{2m\left(\mathcal{E}-\mathrm{V}(x)\right)}} \tag{2.2.11}$$

i.e., the Wigner density is located near the energy shell. For a bound potential, the WKB wavefunction is a linear combination of the "primitive" wavefunctions. In this case, the Wigner density has been shown to be oscillatory near the phase space ridge specified by the energy boundary.[35]

Consider again a point (x_0, p_0) at the energy eigenvalue of the zeroth order Hamiltonian $\hat{\mathrm{H}}^{(0)}$ (for example the harmonic approximation to the potential of $\hat{\mathrm{H}}$). Under the classical force from $\hat{\mathrm{H}}^{(0)}$, the trajectory launched from this point traverses the energy boundary $p(x)^2 = 2m(\mathcal{E} - \mathrm{V}(x))$, tracing out a closed curve of area equal to the action $\mathrm{S}_n^{(0)} = \left(n+\frac{1}{2}\right)\hbar$ that specifies the eigenstate. Upon switching on the perturbation $\hat{\mathrm{H}} - \hat{\mathrm{H}}^{(0)}$ adiabatically, the trajectory deforms to the energy shell of the full Hamiltonian, preserving the value of the action. By virtue of the semiclassical Wigner transform, Equation 2.2.11, it follows that the end point of this trajectory will again specify a point on the Wigner density ridge.

Based on the above ideas, we suggest that the adiabatic switching process from the Wigner density of a reasonable zeroth order Hamiltonian should yield a good approximation to the Wigner distribution of the corresponding

eigenstate of an anharmonic target system. We point out that the adiabatic switching procedure cannot account for subtle quantum mechanical features of the distribution, such as the small shift of the maximum away from the location of the potential minimum which is often observed in the ground state of asymmetric anharmonic systems.

2.2.3 Finite temperature

Last, consider the case of finite temperature. Again, we start with a simple zeroth order Hamiltonian $\hat{\mathrm{H}}^{(0)}$, for which the Boltzmann density is

$$\hat{\rho}^{(0)} = \left(\mathrm{Z}^{(0)}\right)^{-1} e^{-\beta\hat{\mathrm{H}}^{(0)}}, \tag{2.2.12}$$

and consider its spectral expansion in terms of its energy eigenstates,

$$\hat{\rho}^{(0)} = \left(\mathrm{Z}^{(0)}\right)^{-1} \sum_n e^{-\beta \mathrm{E}_n^{(0)}} \left|\Psi_n^{(0)}\right\rangle\!\left\langle\Psi_n^{(0)}\right|. \tag{2.2.13}$$

To motivate the procedure, we express the Wigner transform of this density in terms of the Wigner transforms of the individual eigenstates,

$$\mathrm{W}^{(0)}(x_0, p_0) = \left(\mathrm{Z}^{(0)}\right)^{-1} \sum_n e^{-\beta \mathrm{E}_n^{(0)}} \mathrm{W}_n^{(0)}(x_0, p_0). \tag{2.2.14}$$

Imagine carrying out the adiabatic switching procedure separately for each eigenstate. Upon switching on the perturbation $\hat{\mathrm{H}} - \hat{\mathrm{H}}^{(0)}$ adiabatically, the phase space points x_0, p_0 distributed according to $\mathrm{W}_n^{(0)}$ will evolve to points x, p with distribution that corresponds (approximately) to W_n. Thus, the adiabatic switching procedure described so far will evolve Equation 2.2.14 to the distribution

$$\left(\mathrm{Z}^{(0)}\right)^{-1} \sum_n e^{-\beta \mathrm{E}_n^{(0)}} \mathrm{W}_n(x, p). \tag{2.2.15}$$

However, the Wigner transform of the target density,

$$\hat{\rho} = \mathrm{Z}^{-1} e^{-\beta\hat{\mathrm{H}}} \tag{2.2.16}$$

is given by the expression

$$\mathrm{W}(x, p) = \mathrm{Z}^{-1} \sum_n e^{-\beta \mathrm{E}_n} \mathrm{W}_n(x, p). \tag{2.2.17}$$

One observes that the Wigner densities W_n resulting from the adiabatic switching procedure need to be weighed by the Boltzmann factors corresponding to energies of the full Hamiltonian, yet, according to Equation 2.2.15, the

adiabatic switching trajectories carry the weights that correspond to the energies of the zeroth order Hamiltonian. To correct this, we need to readjust the density at the point (x, p) reached by each trajectory.

The easiest procedure for achieving this task is to include the following classical Boltzmann rescaling factor:

$$f_{\mathrm{CBR}}\left(\mathcal{E}(x,p), \mathcal{E}^{(0)}(x_0,p_0)\right) = e^{-\beta\left(\mathcal{E}(x,p)-\mathcal{E}^{(0)}(x_0,p_0)\right)}. \tag{2.2.18}$$

If many quantum states are occupied at a given temperature, the density argument given in Equation 2.2.18 leads to state occupations consistent with the Boltzmann distribution of the target Hamiltonian. One notices that Equation 2.2.18 does not account for the ratio of the partition functions $\frac{\mathrm{Z}^{(0)}}{\mathrm{Z}}$, because the partition functions are not readily available. However, this ratio is a constant and is conveniently accounted for by normalization. The adiabatic switching method with this classical rescaling factor is denoted by ASW/CBR.

However, the classical weight rescaling procedure as specified in Equation 2.2.18 has no information about the zero-point energy. Hence, it would fail as the temperature approaches zero. In this case, the density operator approaches the ground eigenstate, which is adiabatically transformed correctly without adjustment of trajectory weights. Clearly, the reason for the failure of the classical Boltzmann weight prescription is energy quantization. In the absence of information about the level spacings of the target system, one can approximately remedy this situation by introducing a rescaling factor that depends on the system's ZPE, which is often available for the zeroth order as well as the target Hamiltonian. The expression for the Wigner density of a harmonic oscillator,

$$\begin{aligned}
\mathrm{W}_{harm}(x,p) &= (\hbar\pi)^{-1} \tanh\left(\frac{\hbar\omega\beta}{2}\right) e^{-\tanh\left(\frac{\hbar\omega\beta}{2}\right)\left(\frac{m\omega x^2}{\hbar}+\frac{p^2}{m\omega\hbar}\right)} \\
&= (\hbar\pi)^{-1} \tanh\left(\frac{\hbar\omega\beta}{2}\right) e^{-\tanh(\beta \mathrm{E}_0)\frac{\mathcal{E}(x,p)}{\mathrm{E}_0}},
\end{aligned} \tag{2.2.19}$$

suggests that the proper rescaling factor has the form

$$\exp\left(-\tanh\left(\beta \mathrm{E}_0\right)\frac{\mathcal{E}(x,p)}{\mathrm{E}_0} + \tanh\left(\beta \mathrm{E}_0^{(0)}\right)\frac{\mathcal{E}^{(0)}(x,p)}{\mathrm{E}_0^{(0)}}\right) \tag{2.2.20}$$

Thus the adiabatic switching procedure with the ZPE-based rescaling factor (ASW/ZPE) produces (apart from a normalization factor) the exact Wigner density at all temperatures in the case of a harmonic potential. In the limit of high temperature, $\beta \mathrm{E}_0 \ll 1$, this expression reverts to the classical rescaling factor, Equation 2.2.18, which is correct for any Hamiltonian. Since, most potentials become nearly harmonic at low temperatures, we expect the ZPE-based rescaling procedure to be accurate at low temperatures and also high temperature for anharmonic systems. Thus, the largest errors are expected at intermediate temperatures for systems where the energy level spacings of the target Hamiltonian deviate significantly from the harmonic structure. Our numerical tests on strongly anharmonic systems indicate that the ZPE-based procedure is quite accurate at all temperatures. Further, these results (presented in Section 2.3) suggest that the simpler classical rescaling procedure yields very satisfactory results under most conditions of practical interest, i.e., systems with many degrees of freedom, where full evaluation of the Wigner

integral, Equation 2.1.1, is impractical. These systems have a high density of states at typical temperatures so that the classically derived scaling factor is sufficiently accurate.

To summarize the procedure, the Wigner density of the target system is obtained from adiabatically transformation of a zeroth order Wigner density with weight adjustment,

$$\mathrm{W}(x,p) = \mathrm{N}\mathrm{W}^{(0)}(x_0,p_0) f(\mathcal{E}(x,p),\mathcal{E}(x_0,p_0))\,, \tag{2.2.21}$$

where the weight rescaling factor is given by the classical or the ZPE form, and N is a normalization constant. Since the Wigner density is usual generated for the purpose of calculating time-dependent averages of the type

$$\langle \mathrm{A} \rangle_t = \frac{\iint \mathrm{d}x_0\, \mathrm{d}p_0\, \mathrm{W}(x_0,p_0)\mathrm{A}(x_t,p_t)}{\iint \mathrm{d}x_0\, \mathrm{d}p_0\, \mathrm{W}(x_0,p_0)}, \tag{2.2.22}$$

the normalization factor is evaluated concurrently with the dynamical average.

Quasiclassical methods are often concerned about the inconsistency of generating the initial density by quantum mechanical procedures (whenever this task is feasible) and carrying out the dynamics via classical trajectories, as the quantized distributions are not invariant under classical propagation.[36,37] By its nature, the adiabatic switching construction of the Wigner distribution guarantees its invariance under classical dynamics. This desirable feature ensures exact preservation of thermodynamic properties.

2.3 Application to model systems

In this section, we present numerical examples that illustrate the procedure described in Section 2.2

2.3.1 One-dimensional anharmonic oscillator

In the first example, we choose the potential

$$\mathrm{V}(x) = x^2 - 0.2x^3 + 0.015x^4. \tag{2.3.1}$$

The zeroth order system is chosen as the harmonic oscillator of frequency $\omega_b = \sqrt{2}$. Figure 2.3 shows the (renormalized) Wigner function produced via the adiabatic switching method, both with classical and with ZPE rescaling, at various temperatures. At each chosen temperature, we present the obtained phase space distribution, along with the position and the momentum distributions,

$$\mathrm{P}_p(x) = \int \mathrm{d}p\, \mathrm{W}(x,p), \quad \mathrm{P}_x(p) = \int \mathrm{d}x\, \mathrm{W}(x,p). \tag{2.3.2}$$

These results are compared to accurate calculations generated via a basis set calculation and to the classical Boltzmann distribution.

In spite of the very large anharmonicity, it is seen that the adiabatic transform reproduces the Wigner function rather faithfully at all temperatures. It is particularly encouraging that both the classical and the ZPE weight rescaling factors produce accurate results even far from their optimal regimes. The only observable flaw is the absence of the shift in the maximum of the phase space distribution towards the right of the potential minimum, which is seen in the low temperature distributions obtained by a basis set calculation. This is so because the highest density contours of the Wigner function correspond to trajectories with energies near the potential minimum.

To quantify the respective accuracy attained by the two weight rescaling factors, we show in Figure 2.4 the variance of the position space distribution as a function of temperature. The simple adiabatic switching with classical rescaling is seen to produce quantitative results at all but the lowest temperatures. The adiabatic switching procedure with ZPE rescaling is quantitatively accurate at all temperatures. The importance of the rescaling factor becomes apparent by presenting the raw adiabatic switching results. It is seen that in the absence of the weight rescaling, the method fails to produce accurate results at all but the lowest temperatures.

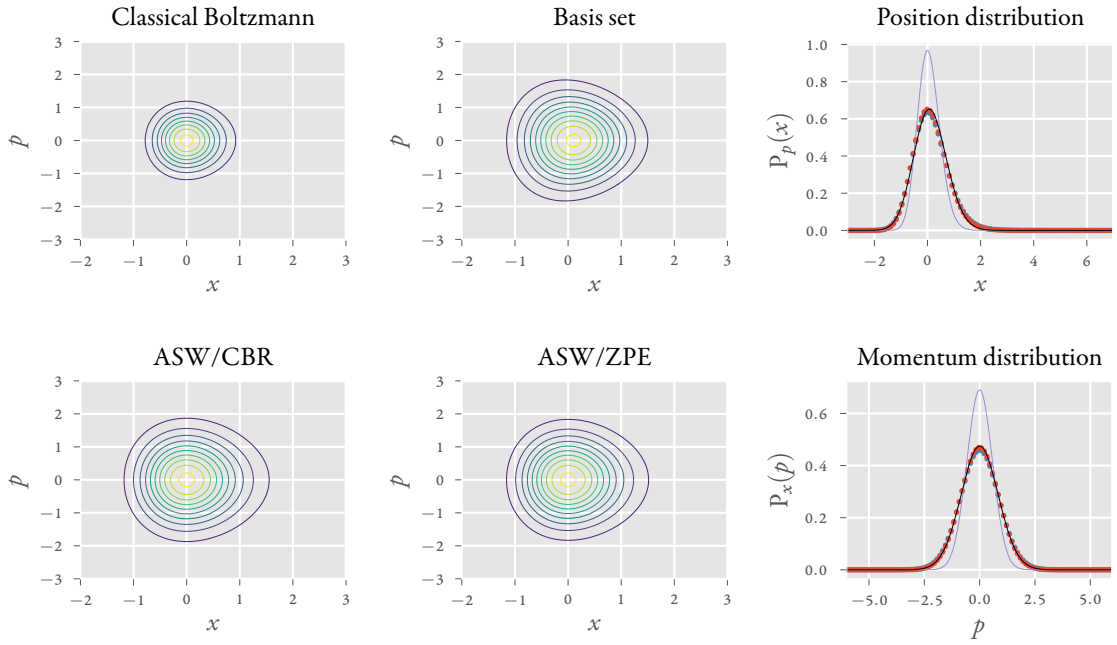

(a) $\hbar\omega\beta = 3\sqrt{2}$

Figure 2.3: 2D histograms of the phase space density, along with the position (top) and momentum (bottom) distribution, obtained by classical Boltzmann (top left, violet line), basis set calculations (top right, black line), ASW with classical rescaling (bottom left, blue markers), ASW with ZPE rescaling (bottom right, red markers).

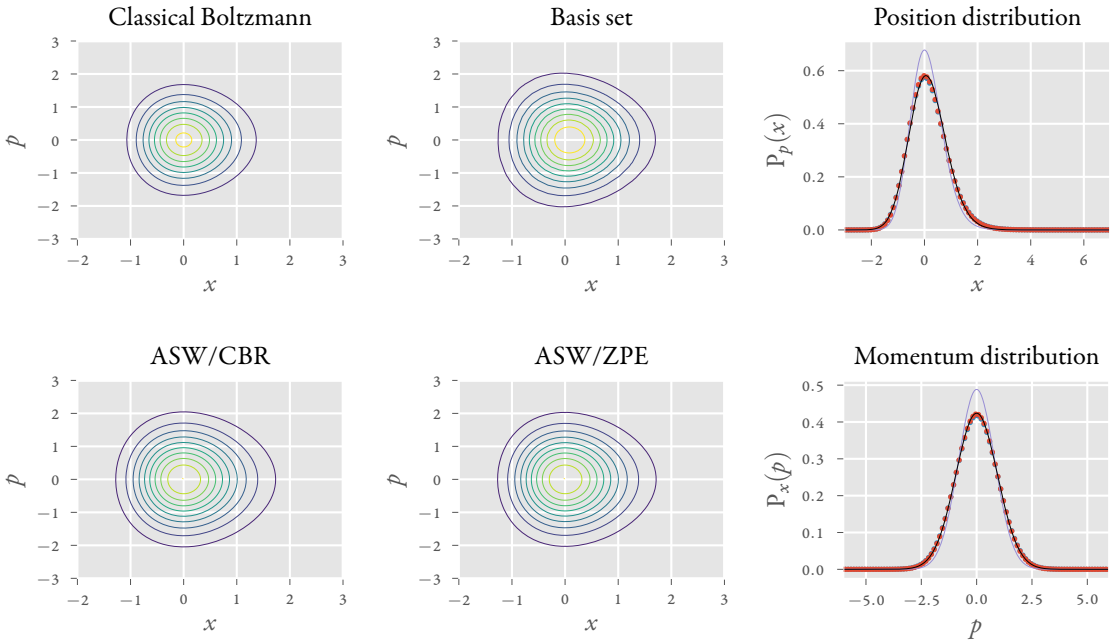

(b) $\hbar\omega\beta = 1.5\sqrt{2}$

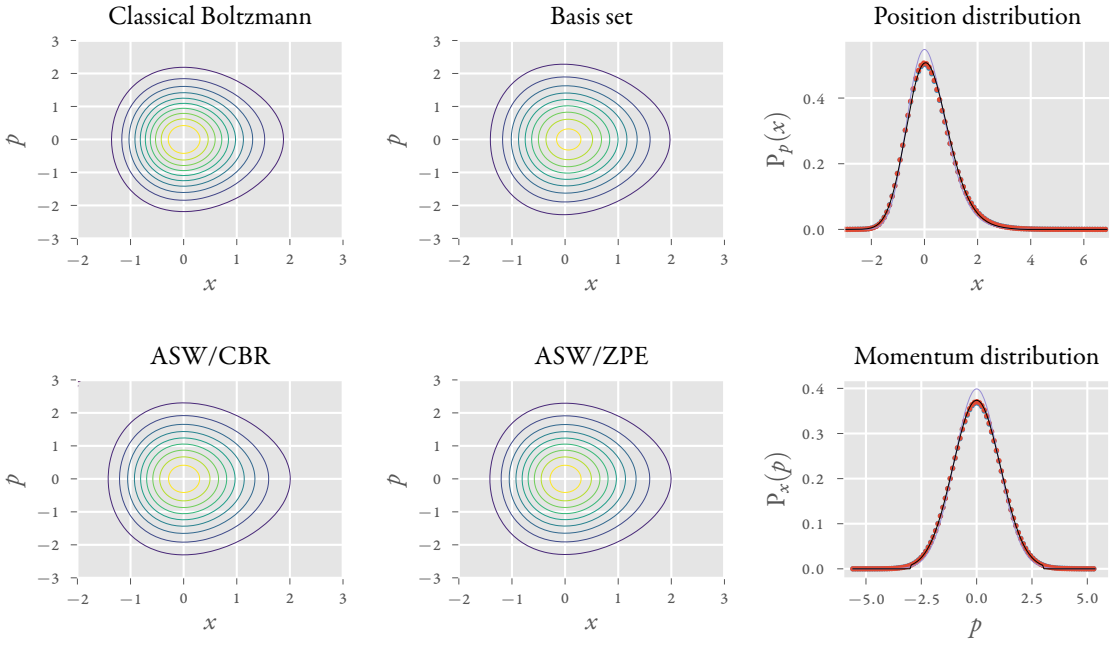

(c) $\hbar\omega\beta = \sqrt{2}$

Figure 2.3: continued

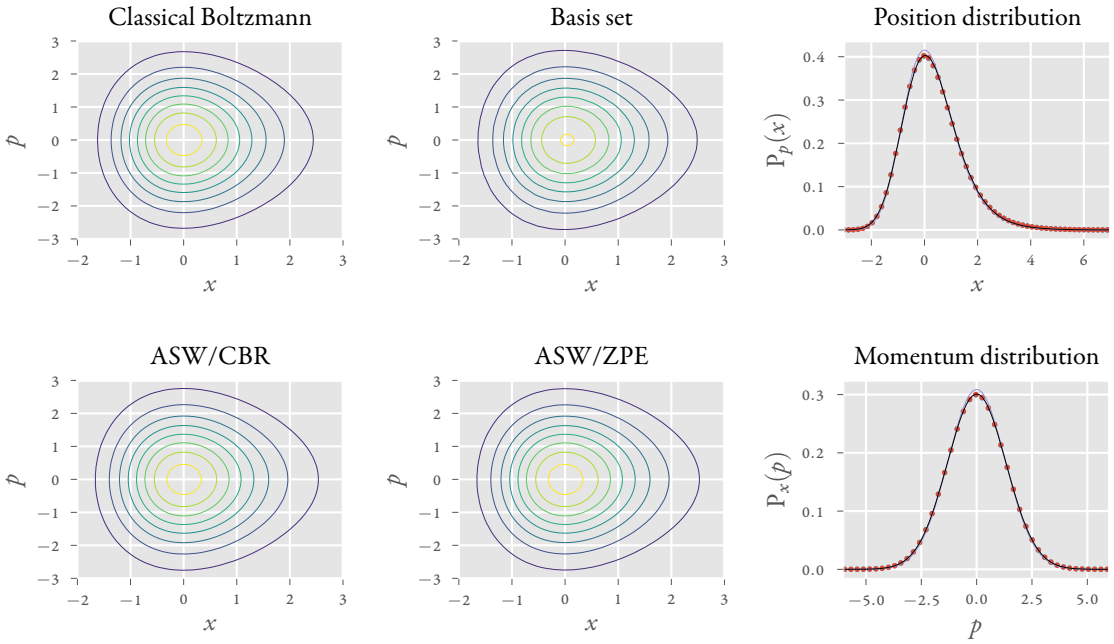

(d) $\hbar\omega\beta = 0.6\sqrt{2}$

Figure 2.3: continued

Lastly, we demonstrate the time invariance of the distribution generated via the adiabatic switching procedure in Figure 2.5, which shows the distribution initially and after classical propagation over 10, 100 and 1000 periods. Since no change of distribution takes place, thermodynamic properties are conserved. This is further illustrated in Figure 2.6, where we plot the Wigner approximation of expectation value of the $\hat{x}^2$ operator as a function of time.

$$\left\langle x^2(t) \right\rangle \approx \iint \mathrm{d}x_0 \, \mathrm{d}p_0 \, \mathrm{W}\left(x_0, p_0\right) x_t^2 \tag{2.3.3}$$

We compare the results obtained from the ASW distribution with those from the exact basis set calculation. While the latter varies with time, the approximate result is invariant. This is because the ASW method acts on entire classical tori, keeping them intact.

2.3.2 Multidimensional system-bath

Finally, we use the adiabatic switching procedure to generate the Wigner function and dynamics for a harmonic system coupled to a dissipative bath. The Hamiltonian has the form

$$\hat{\mathrm{H}} = \hat{\mathrm{H}}^{(0)} - \sum_j c_j \hat{s} \hat{x}_j \tag{2.3.4}$$

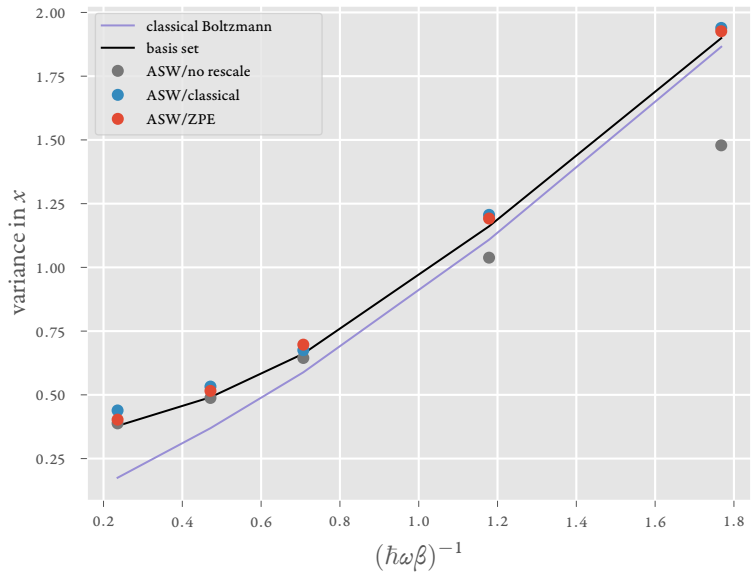

Figure 2.4: Position variance for one-dimensional anharmonic system. Solid black line: basis set calculation. Solid green line: classical Boltzmann results. Blue circles: ASW with classical rescaling. Red circles: ASW with ZPE rescaling. Gray circles: adiabatic switching method without rescaling

$$\hat{H}^{(0)} = \frac{\hat{p}_s^2}{2m} + \frac{1}{2}m\Omega^2\hat{s}^2 + \sum_j \frac{\hat{p}_j^2}{2m} + \frac{1}{2}m\omega_j^2\hat{x}_j^2 \tag{2.3.5}$$

where $m = 1, \Omega = 2$. The frequencies and the system-bath coupling coefficients are collectively specified by the spectral density.[38] We use the Ohmic form with an exponential cutoff,

$$J(\omega) = \frac{\pi}{2}\hbar\xi\omega \exp\left(-\frac{\omega}{\omega_c}\right) \tag{2.3.6}$$

with a cutoff frequency $\omega_c = 1.25\Omega$. The bath was discretized using 60 oscillators with frequency chosen according to the logarithmic discretization of the spectral density[39] with $\omega_{max} = 4\omega_c$. The calculation was performed at four parameter sets, for which the system dynamics changes from weakly damped to near-monotonic decay.

Monte Carlo sampling[32] was used to generate phase space points distributed according to the analytic expression for the 122-dimensional Wigner density. The system-bath coupling was switched on adiabatically over a time period of around 32 oscillations. Trajectory weight rescaling was performed using the classical Boltzmann-weighted procedure.

Once the Wigner distribution was constructed, dynamical results were obtained by continuing the trajectories under forces specified by the system-bath Hamiltonian. We report the real part of the position correlation function

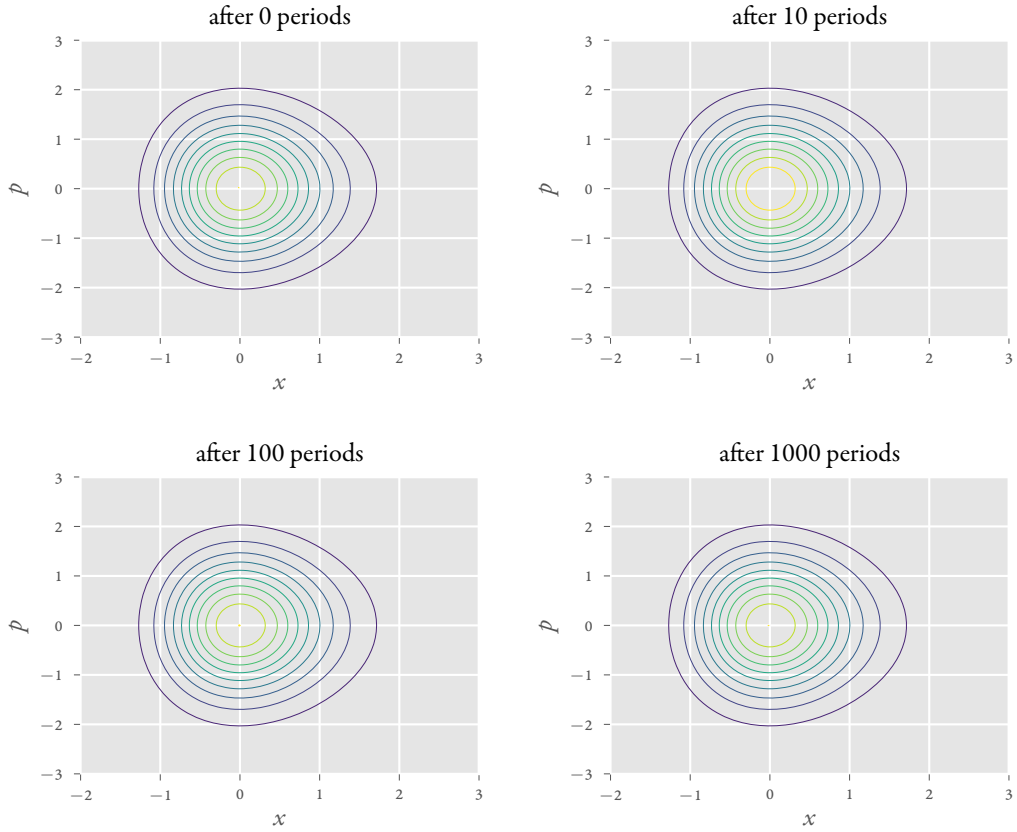

Figure 2.5: Time propagation of ASW distribution.

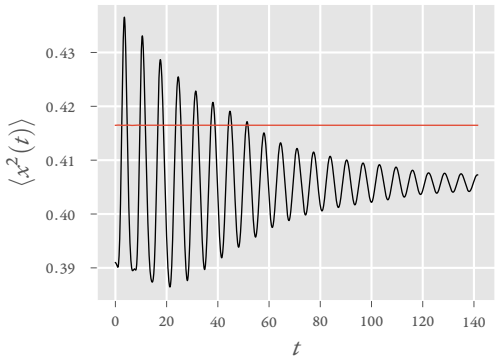

Figure 2.6: Time dependence of thermodynamic expectation value. Black line: Numeric Wigner. Red line: ASW

of the system.

$$\mathrm{C}(t) = \langle s(0)s(t)\rangle \tag{2.3.7}$$

obtained from the Wigner function according to the classical procedure

$$\mathrm{Re}\,\mathrm{C}(t) \approx \iint \mathrm{d}s_0\,\mathrm{d}p_{s,0} \prod_j \iint \mathrm{d}x_{j,0}\,\mathrm{d}p_{j,0}\,\mathrm{W}\left(s_0, p_{s,0}, \{x_{j,0}, p_{j,0}\}\right) s_0 s(t) \tag{2.3.8}$$

Exact results were obtained analytically.

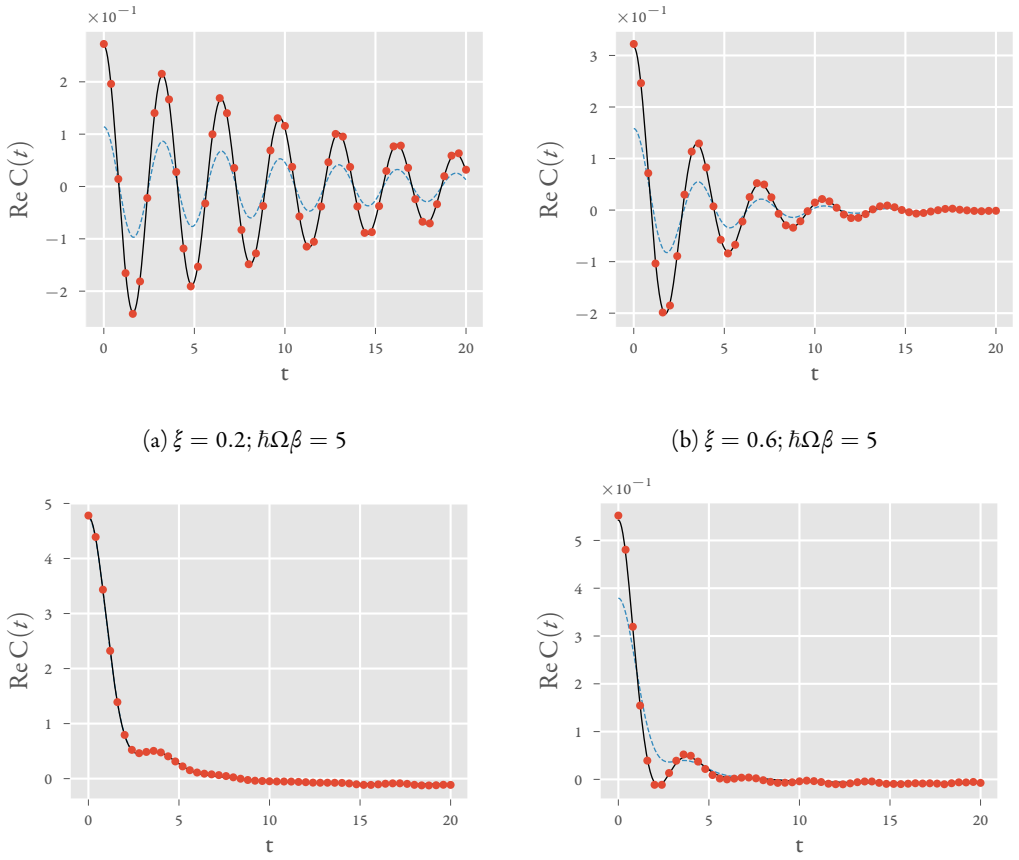

(a) $\xi = 0.2; \hbar\Omega\beta = 5$

(b) $\xi = 0.6; \hbar\Omega\beta = 5$

(c) $\xi = 1.2; \hbar\Omega\beta = 0.4$

(d) $\xi = 1.2; \hbar\Omega\beta = 5$

Figure 2.7: Position correlation function of a harmonic oscillator coupled to a harmonic bath. Black solid line: exact quantum mechanical results. Dashed blue line: classical trajectory results with initial conditions sampled from the Boltzmann density. Red markers: classical results with initial conditions sampled from the Wigner density generated by the adiabatic switching procedure with classical Boltzmann rescaling.

Figure 2.7 shows the adiabatic switching Wigner results, along with the exact quantum mechanical results for this Hamiltonian. Also shown are the results obtained by approximating the Wigner function by the classical Boltzmann phase space density. It is seen that the Boltzmann density severely underestimates the magnitude of the correlation function because of its neglect of ZPE. Even though some of the calculations were performed at a very low temperature with respect to the frequency of the system (and majority of the bath oscillators), the classical Boltzmann-weighted procedure produced excellent results. This is so because a large number of degrees of freedom leads to a high density of states. These findings suggest that the simple adiabatic switching procedure is sufficiently accurate for polyatomic systems.

2.4 Discussion and concluding remarks

The idea of adiabatic switching, which follows from the adiabatic theorem of classical mechanics, is very old.[33] More recently, adiabatic switching was formulated as a trajectory-based procedure for generating semiclassical energy eigenvalues.[34] Even though the idea is strictly valid only when the state of interest is associated with a torus in the full phase space of the system, numerical studies[34] have shown the method to be quite robust even in the presence of chaotic dynamics. However, practical issues are often encountered due to separatrix crossing or when resonant states are present; thus, special care must be taken to choose the initial Hamiltonian in a way that avoids such crossings whenever possible.[40–42] Adiabatic switching has been applied to calculate vibrational energies in molecules with several degrees of freedom.[43–45]

The adiabatic switching procedure described in this chapter is a simple approximate but quite accurate procedure for generating the Wigner transform of the density operator that is valid for pure states or at finite temperature. Because the target density is the Boltzmann operator (or, at zero temperature, the ground state), all degenerate states are to be included, and thus resonant states do not present a problem. Even though it is conceivable that the Wigner density of a strongly anharmonic system may have small negative parts at zero temperature, we have not encountered this situation in any of the strongly anharmonic systems we investigated. At finite temperatures, we expect any small-area negative regions of individual eigenstates to be washed out by the Boltzmann averaging procedure; thus, we do not anticipate the Wigner distribution generated by a positive zeroth order density to lack important structure.

The adiabatic switching based method of generating the Wigner distribution is very easy to implement, as it requires only classical trajectory integration without additional information of potential derivatives. Each trajectory employed in the adiabatic switching procedure can subsequently continue to be propagated in time under the full Hamiltonian to yield dynamic information. The Wigner distribution produced through the adiabatic switching method is invariant under classical propagation, preserving thermodynamic averages. Our numerical tests suggest that the adiabatic switching method is also quite accurate under a variety of conditions. Thus, the method is ideally suited for quasiclassical trajectory calculations and also for calculating the phase space in quantum-classical calculations.

Chapter 3

Adiabatic switching in normal mode coordinates

3.1 Introduction

In Chapter 2, we described a method for obtaining an approximation to the Wigner distribution by using the classical adiabatic switching theorem. The theorem itself states that under an adiabatically changing Hamiltonian, the closed orbits or tori deform in a manner so as to keep the action a constant of motion. Since the classical action is closely linked with quantum numbers in quantum mechanics, it should be expected that through adiabatic switching one can estimate through classical trajectories, information about the quantum states.[34,44,46] This method has been used to calculate semiclassical quantum eigenstates. However, here we are interested in calculating the Wigner transform for the density operator,[5] given by

$$\mathrm{W}(x_0,p_0)=\frac{1}{\sqrt{2\pi\hbar}}\int_{-\infty}^{\infty}\left\langle x_0+\tfrac{1}{2}\Delta x\middle|\hat{\rho}_0\middle|x_0-\tfrac{1}{2}\Delta x\right\rangle e^{-\frac{ip_0\cdot\Delta x}{\hbar}}\,\mathrm{d}\Delta x \tag{3.1.1}$$

In this chapter, we apply the ASW method to calculate the thermal properties of a Hamiltonian based on a normal mode coordinate Hamiltonian for formaldehyde by Romanowski et al.[46] We changed the potential because there were regions of space where the potential reported[46] is unbound. We also explore in depth the time evolution of the ASW distribution, and calculate spectra from the time correlation functions. We also discuss the energy spectrum as obtained from the AS method for semiclassical eigenstates.

3.2 Adiabatically-switched Wigner density in normal mode coordinates

Consider a molecular Hamiltonian expressed in terms of n normal mode coordinates, which has the general form

$$\hat{\mathrm{H}}=\hat{\mathrm{H}}_0+\hat{\mathrm{V}} \tag{3.2.1}$$

where

$$\hat{\mathrm{H}}_0=\sum_{i=1}^{n}\frac{1}{2}\hat{p}_i^2+f_{ii}\hat{q}_i^2,\quad \mathrm{V}(q)=\sum_{i,j,k}^{n}f_{ijk}\hat{q}_i\hat{q}_j\hat{q}_k+\sum_{i,j,k,l}^{n}f_{ijkl}\hat{q}_i\hat{q}_j\hat{q}_k\hat{q}_l. \tag{3.2.2}$$

Here $f_{ii} = \frac{1}{2}\omega_i^2$, where ω_i are the normal mode frequencies, and f_{ijk} and f_{ijkl} are cubic and quartic anharmonicity coefficients, respectively, obtained from the potential function fit. Since the Hamiltonian is expressed in normal modes, the quadratic terms are diagonal. Thus, the normal mode representation gives rise to a convenient zeroth order Hamiltonian whose Wigner density is analytically known. At a temperature $\mathrm{T} = \frac{1}{k_\mathrm{B}\beta}$ (where k_B is the Boltzmann constant), the Wigner function corresponding to H_0 is given by the expression

$$\mathrm{W}_0\left(q,p\right) = \left(\hbar\pi\right)^{-n}\prod_{j=1}^{n}\tanh\left(\frac{1}{2}\hbar\omega_j\beta\right)\exp\left(\tanh\left(\frac{1}{2}\hbar\omega_j\beta\right)\left(\frac{\omega_j q_j^2}{\hbar}+\frac{p_j^2}{\hbar\omega_j}\right)\right) \tag{3.2.3}$$

The ASW density is obtained through the following procedure. Phase space coordinates are sampled from the zeroth Wigner density via a Monte Carlo[32] random walk. Classical trajectories are launched with initial conditions obtained from the sampled phase space points, while the Hamiltonian is slowly changed from H_0 to the full H over a time length τ using a switching function $s(t)$, ie

$$\hat{\mathrm{H}}(t) = \hat{\mathrm{H}}^{(0)} + s(t)\hat{\mathrm{V}} \tag{3.2.4}$$

where $s(0) = 0$ and $s(\tau) = 1$. Various forms of the switching function may be used. The calculations reported in the next section used the form[43]

$$s(t) = \frac{t}{\tau} - \frac{1}{2\pi}\sin\left(2\pi\frac{t}{\tau}\right) \tag{3.2.5}$$

According to the classical adiabatic theorem, a trajectory that lies on a phase space torus evolves in such a manner so as to maintain a constant action, as long as the anharmonic terms are switched on infinitely slowly. However, the energy of the trajectory changes during the adiabatic switching process. To account for the change in the Boltzmann population, we adjust the weight of each trajectory by a rescaling factor, f, ie.

$$\mathrm{W}\left(q,p\right) = \mathrm{N}\mathrm{W}^{(0)}\left(q_0,p_0\right)f\left(\mathcal{E}^{(0)},\mathcal{E}\right) \tag{3.2.6}$$

where N is a normalization factor that does not need to be determined. In particular, we have shown[1] that the ZPE-rescaling factor, Equation 2.2.20 leads to an excellent approximation of the Wigner density. Here $\mathcal{E}^{(0)}\left(q_0,p_0\right)$ is the initial energy of the classical trajectory with phase space coordinates (q_0,p_0) sampled from the Wigner distribution corresponding to the harmonic reference Hamiltonian. $\mathcal{E}\left(q,p\right)$ is the energy reached at the end of the adiabatic switching process, and $\mathrm{E}_0^{(0)}$ and E_0 are the ZPE of the reference and the full Hamiltonians, respectively. At high temperatures, Equation 2.2.20 becomes the ratio of the classical Boltzmann factors at the initial and final energies, ensuring the correct high temperature limit of the Wigner scaling factor for the harmonic oscillator. This leads to the classical Boltzmann rescaling factor, Equation 2.2.18.[1] If the Hamiltonian is sufficiently quadratic near the potential minimum, this procedure results in an ASW distribution which faithfully resembles the Wigner phase space density of the full Hamiltonian.

Calculation of the ZPE, while possible (e.g. via quantum Monte Carlo methods), adds an extra layer of sophistication. We would like to see if we can avoid this extra computation. Typical molecular systems are nearly harmonic at the energy of the ground vibrational state. In such situations, the harmonic ZPE provides a simple and sufficiently accurate approximation to E_0. If the harmonic approximation to the ZPE is not adequate, it may be improved (with minimal computational cost) by adding the diagonal anharmonicity to harmonic reference Hamiltonian. For the calculations presented in this chapter, the use of the harmonic ZPE in the rescaling factor was sufficiently accurate.

A general issue with quasiclassical propagation methods is the inconsistency between the initial quantum density and the classical dynamics that follows. This inconsistency manifests itself in the temporal invariance of the thermal distributions and thermodynamic quantities. Improved dynamical procedures that partially overcome this issue are available, although such schemes are computationally expensive. In this regard, a significant benefit of the ASW is that the obtained phase space density remains (by construction) invariant. We demonstrate this property for the multidimensional system studied here.

3.3 Application to molecular model with six normal modes

In this section, we apply the ASW to a model based on the *ab-initio* quartic potential energy surface developed by Romanowski et al.[46] for the formaldehyde molecule. The normal mode frequencies are 2937 cm^{-1}, 1778 cm^{-1}, 1544 cm^{-1}, 1188 cm^{-1}, 3012 cm^{-1} and 1269 cm^{-1} respectively. Unfortunately, the quartic fit to the potential is unbound and thus ill-behaved at finite temperatures, as it leads to unstable trajectories. We thus modified the potential (primarily the quartic terms) to a confined form, for which the trajectories are stable and bound even at very high temperatures, ensuring that the magnitudes of the coefficients and the coupling terms remain similar. As expected the confining modification led to small upward shifts of the energy levels. Using the adiabatic switching method (which is numerically exact for the ground state energy), we found the the ZPE was increased by 4% and the energy of the first excited state by nearly 5%. The full Hamiltonian has the form given in Equation 3.2.1 and Equation 3.2.2 with $n = 6$ and the force constants are given in Table 3.1.

The anharmonic terms of the Hamiltonian were switched on according to Equation 3.2.5 over a time period of $\tau = 2$ ps. The switching time was chosen to ensure convergence at the highest temperature and kept fixed for all the results reported. We note that much shorter switching times could have been chosen at lower temperatures.

3.3.1 Equilibrium Properties

To assess the accuracy of the ASW density, we first compare various equilibrium properties to accurate results obtained via PIMC calculations and also against those obtained within the harmonic approximation at various temperatures. Figure 3.1 and Figure 3.2 show the marginal distributions

$$\mathrm{P}_i\left(q_i\right) = \int_{-\infty}^{\infty} \mathrm{d}q_1 \ldots \int_{-\infty}^{\infty} \mathrm{d}q_{i-1} \int_{-\infty}^{\infty} \mathrm{d}q_{i+1} \ldots \int_{-\infty}^{\infty} \mathrm{d}q_n \int_{-\infty}^{\infty} \mathrm{d}p_1 \ldots \int_{-\infty}^{\infty} \mathrm{d}p_n \, \mathrm{W}\left(q_1, \ldots, q_n, p_1, \ldots, p_n\right) \quad (3.3.1)$$

Table 3.1: Force constants (in atomic units) for the modified bound model of the formaldehyde normal mode vibrations.

i,j,k,l	force constant	i,j,k,l	force constant	i,j,k,l	force constant
1 1	8.95641×10^{-05}	1 2 2 2	6.06809×10^{-10}	2 3 3 3	5.79834×10^{-11}
2 2	3.28072×10^{-05}	1 2 2 3	3.49433×10^{-09}	2 3 4 4	8.16788×10^{-10}
3 3	2.47445×10^{-05}	1 2 3 3	3.41881×10^{-09}	2 3 5 5	2.49993×10^{-08}
4 4	1.46576×10^{-05}	1 2 4 4	3.99302×10^{-09}	2 3 5 6	8.88722×10^{-09}
5 5	9.41724×10^{-05}	1 2 5 5	1.23419×10^{-08}	2 3 6 6	1.92595×10^{-09}
6 6	1.67271×10^{-05}	1 2 5 6	4.33096×10^{-08}	3 3 3 3	3.01839×10^{-11}
1 1 1	1.58395×10^{-06}	1 2 6 6	1.98986×10^{-09}	3 3 4 4	2.82284×10^{-10}
2 2 2	-3.09488×10^{-07}	1 3 3 3	8.19983×10^{-10}	3 3 5 5	2.08768×10^{-08}
3 3 3	-7.42473×10^{-09}	1 3 4 4	3.47055×10^{-09}	3 3 5 6	2.63248×10^{-09}
1 1 1 1	1.64404×10^{-08}	1 3 5 5	1.24585×10^{-08}	3 3 6 6	1.54438×10^{-09}
1 1 1 2	1.75202×10^{-09}	1 3 5 6	7.06454×10^{-08}	4 4 4 4	7.72218×10^{-10}
1 1 1 3	4.35259×10^{-10}	1 3 6 6	2.71959×10^{-09}	4 4 5 5	2.78328×10^{-08}
1 1 2 2	5.11727×10^{-09}	2 2 2 2	2.09690×10^{-09}	4 4 5 6	3.41463×10^{-10}
1 1 2 3	1.84464×10^{-08}	2 2 2 3	2.29151×10^{-09}	4 4 6 6	1.43632×10^{-09}
1 1 3 3	1.54362×10^{-08}	2 2 3 3	1.57200×10^{-09}	5 5 5 5	2.03858×10^{-08}
1 1 4 4	2.35793×10^{-08}	2 2 4 4	5.30463×10^{-10}	5 5 5 6	4.41000×10^{-09}
1 1 5 5	1.13248×10^{-07}	2 2 5 5	8.45341×10^{-09}	5 5 6 6	2.01654×10^{-08}
1 1 5 6	9.64337×10^{-10}	2 2 5 6	1.88770×10^{-09}	5 6 6 6	7.36786×10^{-10}
1 1 6 6	1.84492×10^{-08}	2 2 6 6	1.00897×10^{-10}	6 6 6 6	6.16225×10^{-10}

of the normal modes as well as the probability distribution of the total potential energy,

$$\mathrm{P}_{pot}(\mathrm{E}) = \int_{-\infty}^{\infty} \mathrm{d}q_1 \ldots \int_{-\infty}^{\infty} \mathrm{d}q_n \int_{-\infty}^{\infty} \mathrm{d}p_1 \ldots \int_{-\infty}^{\infty} \mathrm{d}p_n \, \mathrm{W}(q_1, \ldots, q_n, p_1, \ldots, p_n) \, \delta(\mathrm{E} - \mathrm{V}(q_1, \ldots, q_n)) \quad (3.3.2)$$

at 300K. All the vibrational modes of this molecule are relatively cold at room temperature ($\hbar\omega_i\beta > 5$ for all i). As a result, the normal mode distributions shown in Figure 3.1 are Gaussian-like and in good agreement with those obtained from the harmonic approximation to the Wigner density. Anharmonicity leads to small deviations from the harmonic results. Quantum ZPE effects are very prominent at this temperature. The marginal distributions and potential energy distributions obtained from classical Boltzmann density are much narrower and shifted compared to the PIMC results. As seen in Figure 3.1 and Figure 3.2, the ASW density does an excellent job of capturing these ZPE effects and the small anharmonic corrections.

While neither the original nor the modified potential surface are suitable for high-temperature calculations, the

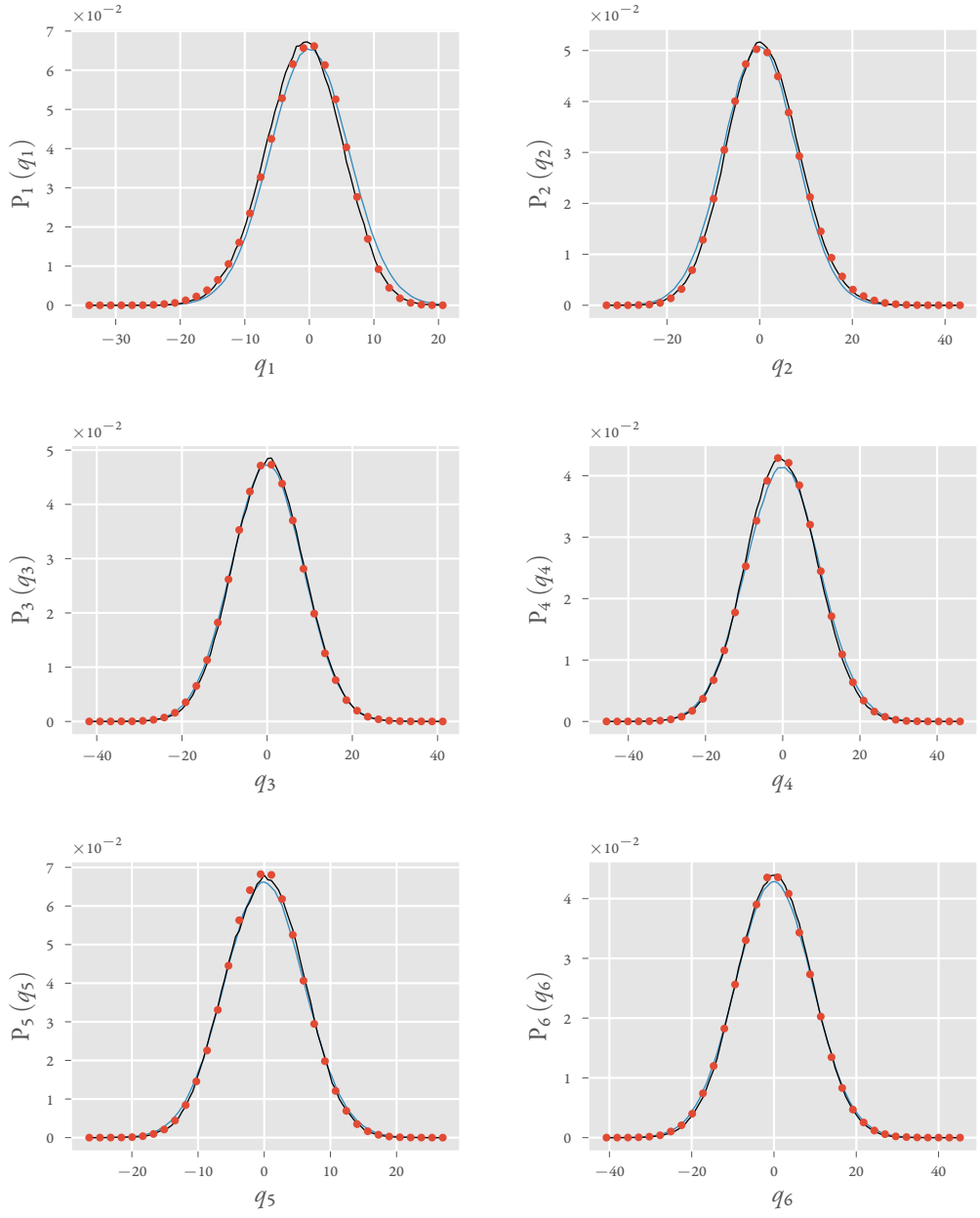

Figure 3.1: Marginal distributions of the six normal modes at 300K. At this temperature $\hbar\omega_{min}\beta = 5.70$ and $\hbar\omega_{max}\beta = 14.4$. Blue lines: harmonic Wigner. Black lines: PIMC results. Red markers: ASW results.

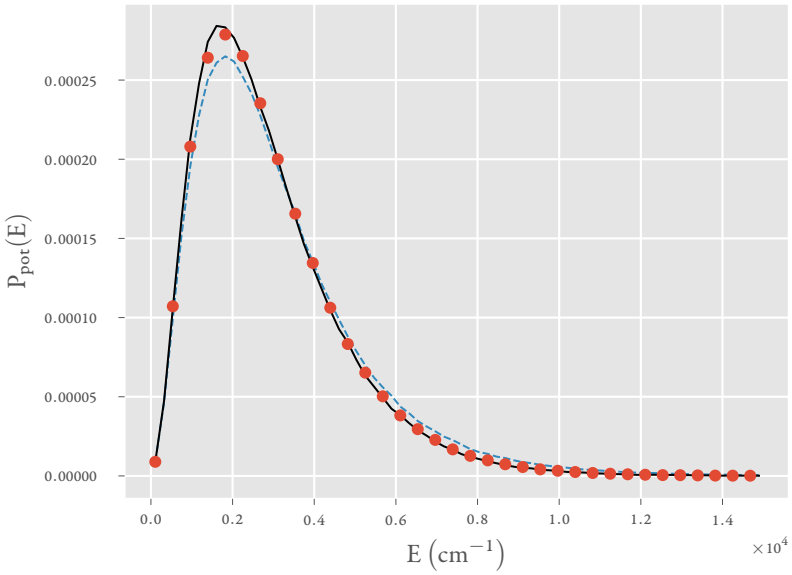

Figure 3.2: Potential energy distribution function at 300K. Blue dashed line: harmonic Wigner. Black line: PIMC results. Red markers: ASW results.

modified potential offers a convenient model for investigating the accuracy of various approximations over a wide range of temperatures. In particular, anharmonicity effects are very prominent at high temperatures, both in the diagonal terms and also in the mode-mode coupling parts of the potential. The results of this comparison have important implications for the performance of these approximate methods on large molecules containing low frequency vibrations, which are highly excited at physiological temperatures and often strongly anharmonic. Figure 3.3 and Figure 3.4 show the normal mode distributions at a temperature for which $\hbar\omega_{min}\beta = 0.11$ and $\hbar\omega_{max}\beta = 0.27$. The accurate distributions obtained from PIMC calculations are strongly skewed at this temperature and resemble closely the classical Boltzmann distributions. Not surprisingly, the harmonic approximation leads to poor results in this case. The ASW procedure again leads to results that are practically indistinguishable from those obtained through the numerically exact PIMC methodology.

In order to quantify the accuracy of the ASW distribution over a broad range of temperatures, we report the Hellinger distance of the ASW marginal distribution of each mode from that given by the PIMC calculations, given by

$$g_i^{\mathrm{ASW}} = \left(1 - \int_{-\infty}^{\infty} \sqrt{\mathrm{P}_i^{\mathrm{ASW}}(q_i)\,\mathrm{P}_i^{\mathrm{PIMC}}(q_i)}\,\mathrm{d}q_i\right)^{\frac{1}{2}} \tag{3.3.3}$$

The Hellinger distance is a measure of the similarity of two probability distributions. The measure is zero for iden-

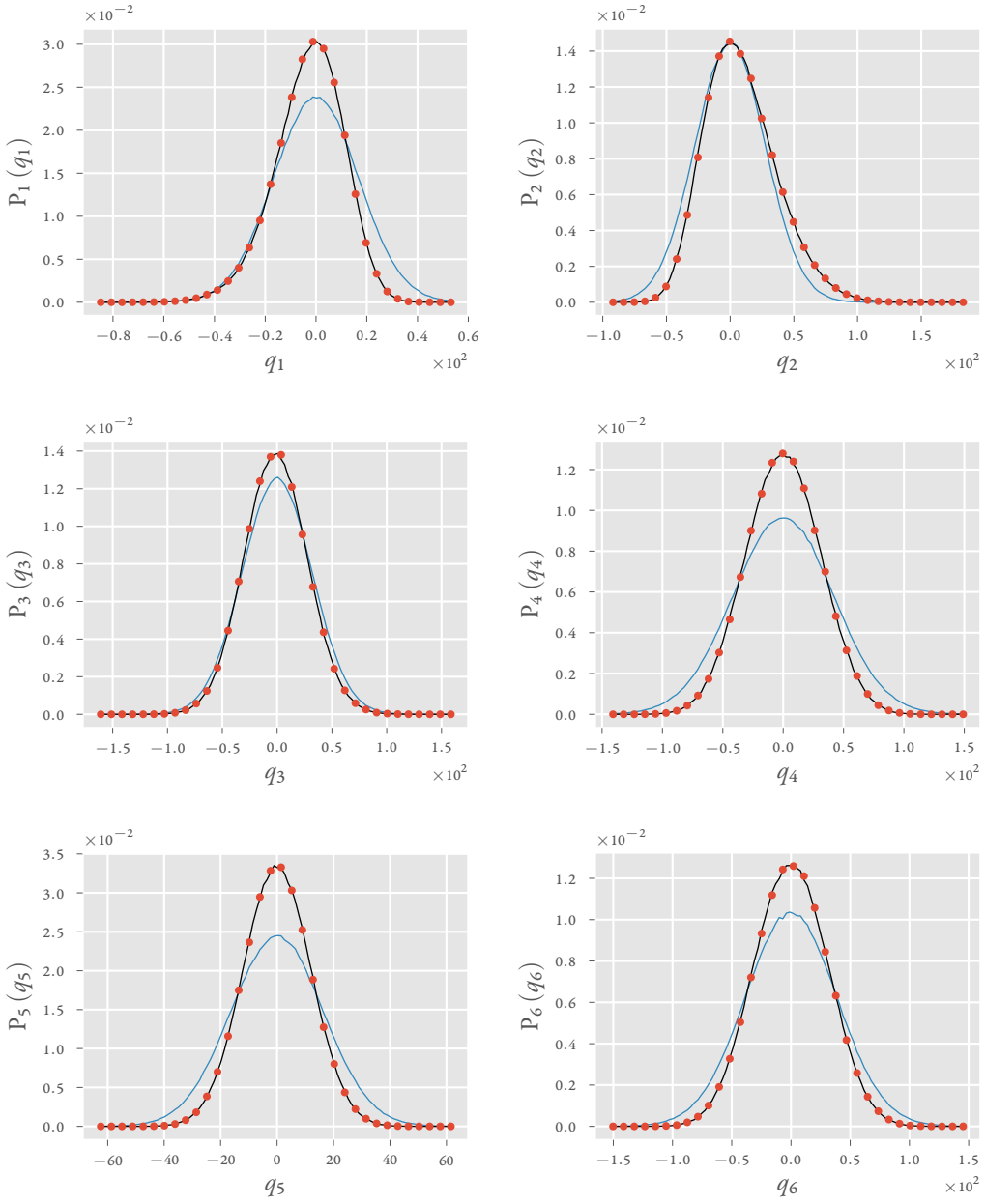

Figure 3.3: Marginal distributions of the six normal modes at a high temperature such that $\hbar\omega_{min}\beta = 0.11$ and $\hbar\omega_{max}\beta = 0.27$. Blue lines: harmonic Wigner. Black lines: PIMC results. Red markers: ASW results.

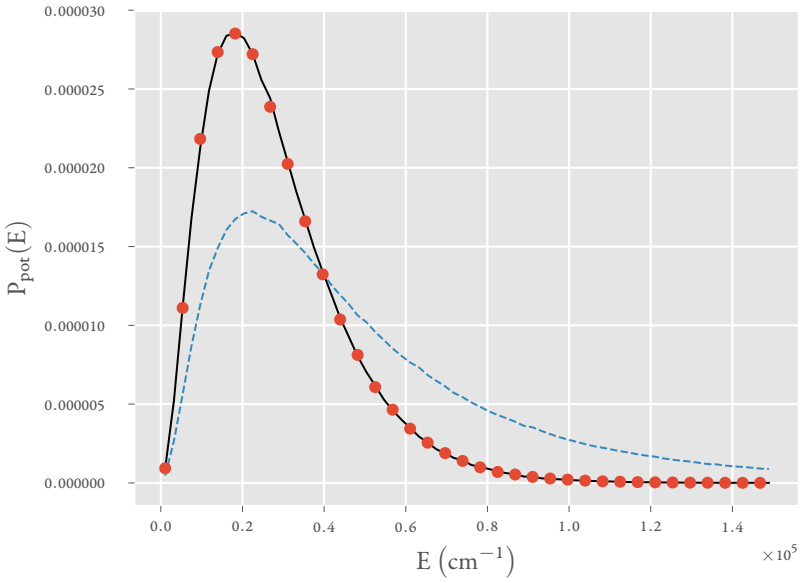

Figure 3.4: Potential energy distribution function at the temperature specified in Figure 3.3. Blue dashed line: harmonic Wigner. Black line: PIMC result. Red markers: ASW results.

tical distributions and unity for pairs of distributions that do not overlap. In Figure 3.5, we compare the Hellinger distance of the ASW distribution from the PIMC result against the Hellinger distance g_i^{har} of the harmonic Wigner density and that of the classical Boltzmann density, g_i^{cl}. Not surprisingly, the error of the harmonic approximation to the Wigner density increases monotonically with temperature, while the classical Boltzmann density fails at the low temperatures. The Hellinger distance of the ASW density remains smaller than 0.03 over the entire temperature range considered, including low temperatures with large ZPE effects and high temperatures where anharmonic potential regions are probed.

Last, we use the Wigner distribution to obtain the expectation values of the squares of the normal mode coordinates,

$$\langle q_i^2 \rangle = \int_{-\infty}^{\infty} \mathrm{d}q_1 \ldots \int_{-\infty}^{\infty} \mathrm{d}q_n \int_{-\infty}^{\infty} \mathrm{d}p_1 \ldots \int_{-\infty}^{\infty} \mathrm{d}p_n \, \mathrm{W}\left(q_1, \ldots, q_n, p_1, \ldots, p_n\right) q_i^2 \tag{3.3.4}$$

Figure 3.6 shows the percentage error of $\langle q_i^2 \rangle$ at various temperatures. It is seen that the harmonic approximation grows steeply with temperature. The error resulting from the ASW distribution remains small at all temperatures, exhibiting a broad maximum at intermediate temperatures, where the method is known to have the worst performance.

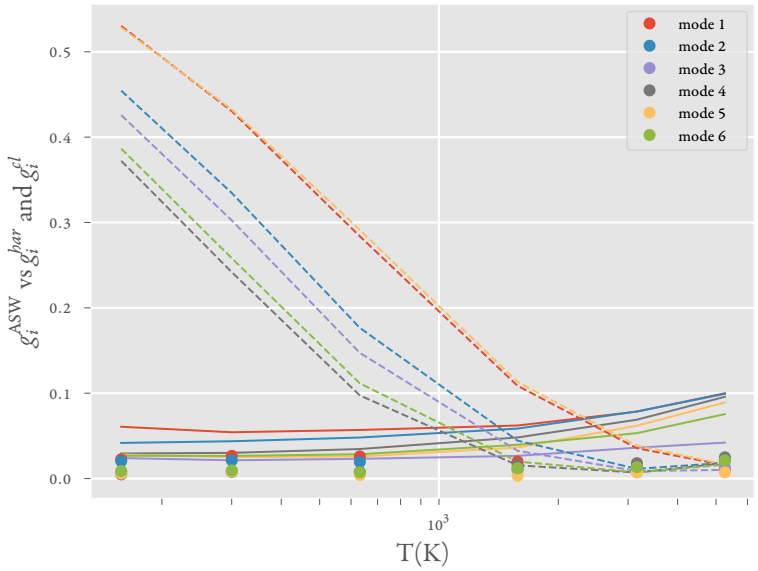

Figure 3.5: Helinger distances of the position distributions of the various modes with PIMC distributions as a function of temperature. Markers: ASW density, solid lines: harmonic approximation to the Wigner density. Dashed lines: classical Boltzmann density.

3.3.2 Dynamical properties

As discussed earlier, the main appeal of the Wigner density is its use for generating initial conditions for quasiclassical or semiclassical trajectory simulations. In the last part of this section, we study the evolution of the ASW density under classical dynamics, as well as the time-dependent observables and the resulting frequency-domain spectra.

First we examine the temporal invariance of thermodynamic quantities. Figure 3.7 shows the average potential energy as a function of time at two temperatures. It is seen that this quantity remains constant, as the ASW density remains invariant under classical propagation. This stability, a consequence of the classical procedure used to generate this phase-space density, is an appealing feature of the ASW scheme from the perspective of quasiclassical dynamics calculations, which prevents spurious oscillations of time-dependent observables. We note again that the exact Wigner function remains invariant only under fully quantum mechanical propagation, exhibiting spiral fluctuations during classical evolution. Figure 3.7 also shows that the average potential energy arising from the harmonic-based Wigner density exhibits significant oscillations during classical trajectory propagation.

Time propagation is often used to generate spectra. Quantum ZPE effects are very important if the forces on the classical trajectories are obtained from *ab initio* electronic structure calculations. Thus the use of a quantized phase space distribution is critical in this task. Below we report the quasiclassical time autocorrelation functions for the six

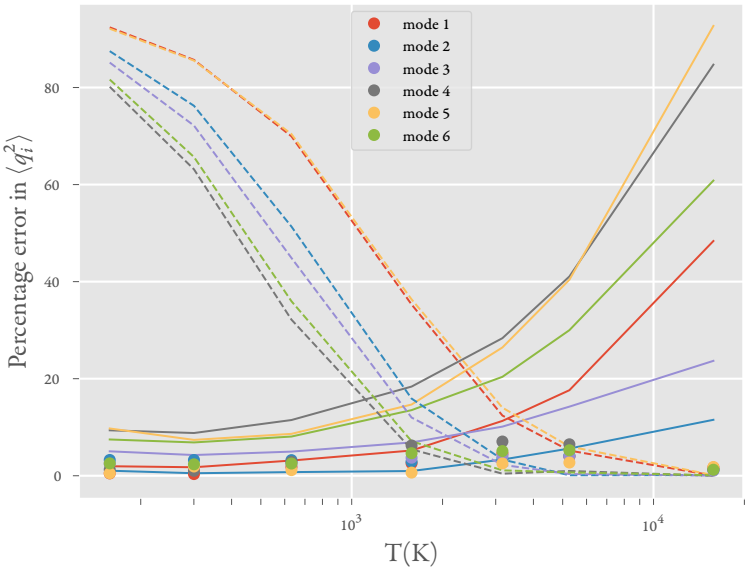

Figure 3.6: Percentage error in $\langle q_i^2 \rangle$ of the various modes with PIMC distributions as a function of temperature. Markers: ASW density, solid lines: harmonic approximation to the Wigner density. Dashed lines: classical Boltzmann density.

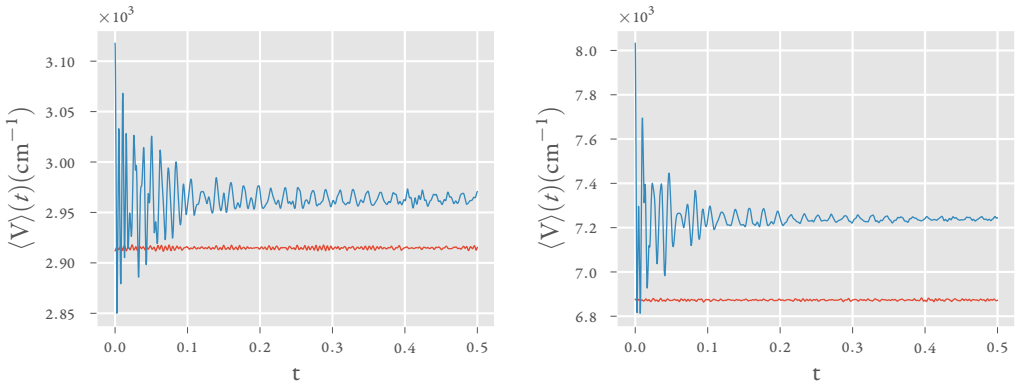

(a) T = 300K (b) T = 3156K

Figure 3.7: Average potential energy as a function of time. Red lines: ASW density. Blue lines: Harmonic Wigner density.

normal modes of the modified formaldehyde potential.

$$\mathrm{G}_k(t) = \int_{-\infty}^{\infty} \cdots \int_{-\infty}^{\infty} \prod_i \mathrm{d}q_i(0)\, \mathrm{d}p_i(0)\ \mathrm{W}\left(q_1(0), \ldots, q_n(0), p_1(0), \ldots, p_n(0)\right) q_k(0) q_k(t) \tag{3.3.5}$$

along with the corresponding mode-specific spectra given by the Fourier transform of these correlation functions,

$$\mathrm{C}_k(\omega) = \frac{1}{\sqrt{2\pi}} \int_{-\infty}^{\infty} \mathrm{G}_k(t) \exp\left(i\omega t\right) \mathrm{d}t\,. \tag{3.3.6}$$

Figure 3.8 shows the mode-specific spectra obtained from the quasiclassical autocorrelation function Equation 3.3.5 at 3156 K. In addition, Figure 3.8 shows the quantum mechanical spectra within the harmonic approximation, and also with the diagonal anharmonicity terms included (obtained from one-dimensional basis set calculations). The one-dimensional anharmonic spectra consist of delta functions (which have been given very small widths for visual clarity) whose peaks exhibit small, primarily blue shifts from the harmonic frequencies, which arise from the quartic potential terms.

A fully quantum mechanical calculation of the correlation function with all six coupled degrees of freedom would be illuminating but is rather challenging. However, we have been able to obtain accurate energy eigenvalues for several low-lying states via the original semiclassical adiabatic switching method.[33,34,40–42] The transition frequencies obtained from these values are shown in Figure 3.9. These transition frequencies exhibit additional blue shifts in comparison with those obtained from the calculations that account only for diagonal anharmonicity, a consequence of confining quartic terms in the mode-mode potential interactions. The spectral peaks obtained from the quasiclassical correlation functions with the ASW phase space density correlate well with the transition frequencies corresponding to the full six-dimensional potential. In addition, the ASW spectra are broadened. This broadening is an intrinsic feature of quasiclassical correlation functions, which eventually decay to zero without being able to account for recurrences associated with quantum interference. In very small systems of one or two degrees of freedom, the absence of recurrences and resulting spectral broadening tend to lead to significant discrepancies from the fully quantum mechanical results. However, the rapidly growing number of transitions in polyatomic molecules leads to very long recurrence times and densely packed spectral lines that are discernible only via high-resolution spectroscopic tools. In such situations quasiclassical calculations tend to produce a low-resolution spectrum that can offer adequate accuracy, provided that ZPE is properly accounted for in the phase space density that specifies trajectory initial conditions. The results presented in this section suggest that the ASW procedure provides an excellent way of achieving this quantization for molecular systems in the normal mode representation.

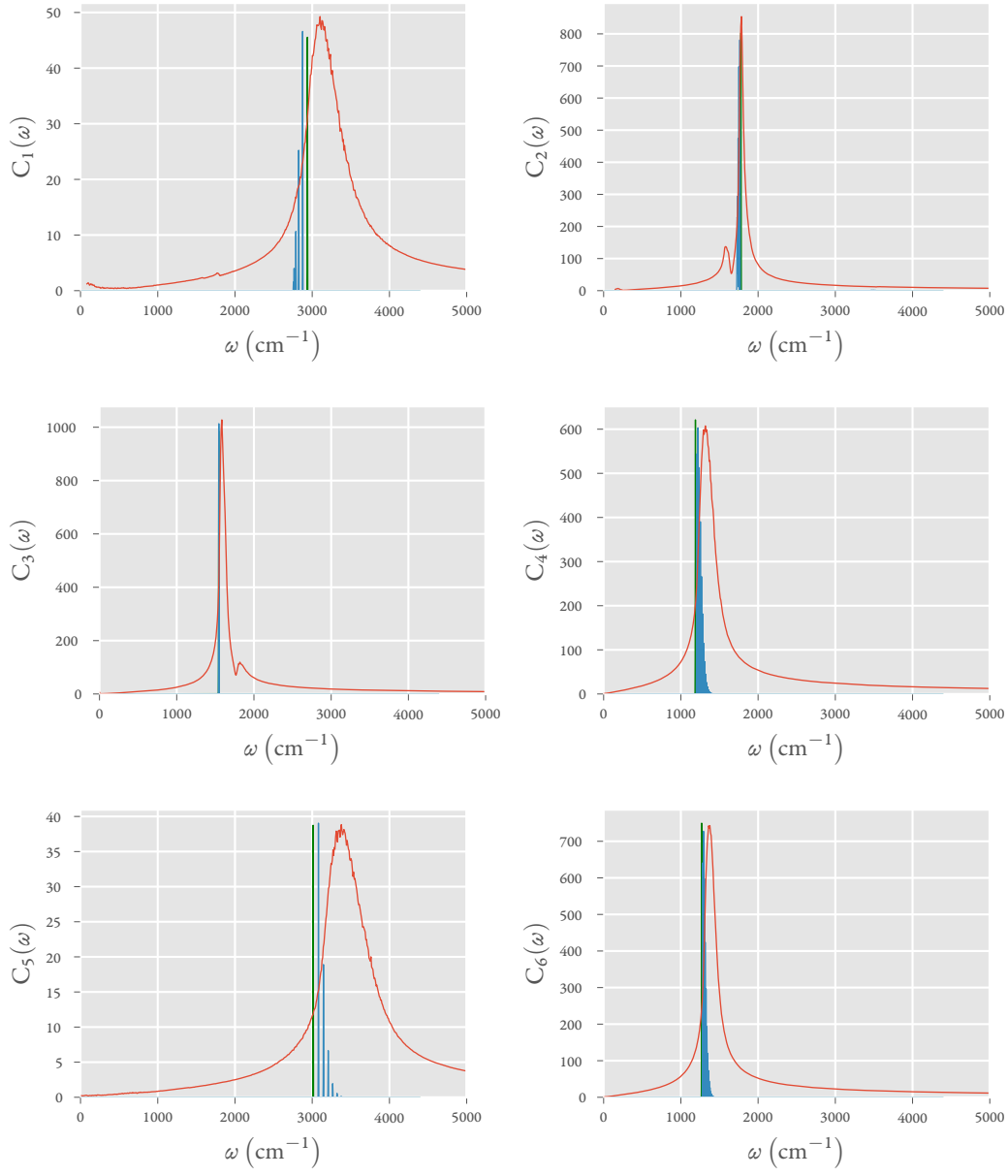

Figure 3.8: Spectra for various modes at 3156 K obtained by Fourier transforming the position autocorrelation function. Red line: spectra from classical trajectories sampled from the ASW distribution and propagated under the full potential. Blue line: quantum mechanical results in absence of anharmonic mode coupling terms. Green line: spectrum arising from the harmonic part of the Hamiltonian

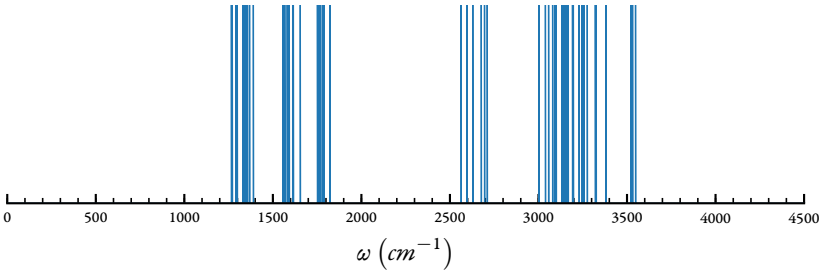

Figure 3.9: Transition frequencies from semiclassical eigenstates obtained via adiabatic switching.

3.4 Discussion and concluding remarks

In this chapter, we have demonstrated how to use the ASW method to generate the Wigner phase space density for a molecule with several degrees of freedom whose Hamiltonian is given in normal mode coordinates. This is the simplest application of the method. Starting from the decoupled normal mode Hamiltonian as the zeroth order Hamiltonian, the trajectories are propagated under adiabatically transforming Hamiltonian to the final fully coupled Hamiltonian. Because the ASW method is based on classical trajectories, it is important for the potential energy surface to be bound over the energy regions sampled by the trajectories. This is not very limiting because the subsequent trajectories used for quasiclassical simulations would of course be subject to the same constraints.

We also applied ASW to the problem at very high temperatures, to test how well it deals with cases where regions of high anharmonicity are sampled. For small molecules of course such temperatures are unrealistic, but for large floppy molecules, such anharmonic regions would be explored pretty regularly at physiological temperatures. We show that ASW is able to reproduce the effects of anharmonicity very effectively, giving quantitative agreement with fully converged PIMC results. We show the invariance of thermodynamic quantities when the dynamics is started from the ASW distribution. This is not the case for the true Wigner density.

In Chapter 4, we show that the main ideas of ASW method carry over completely to the case of Cartesian coordinates. There are a couple of subtleties that need to be taken care of. We deal with those issues and show the applicability of ASW to an atomistic Hamiltonian.

Chapter 4

Adiabatic switching in Cartesian coordinates

4.1 Introduction

In the previous chapter, we used the ASW method to calculate the Wigner function for a Hamiltonian expressed in the normal mode coordinates. While this is a common coordinate system in use, in today's literature an increasing number of potential energy surfaces are given in Cartesian coordinates. This encompasses both highly accurate potential energy surfaces (PES) with sub-wavenumber accuracy, as well as molecular dynamical force fields like CHARMM. Potentials like CHARMM that are fit to experiments rather than *ab initio* calculations have a limitation. They cannot be used outside a very narrow range of parameters, whereas an *ab initio* PES is valid in the entire range of interpolation and can be used at all temperatures if we can calculate the accurate thermal distributions. Calculating the Wigner phase space distribution for a general multidimensional potential is in general difficult. With ASW method, we want to demonstrate it is possible to calculate the Wigner function for the most general case. The essential question becomes how to define a zeroth Hamiltonian. In Section 4.2, we discuss the implementation of ASW in Cartesian coordinates, followed by an application of the method to the CHARMM force field of butyne in Section 4.3.

4.2 ASW in Cartesian coordinates

The Hamiltonian for a CHARMM force field has the form

$$\mathrm{H_{CHARMM}} = \sum_{j}^{\mathrm{N}} \frac{\vec{p}_j \cdot \vec{p}_j}{2m_j} + \sum_{j}^{\mathrm{bond}} \frac{1}{2} k_{b_j} \left(b_j - \bar{b}_j\right)^2 + \sum_{j}^{\mathrm{angle}} \frac{1}{2} k_{\vartheta_j} \left(\vartheta_j - \bar{\vartheta}_j\right)^2 + \text{non-bonded} \tag{4.2.1}$$

where $\vec{p}_j$ is the momentum of the j^{th} atom, b_j is the bond length of the j^{th} bond, with a spring constant of k_{b_j} and mean bond length of $\bar{b}_j$. ϑ_j is the j^{th} angle with a mean of $\bar{\vartheta}_j$ and spring constant of k_{ϑ_j}. Non-bonded interactions include dihedral interactions and van der Waals interactions described by the Lennard-Jones potential.

This does not allow a very obvious choice for a zeroth Hamiltonian. So we consider the Hamiltonian obtained

by the normal mode analysis of Equation 4.2.1 as the zeroth Hamiltonian

$$\mathrm{H}_0 = \sum_{j=0}^{3\mathrm{N}-6} \frac{\mathrm{P}_j^2}{2} + f_{jj}\mathrm{X}_j^2 \tag{4.2.2}$$

where $\left(\mathrm{X}_j, \mathrm{P}_j\right)$ are the normal mode phase space point and N is the number of atoms.

The analytical Wigner function corresponding to H_0 is sampled and trajectories are launched. These trajectories are propagated under a time dependent Hamiltonian which slowly changes from H_0 to $\mathrm{H}_{\mathrm{CHARMM}}$ over a switching time of τ.

$$\mathrm{H}(t) = (1 - s(t))\,\mathrm{H}_0 + s(t)\mathrm{H}_{\mathrm{CHARMM}} \tag{4.2.3}$$

where $s(t)$ is the switching function. The trajectories are defined by Hamilton's equations of motion

$$\begin{aligned}
\dot{\vec{q}} &= (1 - s(t))\,\frac{\partial}{\partial \vec{p}}\mathrm{H}_0\left(\vec{\mathrm{X}}\left(\vec{q},\vec{p}\right), \vec{\mathrm{P}}\left(\vec{q},\vec{p}\right)\right) + s(t)\frac{\partial}{\partial \vec{p}}\mathrm{H}_{\mathrm{CHARMM}}\left(\vec{q},\vec{p}\right) \\
\dot{\vec{p}} &= -\,(1 - s(t))\,\frac{\partial}{\partial \vec{q}}\mathrm{H}_0\left(\vec{\mathrm{X}}\left(\vec{q},\vec{p}\right), \vec{\mathrm{P}}\left(\vec{q},\vec{p}\right)\right) - s(t)\frac{\partial}{\partial \vec{q}}\mathrm{H}_{\mathrm{CHARMM}}\left(\vec{q},\vec{p}\right)
\end{aligned} \tag{4.2.4}$$

where $(\vec{q},\vec{p})$ is the Cartesian phase space point. We explicitly note the dependence of the equation of motion on the two Hamiltonians. Notice that H_0 and $\mathrm{H}_{\mathrm{CHARMM}}$ are not defined on the same spaces. H_0 acts on the reduced dimensional space spanned by the normal mode coordinates, whereas $\mathrm{H}_{\mathrm{CHARMM}}$ is defined in the full 6N dimensional Cartesian phase space. At every time point, there are two contributions to the forces on the atoms — one coming from $\mathrm{H}_{\mathrm{CHARMM}}$ and the other coming from H_0. So, there is a need to convert back and forth between the Cartesian coordinates $(\vec{x},\vec{p})$ and the normal mode coordinates at every time step. This dimension reduction makes the corresponding coordinate transformation unstable. Consider a Hamiltonian which does not couple the rotational and vibrational degrees of freedom. In a Watson Hamiltonian, this would correspond to the absence of coriolis terms. Different rotational structures with the same vibrational configuration should have the same normal mode geometry and energy. This however does not happen if the Hessian matrix is naïvely diagonalized after removal of center of mass motion. The rotational degrees of freedom need to be projected out by going into an Eckart frame of reference. Ideally a Hamiltonian that does not have rotational terms should not lead to changes in the rotational configuration, but in practice even in such cases, numerical instabilities couple the rotational and vibrational degrees of freedom.

The decoupling of the rovibrational degrees of freedom cannot be done completely for a general Hamiltonian. So, the goal is to minimize the coupling between the two. The rotational matrix, C, which transforms from the laboratory frame to the Eckart frame is determined by a method outlined by Czakó and Bowman.[47] It satisfies the following relation

$$\sum_j m_j \vec{r}_j^{\,\mathrm{eq}} \times \left(\mathrm{C}\vec{r}_j - \vec{r}_j^{\,\mathrm{eq}}\right) = 0 \tag{4.2.5}$$

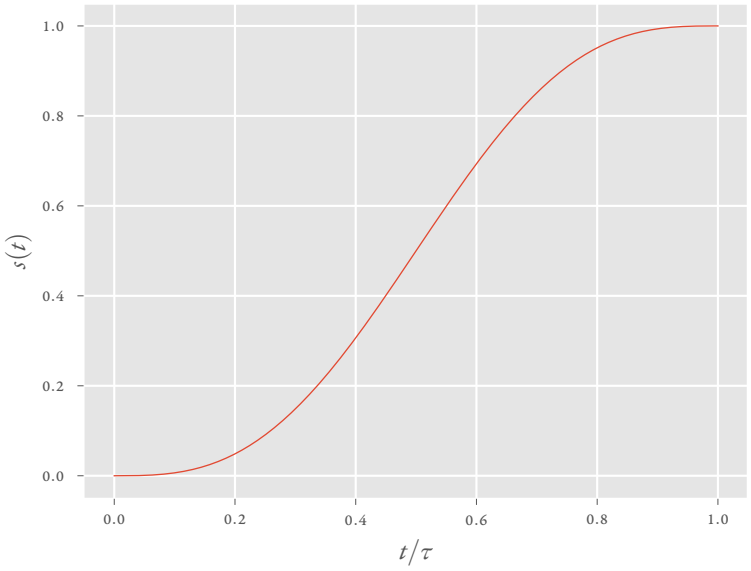

Figure 4.1: Transfer function for ASW

where $\vec{r}_j^{\,\mathrm{eq}}$ is the equilibrium configuration on the basis of which the normal mode analysis would be done. Basically this is a method of bringing the molecule to a configuration that is the closest to the "equilibrium" configuration through just a rotation. Thus, if the molecule has just rotated, all the normal mode coordinates obtained by diagonalizing the Hessian in this Eckart frame, would be 0.

The calculations reported in Section 4.3 use a switching function of the form

$$s(t) = \frac{t}{\tau} - \frac{1}{2\pi}\sin\left(2\pi\frac{t}{\tau}\right) \tag{4.2.6}$$

which is a sigmoidal transfer function which goes from 0 to 1 over the time period of τ. The graph of $s(t)$ with respect to t is shown in Figure 4.1.

We use ZPE-rescaling to reweigh the trajectories. So, finally the ASW procedure can be summarized as

$$\mathrm{W}\left(\vec{q},\vec{p}\right) = \mathrm{NW}^{(0)}\left(\vec{\mathrm{X}}_0\left(\vec{q}_0,\vec{p}_0\right),\vec{\mathrm{P}}_0\left(\vec{q}_0,\vec{p}_0\right)\right) f\left(\mathcal{E}^{(0)},\mathcal{E}\right) \tag{4.2.7}$$

$$f_{\mathrm{ZPE}}\left(\mathcal{E}^{(0)},\mathcal{E}\right) = \exp\left(-\tanh\left(\beta \mathrm{E}_0\right)\frac{\mathcal{E}\left(\vec{q},\vec{p}\right)}{\mathrm{E}_0} + \tanh\left(\beta \mathrm{E}_0^{(0)}\right)\frac{\mathcal{E}^{(0)}\left(\vec{\mathrm{X}},\vec{\mathrm{P}}\right)}{\mathrm{E}_0^{(0)}}\right) \tag{4.2.8}$$

As discussed in Section 3.2, due to the added cost of calculating the ZPE for multidimensional anharmonic systems, we approximate it by the harmonic zero-point energy. Here we sample normal mode phase space points and propagate them under a time dependent Hamiltonian in Cartesian coordinates.

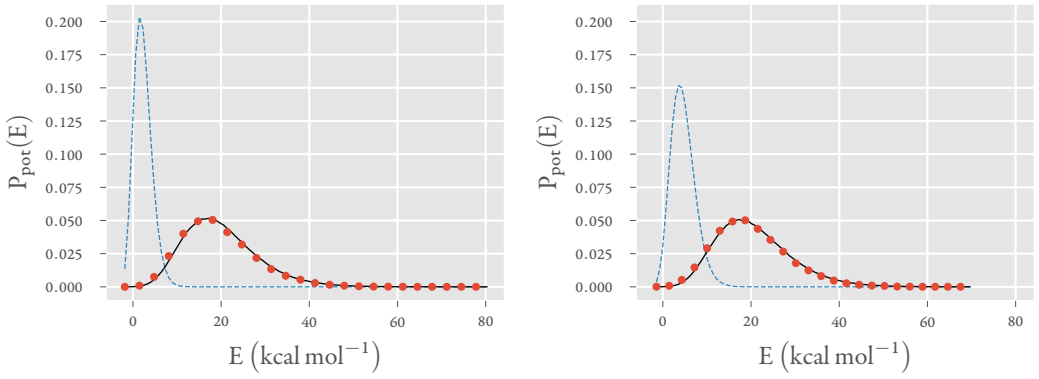

Figure 4.2: Potential energy distribution for butyne at 298 K (left) and 400 K (right). Blue line: Classical Boltzmann. Black line: PIMC. Red markers: ASW

4.3 Application to butyne

Consider the CHARMM force field for but-2-yne. The full Hamiltonian has the form Equation 4.2.1. The non-bonded interactions consist of van der Waals forces given by the Lennard-Jones form and Coulombic electrostatic interactions. All parameters have been obtained from the CHARMM force field. "Scaled 1-4" interaction scheme was used for the simulations. The anharmonicity in the Hamiltonian comes from angular interaction terms, the van der Waals and Coulombic potential terms. The bonded interactions are described by purely harmonic terms. The adiabatic switching done over a period of $\tau = 2$ ps gives converged results for the potential energy distribution. The effect of quantization is already involved in the parameterization of the CHARMM force fields, so, the quantization that we get from ASW would in fact give incorrect results. However here we are using this as a test bed to make sure that we can get results that agree with fully quantum PIMC results even for atomistic Hamiltonians in Cartesian coordinates. We study the thermodynamics at two temperatures 298 K and 400 K.

First consider the potential energy distribution at the two temperatures in Figure 4.2. As expected the ASW results match the fully converged PIMC results quantitatively. We note that the classical Boltzmann result undergoes a large change as the temperature increases from 298 K to 400 K. The average potential energy for the classical distribution shifts from 2.26 kcal mol^{-1} to 4.60 kcal mol^{-1}, and the standard deviation of the distribution also increases from 2.01 kcal mol^{-1} to 2.70 kcal mol^{-1}. This clearly shows the lack of a quantization of energy levels in classical Boltzmann thermodynamics. The energy increases monotonically with temperature. However for both the PIMC and ASW distributions, we notice that the potential energy distributions hardly undergo any change. This only happens when the temperature changes are much less than the difference between the energies of the eigenstates, and the populations on these states do not change significantly. In this case the entire population is mostly stuck in the vibrational ground state. The ZPE pushes the average potential energy up by almost 20 kcal mol^{-1}. The spread is also significantly more than that in pure classical Boltzmann statistics.

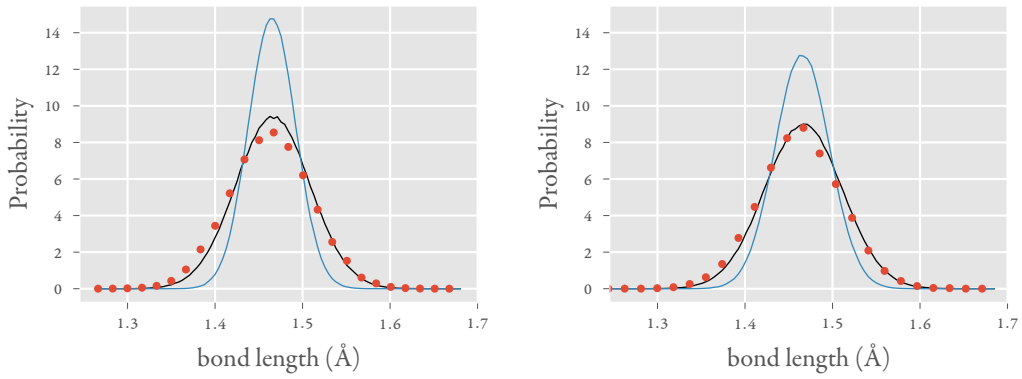

Figure 4.3: C —— C bond length distribution at 298 K (left) and 400 K (right). Blue line: Classical Boltzmann. Black line: PIMC. Red markers: ASW

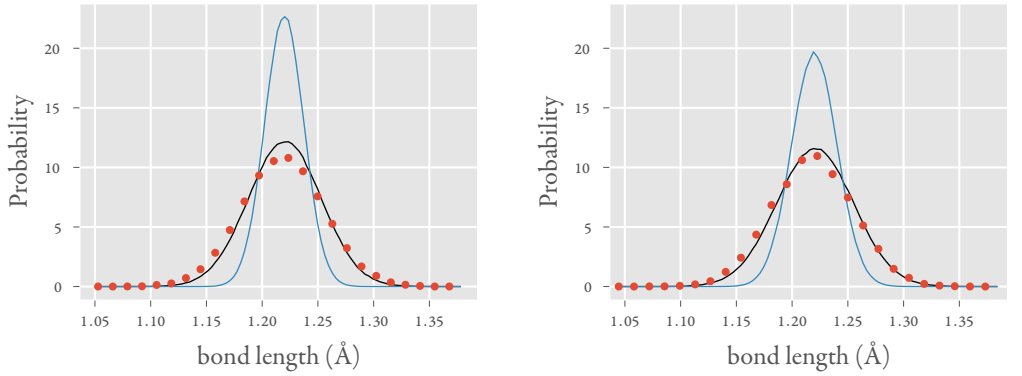

Figure 4.4: C ≡ C bond length distribution at 298 K (left) and 400 K (right). Blue line: Classical Boltzmann. Black line: PIMC. Red markers: ASW

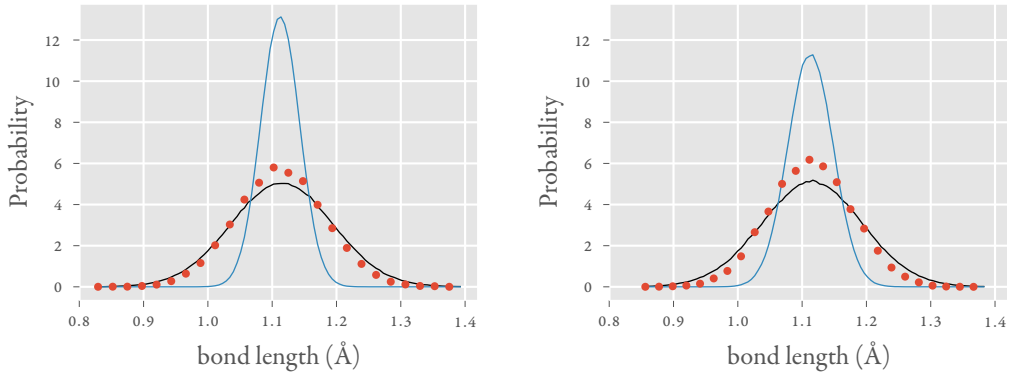

Figure 4.5: C —— H length distribution at 298 K (left) and 400 K (right). Blue line: Classical Boltzmann. Black line: PIMC. Red markers: ASW

Next, consider the carbon-carbon single and triple bond lengths. The corresponding distributions are given in Figure 4.3 and Figure 4.4 respectively. We notice that the average bond length remains the same irrespective of the sort of distribution we are looking at. However it is the spread that changes vastly between the classical and the quantum distributions. Both the quantum distributions are much broader, and their standard deviations remain constant over the temperature change. However, the classical Boltzmann distribution is much narrower at both temperatures, for both the bond length distributions, and its standard deviation increases with increasing temperature. For the C —— H bond as given in Figure 4.5, similar conclusions are obvious. However, here the ASW results do not match the PIMC results quantitatively. This is a result of anharmonicity, and increasing the switching time would make convergence better. Because of the softness of the potential, converging the potential energy distribution within acceptable levels does not converge the C —— H bond length distribution.

4.4 Discussion and concluding remarks

In this chapter, we have demonstrated the use of ASW for calculating the Wigner function for a molecule described by Hamiltonian in Cartesian coordinates. Thus, this method works for molecular systems described in both normal mode and Cartesian coordinates. We compared the potential energy distribution to exact PIMC calculations and the classical Boltzmann distribution. We note that ASW reproduces the PIMC results quite faithfully despite presence of anharmonicities. Bond vibrations are typically cold at room temperatures and we see that both in the ASW and PIMC results, the temperature dependence is largely absent. Thus ASW manages to capture ZPE effects fully.

Because ASW requires only localized knowledge of the PES, it is a very attractive possibility to use ASW with *ab initio* potential energy surfaces. The resulting simulation would have a very wide regime of applicability. The only restriction to such a simulation would be the *ab initio* electronic structure calculation which can be easily converged to high accuracy at any given geometry. Additional limitations on the types of interactions would be absent. All

relevant interactions can be incorporated fully quantum mechanically. Hence, it is an exciting prospect to couple this method to density functional theory (DFT) or other electronic structure methods which can give us the locally relevant Born-Oppenheimer surface on the fly.

Lastly, since the ASW procedure may be applied without modification to generate a quantized phase space distribution for a solvent as required in QCPI. If classical force fields are not available, *ab initio* evaluation of forces is the only option. In such cases, if the ZPE effects are important, the Wigner function would be very important. ASW may be used in such cases to calculate the phase space distribution of the solvent.

However, despite being a simple and attractive method, ASW is still approximate and results cannot be systematically improved. So, in Chapter 5, we discuss a method which would enable us to calculate the exact Wigner function of any operator, and would even allow us to simultaneously equilibrate a fully quantum system and a quasiclassical solvent.

Chapter 5

Path integral Wigner method

5.1 Introduction

We have till now been discussing an approximate method for calculating the Wigner distribution. There are many other methods for approximating the distribution with their individual limitations and strengths. However, there is no numerically exact method reported till now, which can be systematically converged to the required accuracy. Now we present a method for evaluating the Wigner transform for any arbitrary operator using path integrals. This path integral Wigner (PI-Wigner) method mitigates the sign problem inherent in a multidimensional Fourier transform to a certain extent, making it possible to numerically simulate the distribution. We will also be exploring the salient features of the method and how it converges.

The PI-Wigner method for a general thermalized operator is derived in Section 5.2. In Section 5.3, we present numerical examples to illustrate the method. An in-depth study of the convergence and salient features is done using one-dimensional potentials at various temperatures. Multidimensional examples are done for two cases. We apply this method for studying the equilibrium position-position correlation function of a harmonic oscillator that is coupled to a bath of harmonic oscillators in Section 5.3.2. Thereafter, we show the results for the marginal thermal position distributions of formamide in Section 5.3.3.

5.2 Path integral Wigner (PI-Wigner) method

Consider a general operator $\hat{\Omega}$ whose Wigner function, $\Omega_{\mathrm{W}}(q,p)$ is required. Calculating the Wigner function is difficult because of the multidimensional Fourier transform involved. However, it is comparatively easier to calculate the Husimi representation[11] of $\hat{\Omega}$, $\Omega_{\mathrm{H}}(q,p)$, where the phase is bound.

$$\Omega_{\mathrm{H}}(q,p) = \left\langle g_{q,p}\middle|\hat{\Omega}\middle|g_{q,p}\right\rangle \tag{5.2.1}$$

where $\left|g_{q,p}\right\rangle$ are the coherent states defined by the position space wavefunctions,

$$\left\langle q\middle|g_{q_0,p_0}\right\rangle = \left(\frac{\gamma}{\pi}\right)^{\frac{1}{4}} \exp\left(-\frac{\gamma}{2}\left(q-q_0\right)^2 + \frac{i}{\hbar}p_0\left(q-q_0\right)\right) \tag{5.2.2}$$

We give the expression in one dimension. The generalization to the multidimensional case is straightforward. To compute the Wigner function, its relationship[48] with the Husimi representation may be used

$$\Omega_{\mathrm{W}}(q,p) = \exp\left(-\frac{1}{4}\left(\frac{1}{\gamma}\frac{\partial^2}{\partial q^2} + \gamma\frac{\partial^2}{\partial p^2}\right)\right)\Omega_{\mathrm{H}}(q,p) \tag{5.2.3}$$

Solving Equation 5.2.3 exactly is equivalent to solving the full Wigner transform and hence computationally infeasible for multidimensional systems. However, it has been shown by Thoss et al.[49] that the first order truncation of this relationship is equivalent to the derivative forward-backward semiclassical dynamics method of Shao and Makri.[9]

Consider the case of a symmetrically thermalized operator, $\hat{\Omega}^{\beta} = e^{-\beta\hat{\mathrm{H}}/2}\hat{\Omega}e^{-\beta\hat{\mathrm{H}}/2}$. Rewriting Equation 5.2.3 for this case, we get

$$\Omega_{\mathrm{W}}^{\beta}(q,p) = \exp\left(-\frac{1}{4}\left(\frac{1}{\gamma}\frac{\partial^2}{\partial q^2} + \gamma\frac{\partial^2}{\partial p^2}\right)\right)\left\langle g_{q,p}\middle|e^{-\beta\hat{\mathrm{H}}/2}\hat{\Omega}e^{-\beta\hat{\mathrm{H}}/2}\middle|g_{q,p}\right\rangle \tag{5.2.4}$$

To get a path integral representation, we split the Boltzmann operator at an inverse temperature of $\beta = \frac{1}{k_{\mathrm{B}}\mathrm{T}}$ into N imaginary time slices with $\Delta\beta = \frac{\beta}{2\mathrm{N}}$.

$$e^{-\beta\hat{\mathrm{H}}/2} = \left(e^{-\Delta\beta\hat{\mathrm{H}}}\right)^{\mathrm{N}} \tag{5.2.5}$$

and by subsequent application of the Trotter formula for sufficiently small $\Delta\beta$, we get

$$e^{-\beta\hat{\mathrm{H}}/2} = \left(e^{-\Delta\beta\hat{\mathrm{T}}/2}e^{-\Delta\beta\hat{\mathrm{V}}}e^{-\Delta\beta\hat{\mathrm{T}}/2}\right)^{\mathrm{N}} \tag{5.2.6}$$

where $\hat{\mathrm{T}}$ and $\hat{\mathrm{V}}$ are the kinetic energy and potential energy operators respectively. Now we can write down the path integral representation for the Husimi function, $\Omega_{\mathrm{H}}^{\beta}(q,p)$.

$$\begin{aligned}
\Omega_{\mathrm{H}}^{\beta}(q,p) &= \left\langle g_{q,p}\middle|e^{-\beta\hat{\mathrm{H}}/2}\hat{\Omega}e^{-\beta\hat{\mathrm{H}}/2}\middle|g_{q,p}\right\rangle \\
&= \int\cdots\int \mathrm{d}x_1\ldots\mathrm{d}x_{2\mathrm{N}+2}\ \left\langle g_{q,p}\middle|e^{-\Delta\beta\hat{\mathrm{T}}/2}\middle|x_1\right\rangle e^{-\Delta\beta\mathrm{V}(x_1)} \\
&\times\ \left\langle x_1|e^{-\Delta\beta\hat{\mathrm{T}}}|x_2\right\rangle e^{-\Delta\beta\mathrm{V}(x_2)}\left\langle x_2|e^{-\Delta\beta\hat{\mathrm{T}}}|x_3\right\rangle\ldots\left\langle x_{\mathrm{N}}|e^{-\Delta\beta\hat{\mathrm{T}}/2}|x_{\mathrm{N}+1}\right\rangle \\
&\times\ \left\langle x_{\mathrm{N}+1}|\hat{\Omega}|x_{\mathrm{N}+2}\right\rangle\left\langle x_{\mathrm{N}+2}|e^{-\Delta\beta\hat{\mathrm{T}}/2}|x_{\mathrm{N}+3}\right\rangle e^{-\Delta\beta\mathrm{V}(x_{\mathrm{N}+3})}\ldots \\
&\times\ \left\langle x_{2\mathrm{N}+2}\middle|e^{-\Delta\beta\hat{\mathrm{T}}/2}\middle|g_{q,p}\right\rangle
\end{aligned} \tag{5.2.7}$$

By doing the Gaussian integrals, we get closed form expressions for the factors involving coherent states[50]

$$\left\langle x_{2\mathrm{N}+2}\middle|e^{-\Delta\beta\hat{\mathrm{T}}/2}\middle|g_{q,p}\right\rangle = \left(\frac{\gamma}{\pi}\right)^{1/4}\sqrt{\frac{2m}{2m+\hbar^2\Delta\beta\gamma}}$$

$$\times \exp\left(-\frac{2m}{2m+\hbar^2\Delta\beta\gamma}\left(\frac{\gamma}{2}\left(q-x_{2N+2}\right)^2+\frac{\Delta\beta}{4m}p^2+ip\left(q-x_{2N+2}\right)\right)\right) \tag{5.2.8}$$

Thus, the coherent state matrix element for the symmetrically thermalized operator A becomes in path integral representation

$$\begin{aligned}
\Omega_{\mathrm{H}}^{\beta}(q,p) &= \left(\frac{\gamma}{\pi}\right)^{1/2}\left(\frac{2m}{2m+\hbar^2\Delta\beta\gamma}\right)\int\cdots\int \mathrm{d}x_1\ldots\mathrm{d}x_{2N+2}\, e^{-\Delta\beta V(x_1)} \\
&\times \langle x_1|e^{-\Delta\beta\hat{T}}|x_2\rangle\, e^{-\Delta\beta V(x_2)}\,\langle x_2|e^{-\Delta\beta\hat{T}}|x_3\rangle\ldots\langle x_N|e^{-\Delta\beta\hat{T}/2}|x_{N+1}\rangle \\
&\times \langle x_{N+1}|\hat{\Omega}|x_{N+2}\rangle\,\langle x_{N+2}|e^{-\Delta\beta\hat{T}/2}|x_{N+3}\rangle\, e^{-\Delta\beta V(x_{N+3})}\ldots \\
&\times \exp\left(-\frac{2m}{2m+\hbar^2\Delta\beta\gamma}\left(\frac{\gamma}{2}\left(\left(q-x_1\right)^2+\left(q-x_{2N+2}\right)^2\right)+\frac{\Delta\beta}{4m}p^2+ip\left(x_1-x_{2N+2}\right)\right)\right) \qquad (5.2.9)\\
\Omega_{\mathrm{W}}^{\beta}(q,p) &= \left(\frac{\gamma}{\pi}\right)^{1/2}\left(\frac{2m}{2m+\hbar^2\Delta\beta\gamma}\right)\int\cdots\int \mathrm{d}x_1\ldots\mathrm{d}x_{2N+2}\, e^{-\Delta\beta V(x_1)} \\
&\times \langle x_1|e^{-\Delta\beta\hat{T}}|x_2\rangle\, e^{-\Delta\beta V(x_2)}\,\langle x_2|e^{-\Delta\beta\hat{T}}|x_3\rangle\ldots\langle x_N|e^{-\Delta\beta\hat{T}/2}|x_{N+1}\rangle \\
&\times \langle x_{N+1}|\hat{\Omega}|x_{N+2}\rangle\,\langle x_{N+2}|e^{-\Delta\beta\hat{T}/2}|x_{N+3}\rangle\, e^{-\Delta\beta V(x_{N+3})}\ldots \\
&\times \exp\left(-\frac{1}{4\gamma}\frac{\partial^2}{\partial q^2}\right)\exp\left(-\frac{2m}{2m+\hbar^2\Delta\beta\gamma}\left(\frac{\gamma}{2}\right)\left(\left(q-x_1\right)^2+\left(q-x_{2N+2}\right)^2\right)\right) \\
&\times \exp\left(-\frac{\gamma}{4}\frac{\partial^2}{\partial p^2}\right)\exp\left(-\frac{2m}{2m+\hbar^2\Delta\beta\gamma}\left(\frac{\Delta\beta}{4m}p^2+ip\left(x_1-x_{2N+2}\right)\right)\right) \qquad (5.2.10)
\end{aligned}$$

The separation of the q and the p part of the derivatives is possible because q and p over here are not operators but just coherent state label variables. So, there are no commutation issues to be taken care of. We directly solve the exponentials of the derivatives exactly because they are Gaussian functions. Consider a general exponential operator, $e^{-\eta\partial_y^2}$ acting on a general Gaussian function, $\psi(y)=e^{-ay^2+by}$, where $a>0, b\in\mathbb{C}$. Then ψ in the reciprocal space is given as

$$\begin{aligned}
\psi(k) &= \frac{1}{\sqrt{2\pi}}\int \mathrm{d}y\,\psi(y)\,e^{iky} = \frac{1}{\sqrt{2a}}\,\exp\left\{\frac{(b+ik)^2}{4a}\right\} \\
e^{-\eta\partial_y^2}\psi(y) &= \frac{1}{\sqrt{2\pi}}\int \mathrm{d}k\,\psi(k)\,e^{-\eta\partial_y^2}e^{-iky} = \frac{1}{\sqrt{2\pi}}\int \mathrm{d}k\,\psi(k)\,e^{\eta k^2}e^{-iky} \\
&= \frac{1}{\sqrt{4\pi a}}\,e^{\frac{b^2}{4a}}\int dk\, e^{-\left(\frac{1}{4a}-\eta\right)k^2}\,e^{-i\left(y-\frac{b}{2a}\right)k} \\
&= \frac{e^{\frac{b^2}{4a}}}{\sqrt{1-4\eta a}}\,\exp\left\{-\frac{a}{(1-4\eta a)}\left(y-\frac{b}{2a}\right)^2\right\}, \quad \text{if } 4\eta a<1
\end{aligned} \tag{5.2.11}$$

Applying Equation 5.2.11 to Equation 5.2.10, we can simplify the expressions to the following

$$\exp\left(-\frac{1}{4\gamma}\frac{\partial^2}{\partial q^2}\right)\exp\left(-\frac{2m}{2m+\hbar^2\Delta\beta\gamma}\left(\frac{\gamma}{2}\right)\left((q-x_1)^2+(q-x_{2N+2})^2\right)\right)$$
$$=\sqrt{\frac{2m+\Delta\beta\gamma}{\Delta\beta\gamma}}\exp\left(-\frac{2m}{\Delta\beta}\left(q-\frac{x_1+x_{2N+2}}{2}\right)^2\right)\exp\left(-\frac{m\gamma}{2\left(2m+\Delta\beta\gamma\right)}\left(x_1-x_{2N+2}\right)^2\right) \tag{5.2.12}$$
$$\exp\left(-\frac{\gamma}{4}\frac{\partial^2}{\partial p^2}\right)\exp\left(-\frac{2m}{2m+\hbar^2\Delta\beta\gamma}\left(\frac{\Delta\beta}{4m}p^2+ip\left(x_1-x_{2N+2}\right)\right)\right)$$
$$=\sqrt{\frac{2m+\Delta\beta\gamma}{2m}}\exp\left(-\Delta\beta\frac{p^2}{2m}-ip\left(x_1-x_{2N+2}\right)\right)\exp\left(\frac{m\gamma}{2\left(2m+\Delta\beta\gamma\right)}\left(x_1-x_{2N+2}\right)^2\right) \tag{5.2.13}$$

Notice that the Gaussian spring-like term holding x_1 close to x_{2N+2} in Equation 5.2.12 is exactly canceled by its reciprocal present in Equation 5.2.13. This is what leads to unbound phase causing the "sign" problem in multidimensional systems. However, because of the nature of the Boltzmannized operator, we know that the end points of the path integral necklace cannot be very far from each other. So, we expand the inverse Gaussian in Equation 5.2.13 in a truncated polynomial upto a finite order, n_x. We introduce a new notation preempting our next step and consolidate all the terms into

$$\begin{aligned}\Omega^{\beta}_{W,n_xX,\infty P}\left(q,p\right)=&\left(\frac{2m}{\pi\Delta\beta}\right)^{1/2}\int\cdots\int dx_1\ldots dx_{2N+2}\,e^{-\Delta\beta V(x_1)}\\
&\times\ \langle x_1|e^{-\Delta\beta\hat{T}}|x_2\rangle\,e^{-\Delta\beta V(x_2)}\,\langle x_2|e^{-\Delta\beta\hat{T}}|x_3\rangle\ldots\langle x_N|e^{-\Delta\beta\hat{T}/2}|x_{N+1}\rangle\\
&\times\ \langle x_{N+1}|\hat{\Omega}|x_{N+2}\rangle\ \langle x_{N+2}|e^{-\Delta\beta\hat{T}/2}|x_{N+3}\rangle\,e^{-\Delta\beta V(x_{N+3})}\ldots\\
&\times\exp\left(-\frac{m\gamma}{2\left(2m+\Delta\beta\gamma\right)}\left(x_1-x_{2N+2}\right)^2\right)\exp\left(-\frac{2m}{\Delta\beta}\left(q-\frac{x_1+x_{2N+2}}{2}\right)^2\right)\\
&\times\exp\left(-\Delta\beta\frac{p^2}{2m}\right)\left(\sum_{j=0}^{n_x}\frac{1}{j!}\left(\frac{m\gamma}{2\left(2m+\Delta\beta\gamma\right)}\left(x_1-x_{2N+2}\right)^2\right)^j+\mathcal{O}\left(\left(x_1-x_{2N+2}\right)^{2n_x+1}\right)\right)\\
&\times\exp\left(ip\left(x_1-x_{2N+2}\right)\right)\end{aligned} \tag{5.2.14}$$

In Equation 5.2.14, we notice that there is a Gaussian factor holding x_1 close to x_{2N+2}. This Gaussian factor decays much faster than any finite ordered polynomial would. Therefore, $(x_1 - x_{2N+2})$ is bound, as is p. Therefore the phase is bound. However, notice that at low temperatures, we are still sampling a high temperature classical momentum distribution, which is much broader than the true quantum distribution. The latter is obtained because of the phase cancellation. So, this additional broadening can lead to extra "sign" problem. To take care of that we multiply and divide by a more "correct" momentum factor and expand whatever remains in a truncated polynomial,

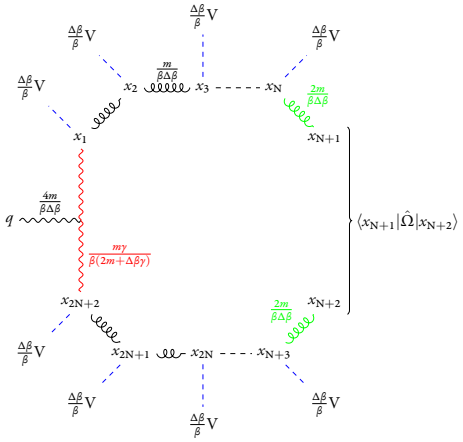

Figure 5.1: Schematic diagram for the coordinate space part of the sampling function in Equation 5.2.15. Wavy lines are the springs. Different spring constants (noted on top of the springs) are denoted by different types of windings of the springs. Red spring also has the polynomial correction factor associated with it.

leading to

$$\begin{aligned}
\Omega^{\beta}_{\mathrm{W},n_x\mathrm{X},n_p\mathrm{P}}(q,p) = &\left(\frac{2m}{\pi\Delta\beta}\right)^{1/2}\int\cdots\int \mathrm{d}x_1\ldots\mathrm{d}x_{2\mathrm{N}+2}\, e^{-\Delta\beta\mathrm{V}(x_1)} \\
&\times \langle x_1|e^{-\Delta\beta\hat{\mathrm{T}}}|x_2\rangle\, e^{-\Delta\beta\mathrm{V}(x_2)}\, \langle x_2|e^{-\Delta\beta\hat{\mathrm{T}}}|x_3\rangle\ldots\langle x_{\mathrm{N}}|e^{-\Delta\beta\hat{\mathrm{T}}/2}|x_{\mathrm{N}+1}\rangle \\
&\times \langle x_{\mathrm{N}+1}|\hat{\Omega}|x_{\mathrm{N}+2}\rangle\ \langle x_{\mathrm{N}+2}|e^{-\Delta\beta\hat{\mathrm{T}}/2}|x_{\mathrm{N}+3}\rangle\, e^{-\Delta\beta\mathrm{V}(x_{\mathrm{N}+3})}\ldots \\
&\times \exp\left(-\frac{m\gamma}{2\,(2m+\Delta\beta\gamma)}\,(x_1-x_{2\mathrm{N}+2})^2\right)\exp\left(-\frac{2m}{\Delta\beta}\left(q-\frac{x_1+x_{2\mathrm{N}+2}}{2}\right)^2\right) \\
&\times \exp\left(-\beta\frac{p^2}{2m}\right)\left(\sum_{j=0}^{n_p}\frac{1}{j!}\left((\beta-\Delta\beta)\frac{p^2}{2m}\right)^j+\mathcal{O}\left(p^{2n_p+1}\right)\right) \\
&\times \left(\sum_{j=0}^{n_x}\frac{1}{j!}\left(\frac{m\gamma}{2\,(2m+\Delta\beta\gamma)}\,(x_1-x_{2\mathrm{N}+2})^2\right)^j+\mathcal{O}\left((x_1-x_{2\mathrm{N}+2})^{2n_x+1}\right)\right) \\
&\times \exp\left(ip\,(x_1-x_{2\mathrm{N}+2})\right)
\end{aligned} \tag{5.2.15}$$

where n_x and n_p are two different truncation parameters in terms of which convergence needs to be tested. All but the last line of Equation 5.2.15 is used as the sampling function. The pure phase part is treated as the Monte Carlo integrand. In Equation 5.2.15, we have used the momentum part of the classical Boltzmann distribution as the "reference" distribution, however the method can be written in terms of any other "reference" momentum distributions. A very lucrative alternative, in cases where the harmonic fit is a good approximation to the full Hamiltonian, is the momentum part of the harmonic Wigner function. In Figure 5.1, we show a schematic for the sampling function of the position coordinates. There are subtle differences from the standard quantum-classical isomorphism. For instance, not all the "springs" have the same spring constant. This is indicated in the different colors and shapes of the springs used. For the rest of the chapter, we use $\mathrm{W}_{n_x\mathrm{X},n_p\mathrm{P}}$ for the case where $\hat{\Omega}=\hat{\mathcal{I}}$, the identity operator.

5.3 Applications to model systems

In this section, we present some numerical tests of the PI-Wigner method.

5.3.1 One-dimensional anharmonic oscillators

We demonstrate the method on two different one-dimensional potentials

$$\mathrm{V}_1(x) = \frac{1}{2}\omega^2 x^2 - 0.2x^3 + 0.015x^4 \text{ and } \mathrm{V}_2(x) = \frac{1}{2}\omega^2 x^2 - 0.1x^3 + 0.1x^4 \tag{5.3.1}$$

where $\omega = \sqrt{2}$. In Figure 5.2, we present the phase space distribution at different temperatures for both potentials. We compare the position and the momentum distributions to basis set and classical Boltzmann distribution

$$\mathrm{P}_p(x) = \int \mathrm{d}p\, \mathrm{W}(x,p), \quad \mathrm{P}_x(p) = \int \mathrm{d}x\, \mathrm{W}(x,p). \tag{5.3.2}$$

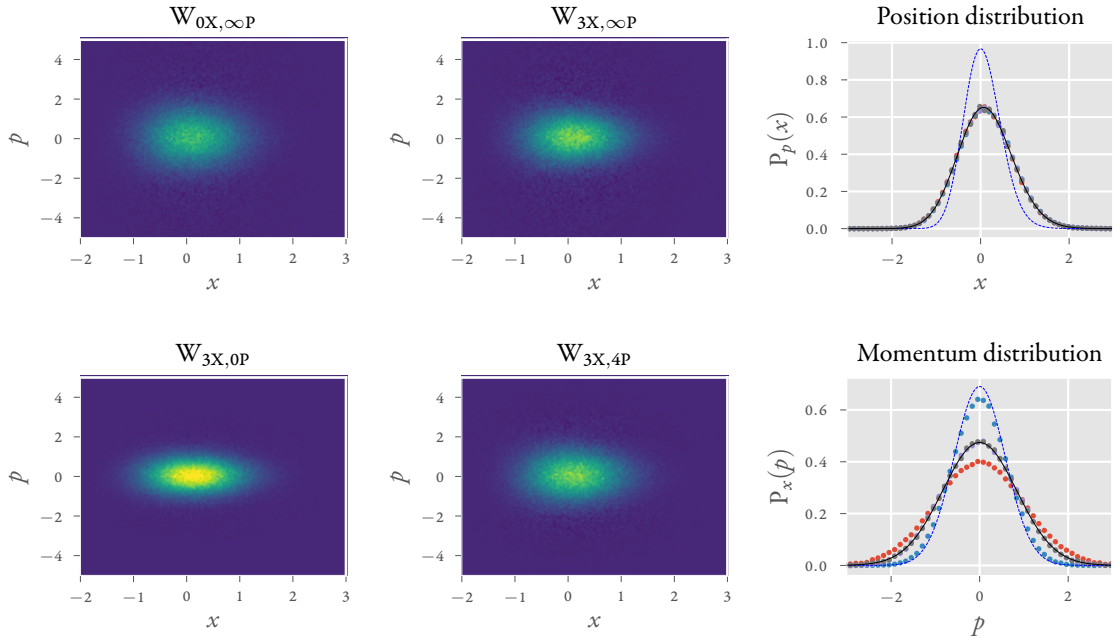

(a) $\hbar\omega\beta = 3\sqrt{2}$, V_1 potential using 14 beads

Figure 5.2: Phase space density, with the position (top) and momentum (bottom) distribution, obtained by $\mathrm{W}_{0\mathrm{X},\infty\mathrm{P}}$ (top left, red markers), $\mathrm{W}_{3\mathrm{X},\infty\mathrm{P}}$ (top right, gray markers), $\mathrm{W}_{3\mathrm{X},0\mathrm{P}}$ (bottom left, blue markers), $\mathrm{W}_{3\mathrm{X},4\mathrm{P}}$ (bottom right, violet markers). Solid black line: basis set calculation, dashed blue line: classical Boltzmann density.

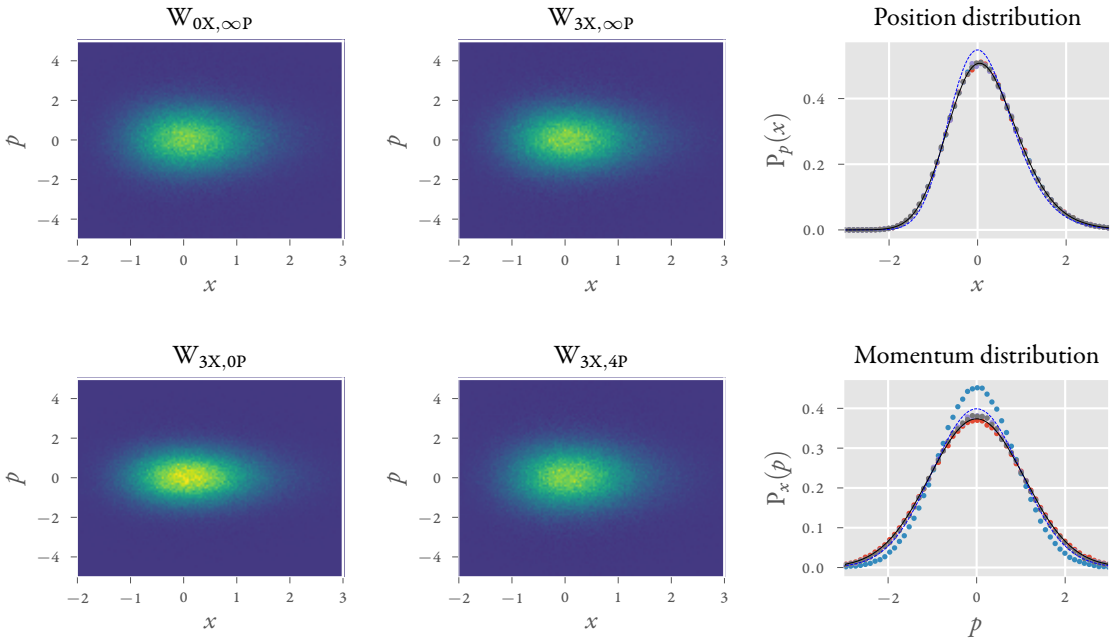

(b) $\hbar\omega\beta = \sqrt{2}$, V_1 potential using 3 beads

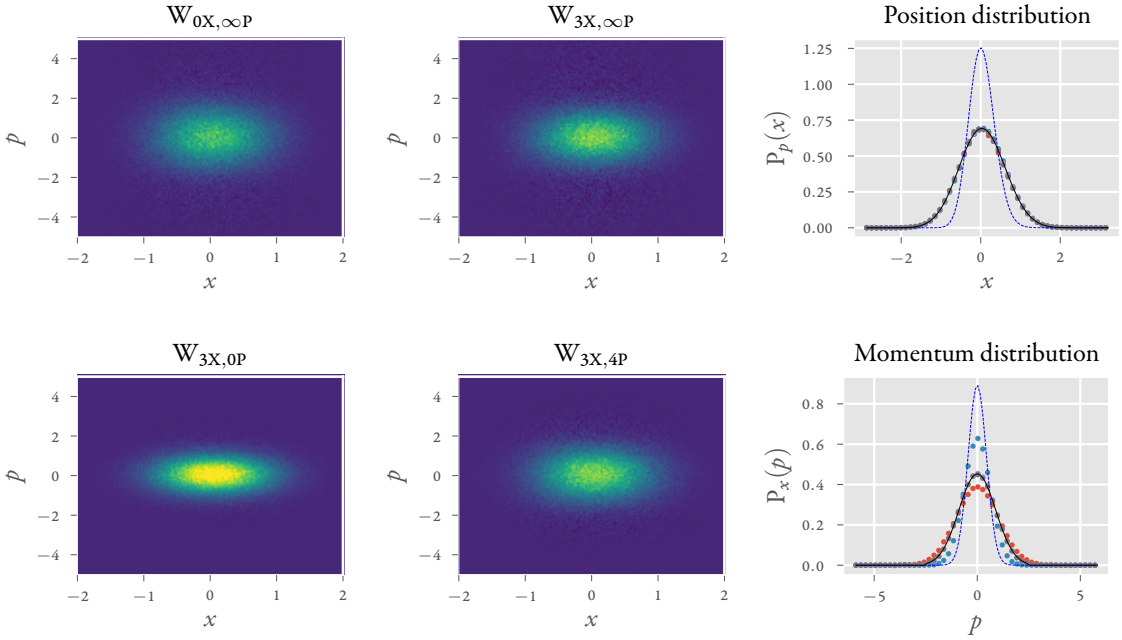

(c) $\hbar\omega\beta = 5\sqrt{2}$, V_2 potential using 24 beads

Figure 5.2: continued

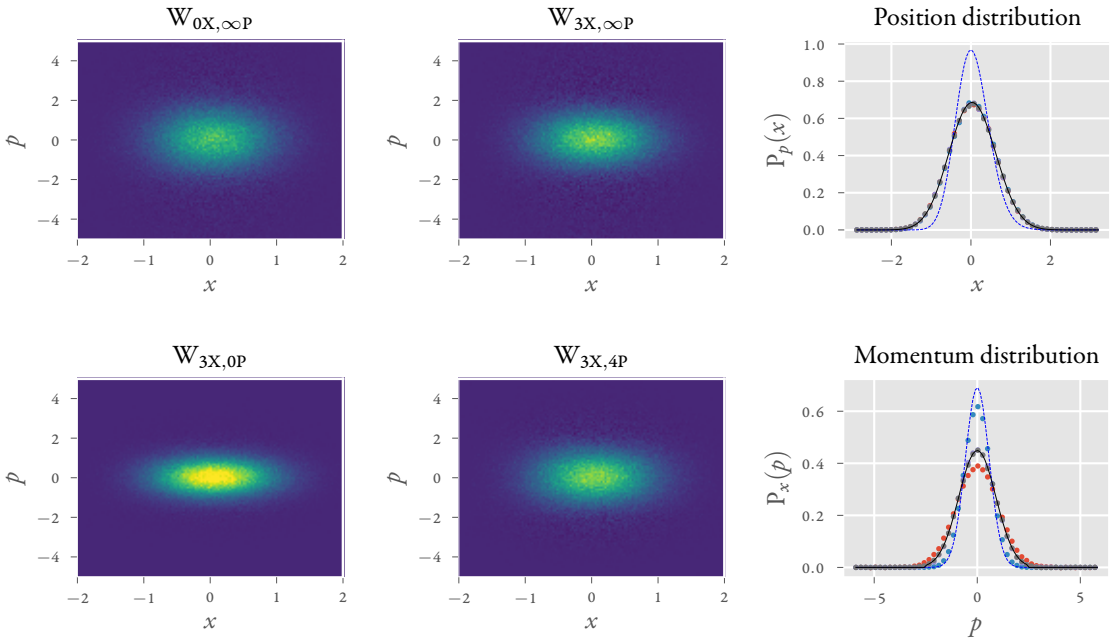

(d) $\hbar\omega\beta = 3\sqrt{2}$, V_2 potential using 14 beads

Figure 5.2: continued

We see in Figure 5.2 that the PI-Wigner method converges for over a large range of temperatures to the correct distribution. At low temperatures, the number of beads required to minimize the Trotter error increases, which leads to larger phase. In these examples we show that we have sufficiently reduced the phase so that the distribution converges well even for 24 beads. Previously we had discussed the inability of the ASW method to capture delicate quantum effects like the slight shift of the distribution maximum. The PI-Wigner method, being a numerically exact method is able to accurately capture all these effects. It is also interesting to note the effect of momentum truncation. It makes the momentum distribution more classical-like. Thus we see that at low temperatures the momentum distribution corresponding to $W_{3X,0P}$ resembles the classical momentum distribution. However it has no effect on the position distribution. We demonstrate the effect of the momentum truncation by looking at the joint probability distribution of momentum and phase in Figure 5.3. Slices are taken along the Re phase $= \pm 1$ axis. The area under the Re phase $= -1$ curve is a measure of the amount of sign problem. We notice that for $W_{3X,\infty P}$, the area is the maximum as expected, and for $W_{3X,0P}$ it is the minimum. Also at low temperatures, even at converged levels of momentum truncation, the area under the Re phase $= -1$ curve is much smaller than that of $W_{3X,\infty P}$. This illustrates the reduction of the "sign" problem for these two Hamiltonians.

Effect of momentum truncation on dynamics

It is also instructive to study the effect of momentum truncation on the dynamics. Of course for a one-dimensional Hamiltonian, the effects of sign problem would be heavily muted, but there might be small indications of improvement.

Consider the correlation function

$$\mathrm{Re}\,\langle p(0)p(t)\rangle = \iint \mathrm{d}x_0\,\mathrm{d}p_0\,\mathrm{W}\,(x_0,p_0)\,p_0 p(t) \tag{5.3.3}$$

$p(t)$ in Equation 5.3.3 is computed by propagating classical trajectories. In Figure 5.5 we compare the results using $\mathrm{W}_{3\mathrm{X},\infty\mathrm{P}}$ and $\mathrm{W}_{3\mathrm{X},4\mathrm{P}}$ with those obtained by doing classical propagation on the numerically exact Wigner distribution. 100000 Monte Carlo points were employed. We can clearly see that in the left panel, where the temperature is slightly higher, there is not much difference between $\mathrm{W}_{3\mathrm{X},\infty\mathrm{P}}$ and $\mathrm{W}_{3\mathrm{X},4\mathrm{P}}$, however in the right panel, at $\hbar\omega\beta = 5$, there is noticeable errors in the $\mathrm{W}_{3\mathrm{X},\infty\mathrm{P}}$ calculations. These are absent in $\mathrm{W}_{3\mathrm{X},4\mathrm{P}}$ calculation. This is a very small error that we are talking about. However, things get only worse as we go higher in dimensionality.

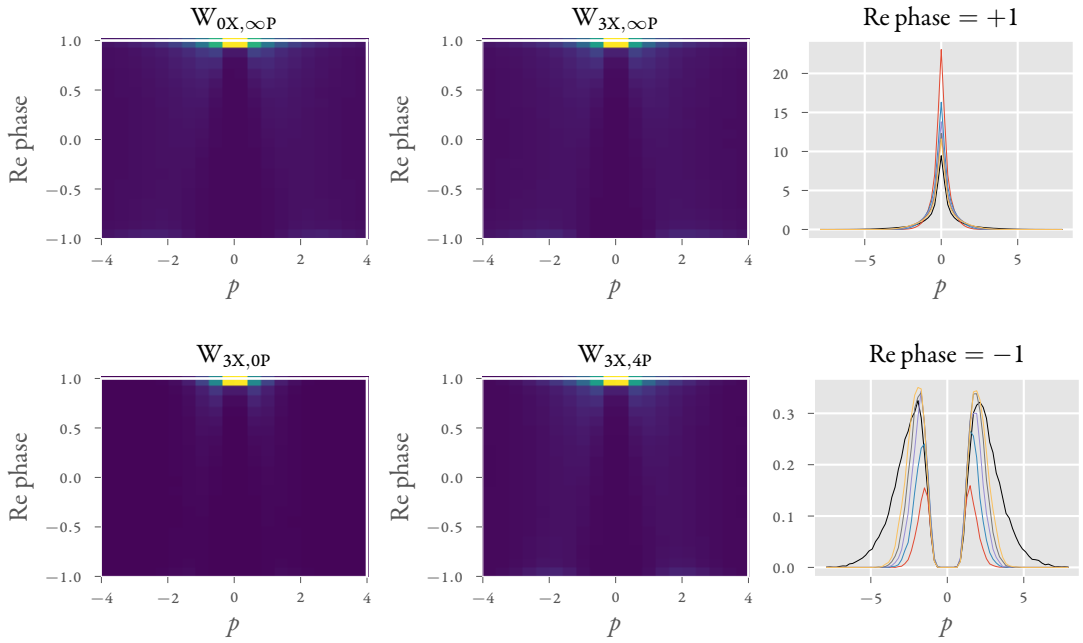

(a) $\hbar\omega\beta = 3\sqrt{2}$, V_1 potential using 14 beads

Figure 5.3: 2D histograms of momentum vs the real part of the phase, along with a slice at Re phase $= 1$ (top) and Re phase $= -1$ (bottom), obtained by $\mathrm{W}_{0\mathrm{X},\infty\mathrm{P}}$ (top left), $\mathrm{W}_{3\mathrm{X},\infty\mathrm{P}}$ (top right, black line), $\mathrm{W}_{3\mathrm{X},0\mathrm{P}}$ (bottom left, red line), $\mathrm{W}_{3\mathrm{X},1\mathrm{P}}$ (blue line), $\mathrm{W}_{3\mathrm{X},2\mathrm{P}}$ (violet line), $\mathrm{W}_{3\mathrm{X},3\mathrm{P}}$ (gray line), $\mathrm{W}_{3\mathrm{X},4\mathrm{P}}$ (bottom right, yellow line).

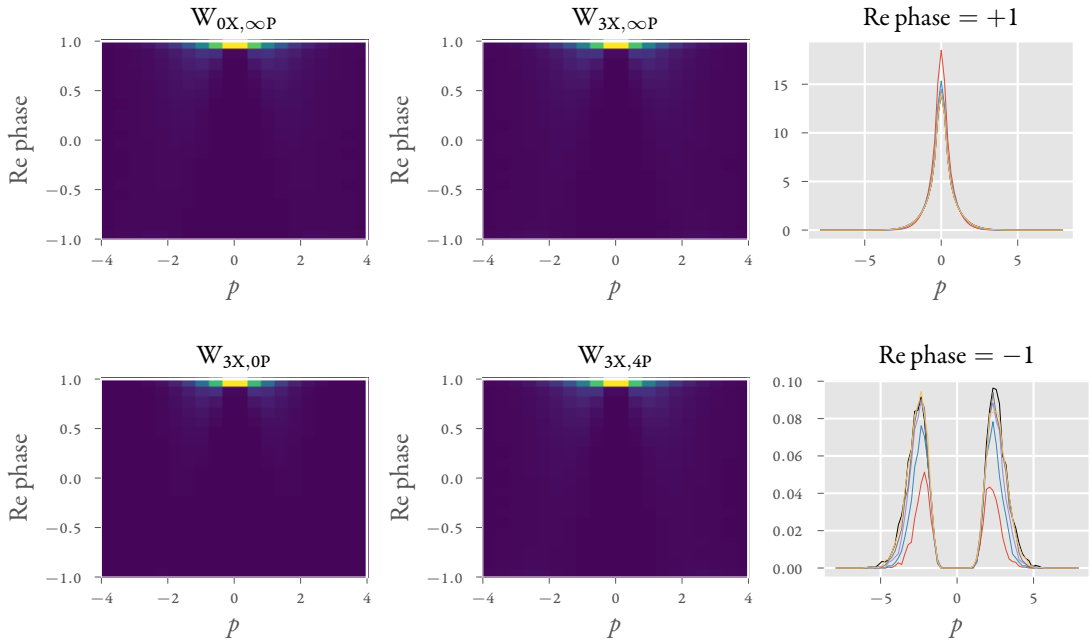

(b) $\hbar\omega\beta = \sqrt{2}$, V_1 potential using 3 beads

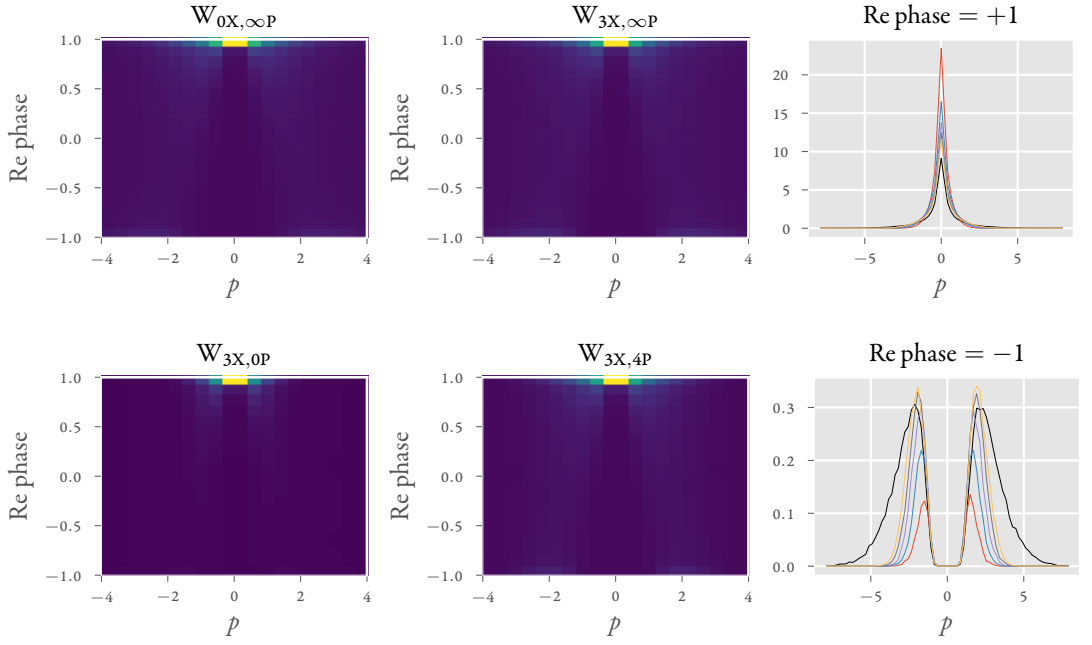

(c) $\hbar\omega\beta = 5\sqrt{2}$, V_2 potential using 24 beads

Figure 5.3: continued

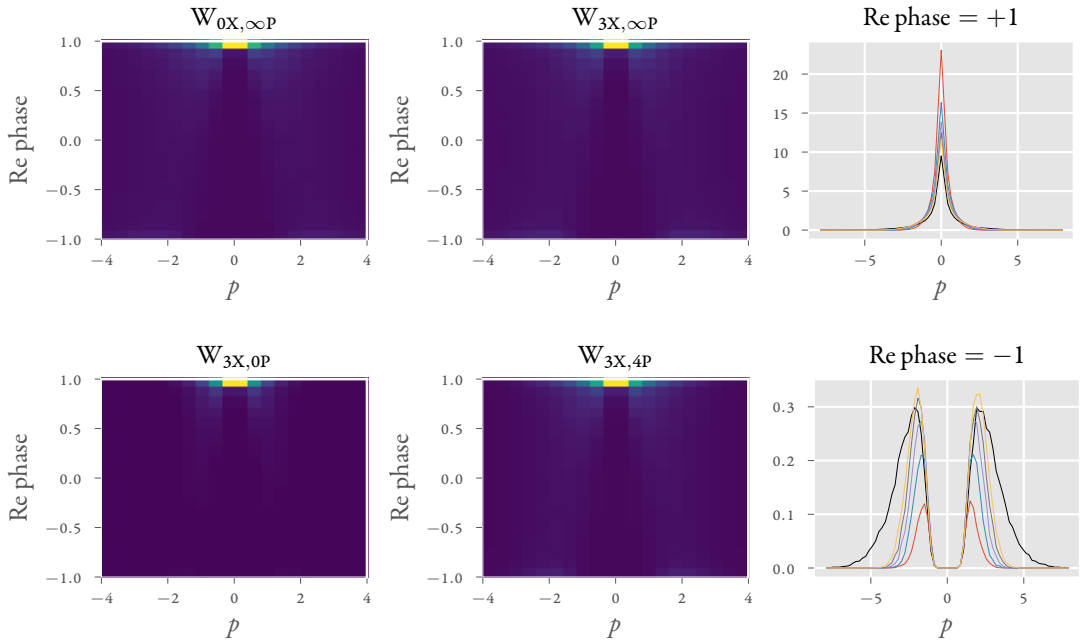

(a) $\hbar\omega\beta = 3\sqrt{2}$, V_2 potential using 14 beads

Figure 5.4: continued

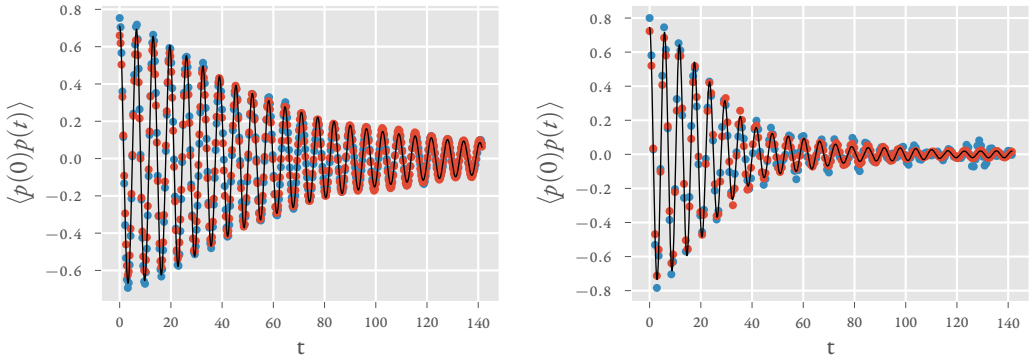

(a) V_1 at $\hbar\omega\beta = 3\sqrt{2}$

(b) V_2 at $\hbar\omega\beta = 5\sqrt{2}$

Figure 5.5: Momentum correlation function for 1D anharmonic oscillator. Black solid line: classical propagation of numerically exact Wigner distribution. Blue markers: classical propagation of $W_{3X,\infty P}$. Red markers: classical propagation of $W_{3X,4P}$. 100000 Monte Carlo points used in each case.

5.3.2 Multidimensional system-bath

As the first example of a multidimensional problem, we use the PI-Wigner method to generate the Wigner function and dynamics for a harmonic system coupled to a dissipative bath. The Hamiltonian has the form

$$\hat{\mathrm{H}} = \hat{\mathrm{H}}^{(0)} - \sum_j c_j \hat{s}\hat{x}_j; \quad \hat{\mathrm{H}}^{(0)} = \frac{\hat{p}_s^2}{2m} + \frac{1}{2}m\Omega^2\hat{s}^2 + \sum_j \frac{\hat{p}_j^2}{2m} + \frac{1}{2}m\omega_j^2\hat{x}_j^2 \tag{5.3.4}$$

where $m = 1, \Omega = 2$. The frequencies and the system-bath coupling coefficients are collectively specified by the spectral density.[38] We use the Ohmic form,

$$\mathrm{J}(\omega) = \frac{\pi}{2}\hbar\xi\omega \exp\left(-\frac{\omega}{\omega_c}\right) \tag{5.3.5}$$

with the cutoff frequency $\omega_c = 1.25\Omega$. The bath was discretized using 24 oscillators with frequencies chosen according to the logarithmic discretization of the spectral density[39] with $\omega_{max} = 4\omega_c$. We show the results of the discretization with varying numbers of oscillators at different parameters by reporting the real part of the position - position correlation function for the system, approximated by the classical Wigner procedure as

$$\mathrm{Re}\,\mathrm{C}(t) = \iint \mathrm{d}s_0\,\mathrm{d}p_{s,0} \prod_j \iint \mathrm{d}x_{j,0}\,\mathrm{d}p_{j,0}\,\mathrm{W}\left(s_0, p_{s,0}, \{x_{j,0}, p_{j,0}\}\right)\, s_0\, s(t) \tag{5.3.6}$$

Comparisons with the classical results and the analytically solved quantum correlation function is shown in Figure 5.6. We see that at both the different coupling parameters, the PI-Wigner simulation at $\mathrm{W}_{2\mathrm{X},0\mathrm{P}}$ level agrees with the true quantum results.

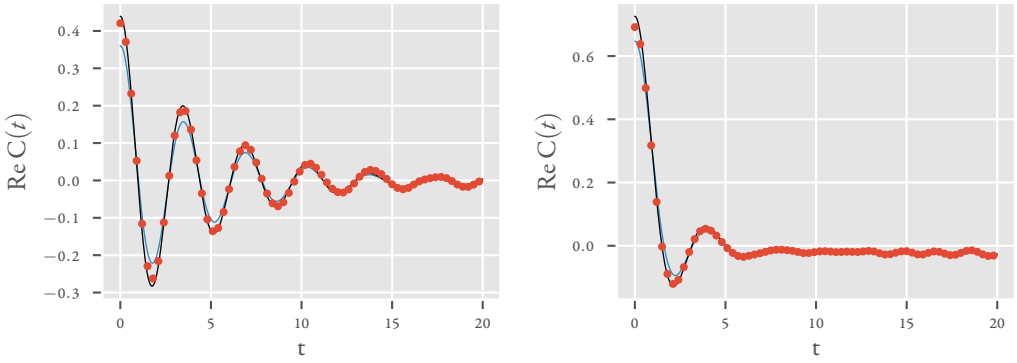

Figure 5.6: Correlation function for a harmonic system coupled with a harmonic bath. Black solid line: Exact quantum results. Blue line: Classical Boltzmann results. Red markers: $\mathrm{W}_{2\mathrm{X},0\mathrm{P}}$. Left panel: $\omega_c = 2.5, \xi = 0.5, \beta = 1$ with 29 bath modes. Right panel: $\omega_c = 2.5, \xi = 1, \beta = 1$ with 24 bath modes.

5.3.3 Quartic force field for formamide

As a final example, consider the *ab initio* quartic force field for the formamide molecule. The potential is calculated using Gaussian09 at the level of Møller-Plesset (MP2) perturbation theory with aug-ccpvtz basis set. The Hamiltonian is in normal mode coordinates and of the following form

$$\hat{\mathrm{H}} = \hat{\mathrm{H}}_0 + \hat{\mathrm{V}} \tag{5.3.7}$$

$$\hat{\mathrm{H}}_0 = \sum_{i=1}^{n} \frac{\hat{p}_i^2}{2} + \frac{1}{2} f_{ii} \hat{q}_i^2 + \frac{1}{6} f_{iii} \hat{q}_i^3 + \frac{1}{24} f_{iiii} \hat{q}_i^4 \tag{5.3.8}$$

$$\begin{aligned} \hat{\mathrm{V}} = &\sum_{i \neq j \neq k} f_{ijk} \hat{q}_i \hat{q}_j \hat{q}_k + \sum_{i \neq j} \frac{1}{2} f_{iij} \hat{q}_i^2 \hat{q}_j + \sum_{i \neq j \neq k \neq l} f_{ijkl} \hat{q}_i \hat{q}_j \hat{q}_k \hat{q}_l \\ &+ \sum_{i \neq j} \left(\frac{1}{6} f_{iiij} \hat{q}_i^3 \hat{q}_j + \frac{1}{4} f_{iijj} \hat{q}_i^2 \hat{q}_j^2 \right) + \sum_{i \neq j \neq k} \frac{1}{2} f_{iijk} \hat{q}_i^2 \hat{q}_j \hat{q}_k \end{aligned} \tag{5.3.9}$$

There are no quadratic couplings between the coordinates because the Hamiltonian is in normal mode coordinates, which diagonalize the harmonic terms. Here we report the thermal marginal distributions of the various modes

$$\mathrm{P}_i(q_i) = \int_{-\infty}^{\infty} \mathrm{d}q_1 \ldots \int_{-\infty}^{\infty} \mathrm{d}q_{i-1} \int_{-\infty}^{\infty} \mathrm{d}q_{i+1} \ldots \int_{-\infty}^{\infty} \mathrm{d}q_n \int_{-\infty}^{\infty} \mathrm{d}p_1 \ldots \int_{-\infty}^{\infty} \mathrm{d}p_n \, \mathrm{W}(q_1, \ldots, q_n, p_1, \ldots, p_n) \tag{5.3.10}$$

obtained using the PI-Wigner method along with the corresponding PIMC results and the Wigner distributions corresponding to the harmonic part of the Hamiltonian at room temperature ($\mathrm{T} = 300\mathrm{K}$).

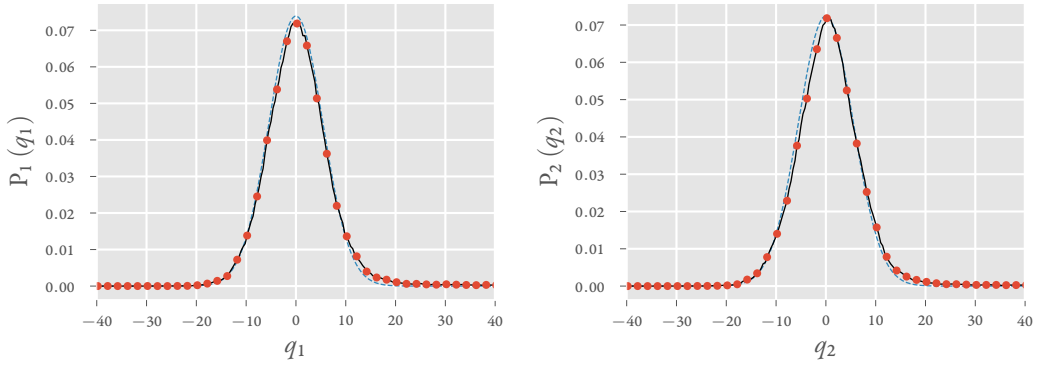

Figure 5.7: Marginal position distributions of the twelve normal modes of formamide at 300K. At this temperature $\hbar\omega_{\mathrm{min}}\beta = 0.64$ and $\hbar\omega_{\mathrm{max}}\beta = 18.06$. Black solid line: fully quantum PIMC results. Blue dashed line: harmonic Wigner distribution. Red markers: $\mathrm{W}_{\mathrm{2X,0P}}$ distribution.

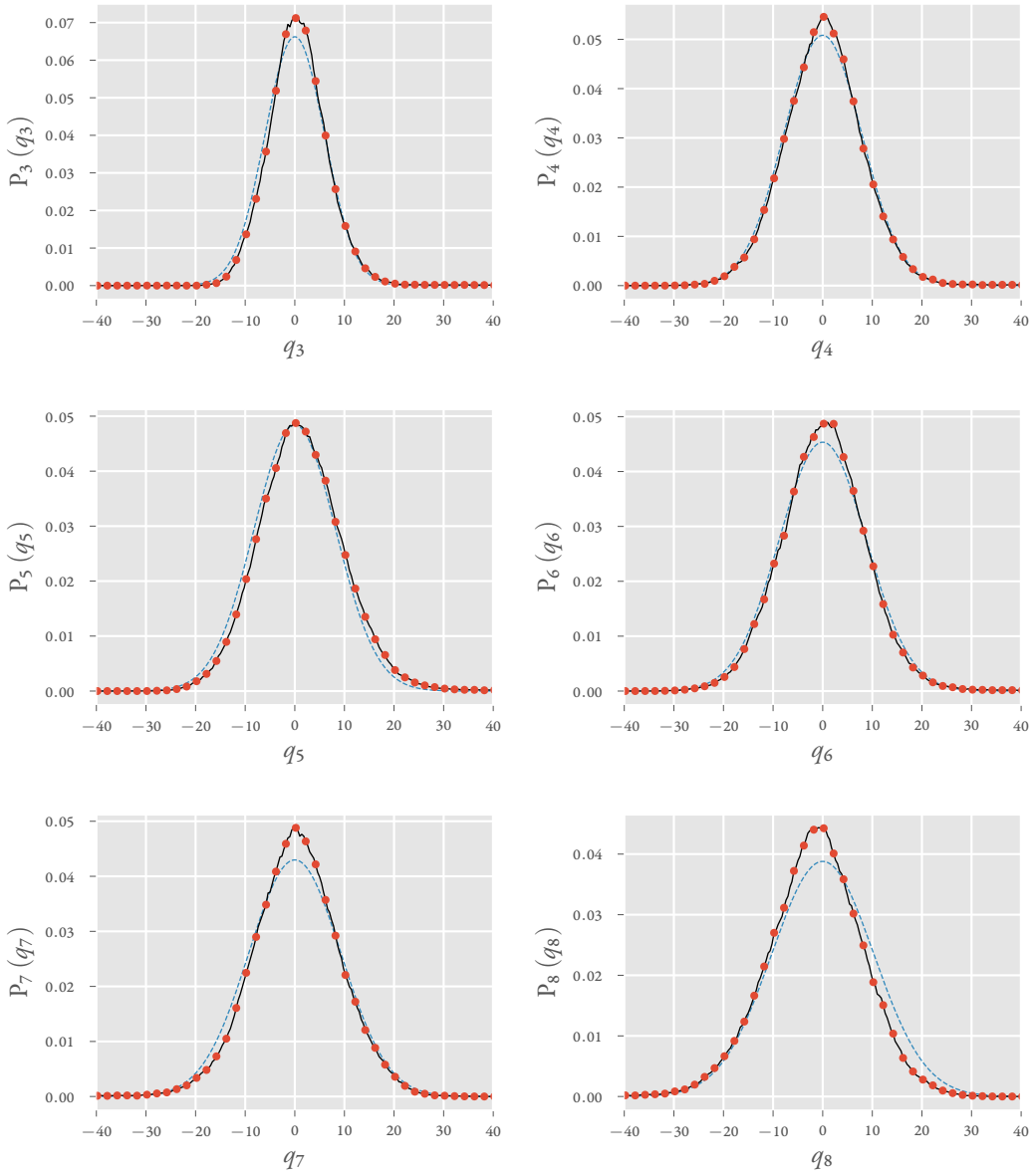

Figure 5.7: continued

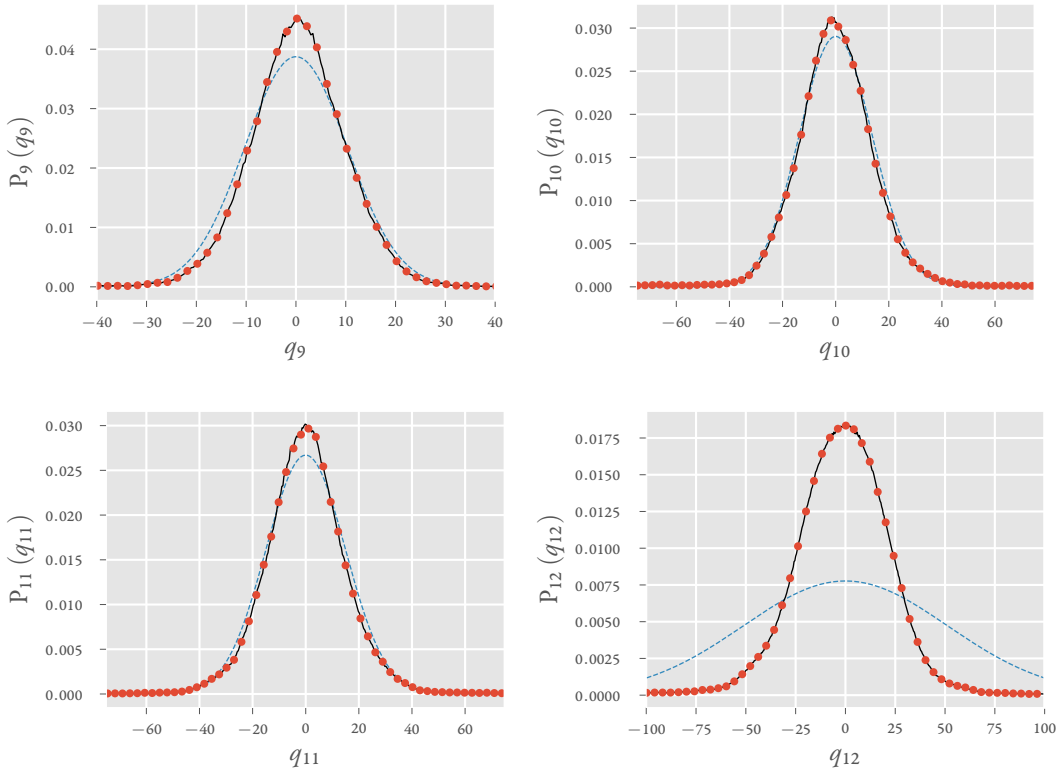

Figure 5.7: continued

Because of the difference in the diagonal parts of the Hamiltonian, different number of beads were used for the different modes. The PI-Wigner distribution was calculated at the level of $W_{2X,0P}$ using the harmonic Wigner momentum distribution as a reference. We see as expected that the comparatively low frequency modes explore highly anharmonic regions of the potential energy surface and thus show strong effects of anharmonicity. The number of PIMC beads used is 420. The Fourier transform involved in calculating the Wigner distribution is, of course, carried out over the 12 dimensional space spanned by the normal modes. The results, even at a relatively low order ($W_{2X,0P}$), match the exact PIMC results remarkably accurately.

5.4 Discussion and concluding remarks

In this final chapter of the part on Wigner functions, we have developed a very simple path integral method for calculating the distribution corresponding to thermal operators. The PI-Wigner method is numerically exact. It is heartening to see the sign problem mitigated to a sufficient extent to make it possible to calculate the full 24 dimensional Wigner distribution for formamide easily. It is easy to systematically converge the PI-Wigner method

at increased computational cost. A few of the problems that plague the ASW method are alleviated here, since the PI-Wigner method is numerically exact. Firstly, unlike ASW it does not require a good zeroth Hamiltonian. This makes the current method extremely attractive for application to liquids and clusters, where it is difficult to define a good zeroth Hamiltonian. Liquids prove to be additionally challenging to ASW because of the existence of inverted modes. We expect that the PI-Wigner method should work well in case of liquids too. Also, it can couple a discrete quantum system with a bath with a Wigner phase space representation. We are in the process of applying this method to clusters and quasi-classical liquids. Lastly, for quantum liquids, fermionic and bosonic exchanges are important. These cannot be incorporated in the ASW method. We are also working on ways of extending the PI-Wigner method to quantum fluids.

References

[1] A. Bose and N. Makri, "Wigner phase space distribution via classical adiabatic switching", J. Chem. Phys. **143**, 114114 (2015).

[2] H. Wang, X. Sun, and W. H. Miller, "Semiclassical approximations for the calculation of thermal rate constants for chemical reactions in complex molecular systems", J. Chem. Phys. **108**, 9726–9736 (1998).

[3] X. Sun, H. Wang, and W. H. Miller, "Semiclassical theory of electronically nonadiabatic dynamics: Results of a linearized approximation to the initial value representation", J. Chem. Phys. **109**, 7064–7074 (1998).

[4] W. Miller, "Generalization of the linearized approximation to the semiclassical initial value representation for reactive flux correlation functions", J. Phys. Chem. A **103**, 9384–9387 (1999).

[5] E. Wigner, "Calculation of the Rate of Elementary Association Reactions", J. Chem. Phys. **5**, 720–725 (1937).

[6] E. J. Heller and R. C. Brown, "Errors in the Wigner Approach to Quantum Dynamics", J. Chem. Phys. **75**, 1048–1050 (1981).

[7] J. A. Poulsen, G. Nyman, and P. J. Rossky, "Practical evaluation of condensed phase quantum correlation functions: A Feynman-Kleinert variational linearized path integral method", J. Chem. Phys. **119**, 12179–12193 (2003).

[8] N. Makri and K. Thompson, "Semiclassical influence functionals for quantum systems in anharmonic environments", Chem. Phys. Lett. **291**, 101–109 (1998).

[9] J. Shao and N. Makri, "Forward-backward semiclassical dynamics with linear scaling.", J. Phys. Chem. A **103**, 9479–9486 (1999).

[10] N. Makri, "Forward-backward semiclassical and quantum trajectory methods for time correlation functions.", Phys. Chem. Chem. Phys. **13**, 14442–14452 (2011).

[11] K. Husimi, "Some Formal Properties of the Density Matrix", Proc. Physico-Mathematical Soc. Japan. 3rd Ser. **22**, 264–314 (1940).

[12] C. Y. Hsieh and R. Kapral, "Nonadiabatic dynamics in open quantum-classical systems: Forward-backward trajectory solution", J. Chem. Phys. **137**, 22A507 (2012).

[13] R. Kapral, "Quantum dynamics in open quantum-classical systems", J. Phys. Condens. Matter **27**, 073201 (2015).

[14]R. Lambert and N. Makri, "Quantum-classical path integral. I. Classical memory and weak quantum nonlocality", J. Chem. Phys. **137**, 22A552 (2012).

[15]R. Lambert and N. Makri, "Quantum-classical path integral. II. Numerical methodology", J. Chem. Phys. **137**, 22A553 (2012).

[16]T. Banerjee and N. Makri, "Quantum-classical path integral with self-consistent solvent-driven reference propagators", J. Phys. Chem. B **117**, 13357–13366 (2013).

[17]N. Makri, "Quantum-classical path integral: A rigorous approach to condensed phase dynamics", Int. J. Quantum Chem. **115**, 1209–1214 (2015).

[18]M. Ovchinnikov, V. A. Apkarian, and G. A. Voth, "Semiclassical molecular dynamics computation of spontaneous light emission in the condensed phase: Resonance Raman spectra", J. Chem. Phys. **114**, 7130–7143 (2001).

[19]N. Makri and W. H. Miller, "Coherent state semiclassical initial value representation for the Boltzmann operator in thermal correlation functions", J. Chem. Phys. **116**, 1–6 (2002).

[20]N. Makri, "Monte Carlo evaluation of forward-backward semiclassical correlation functions with a quantized coherent state density", J. Phys. Chem. B **106**, 8390–8398 (2002).

[21]A. Nakayama and N. Makri, "Forward-backward semiclassical dynamics for systems of indistinguishable particles", Chem. Phys. **304**, 147–158 (2004).

[22]Q. Shi and E. Geva, "Semiclassical Theory of Vibrational Energy Relaxation in the Condensed Phase", J. Phys. Chem. A **107**, 9059–9069 (2003).

[23]Y. Zhao and W. H. Miller, "Semiclassical initial value representation for the Boltzmann operator in thermal rate constants", J. Chem. Phys. **117**, 9605–9610 (2002).

[24]P. Frantsuzov, A. Neumaier, and V. A. Mandelshtam, "Gaussian resolutions for equilibrium density matrices", Chem. Phys. Lett. **381**, 117–122 (2003).

[25]P. A. Frantsuzov and V. A. Mandelshtam, "Quantum statistical mechanics with Gaussians: Equilibrium properties of van der Waals clusters", J. Chem. Phys. **121**, 9247–9256 (2004).

[26]E. J. Heller, "Time dependent variational approach to semiclassical dynamics", J. Chem. Phys. **64**, 63–73 (1976).

[27]J. Shao and E. Pollak, "A new time evolving Gaussian series representation of the imaginary time propagator", J. Chem. Phys. **125**, 133502 (2006).

[28]Q. Shi and E. Geva, "Vibrational Energy Relaxation in Liquid Oxygen from a Semiclassical Molecular Dynamics Simulation", J. Phys. Chem. A **107**, 9070–9078 (2003).

[29]A. Nakayama and N. Makri, "Simulation of dynamical properties of normal and superfluid helium", Proc. Natl. Acad. Sci. **102**, 4230–4234 (2005).

[30]J. Liu and W. H. Miller, "Using the thermal Gaussian approximation for the Boltzmann operator in semiclassical initial value time correlation functions", J. Chem. Phys. **125**, 224104 (2006).

[31] J. Liu and W. H. Miller, "Linearized semiclassical initial value time correlation functions using the thermal Gaussian approximation: Applications to condensed phase systems", J. Chem. Phys. **127**, 114506 (2007).

[32] N. Metropolis, A. W. Rosenbluth, M. N. Rosenbluth, A. H. Teller, and E. Teller, "Equation of State Calculations by Fast Computing Machines", J. Chem. Phys. **21**, 1087–1092 (1953).

[33] P. Ehrenfest, "XLVIII. Adiabatic invariants and the theory of quanta", Philos. Mag. Ser. 6 **33**, 500–513 (1917).

[34] R. T. Skodje, F. Borondo, and W. P. Reinhardt, "The semiclassical quantization of nonseparable systems using the method of adiabatic switching", J. Chem. Phys. **82**, 4611 (1985).

[35] M. V. Berry, "Semi-classical mechanics in phase space: a study of Wigner's function", Philos. Trans. R. Soc. London. Ser. A, Math. Phys. Sci. **287**, 237–271 (1977).

[36] N. Wright and N. Makri, "Phase space features and statistical aspects of forward-backward semiclassical dynamics", J. Phys. Chem. B **108**, 6816–6825 (2004).

[37] J. Liu, A. Nakayama, and N. Makri, "Long-time behaviour of quantized distributions in forward-backward semiclassical dynamics", Mol. Phys. **104**, 1267–1274 (2006).

[38] A. Caldeira and A. Leggett, "Path integral approach to quantum Brownian motion", Phys. A Stat. Mech. its Appl. **121**, 587–616 (1983).

[39] N. Makri, "The Linear Response Approximation and Its Lowest Order Corrections: An Influence Functional Approach", J. Phys. Chem. B **103**, 2823–2829 (1999).

[40] R. T. Skodje and J. R. Cary, "An analysis of the adiabatic switching method: Foundations and applications", Comput. Phys. Reports **8**, 221–292 (1988).

[41] J. Zakrzewski, S. Saini, and H. S. Taylor, "Semiclassical quantization via adiabatic switching. I. Choice of tori and initial conditions for two-dimensional systems", Phys. Rev. A **38**, 3877–3899 (1988).

[42] S. Saini, J. Zakrzewski, and H. S. Taylor, "Semiclassical quantization via adiabatic switching. II. Choice of tori and initial conditions for multidimensional systems", Phys. Rev. A **38**, 3900–3908 (1988).

[43] B. R. Johnson, "Semiclassical vibrational eigenvalues of H_3^+, D_3^+, and T_3^+ by the adiabatic switching method", J. Chem. Phys. **86**, 1445–1450 (1987).

[44] Q. Sun, J. M. Bowman, and B. Gazdy, "Application of adiabatic switching to vibrational energies of three-dimensional HCO, H_2O, and H_2CO", J. Chem. Phys. **89**, 3124–3130 (1988).

[45] B. R. Johnson, "Semiclassical vibrational eigenvalues of H_2O and SO_2 by the adiabatic switching method", Comput. Phys. Commun. **51**, 1–10 (1988).

[46] H. Romanowski, J. M. Bowman, and L. B. Harding, "Vibrational energy levels of formaldehyde", J. Chem. Phys. **82**, 4155–4165 (1985).

[47] G. Czakó and J. M. Bowman, "Reaction Dynamics of Methane with F, O, Cl, and Br on ab Initio Potential Energy Surfaces", J. Phys. Chem. A **118**, 2839–2864 (2014).

[48] A. Voros, "Wentzel-Kramers-Brillouin method in the Bargmann representation", Phys. Rev. A **40**, 6814–6825 (1989).

[49] M. Thoss, H. Wang, and W. H. Miller, "Generalized forward-backward initial value representation for the calculation of correlation functions in complex systems", J. Chem. Phys. **114**, 9220–9235 (2001).

[50] E. Jezek and N. Makri, "Finite Temperature Correlation Functions via Forward–Backward Semiclassical Dynamics", J. Phys. Chem. A **105**, 2851–2857 (2001).

Part II

Path integral methods for system-solvent problems

Chapter 6

Non-equilibrium reactive flux

6.1 Introduction

This chapter is based on the paper, A. Bose and N. Makri, "Non-equilibrium reactive flux: A unified framework for slow and fast reaction kinetics", J. Chem. Phys. **147**, 152723 (2017).

Reactive processes, such as charge transfer and barrier crossing, often occur on time scales that are much longer than those associated with the ro-vibrational dynamics of the reactants. Rather than following the slow transformation of reactants to products it is advantageous in such cases to evaluate the reaction rate constant using the flux formalism.[2–13] The latter is based on equilibrium correlation functions that involve the reactive flux, and classical, quantum mechanical, as well as semiclassical formulations are available. The main advantage of the flux correlation function formalism is that it requires the dynamics to be followed only up to the "plateau time", i.e., the time required for initial transients to settle and the reactant population to enter its slow, exponential decay.

There are, of course, many cases of fast reactions characterized by low potential barriers, where there is no clear separation of time scales. In such situations no plateau regime can be identified, thus the flux correlation function formalism cannot be used to obtain the reaction rate. In some cases of ultrafast reactions, transient dynamics persists almost until the reactant population attains its equilibrium value, causing strongly nonexponential kinetics for the duration of the reaction. These situations require full simulation of the population dynamics. Since one does not know *a priori* the applicability of the rate picture, one would typically attempt to infer the rate by evaluating the flux correlation function. In the event this function does not appear to plateau, one would abandon this approach and proceed to simulate the evolution of the reactant population.

Further, fully quantum mechanical calculations of condensed phase reactions are impractical, and one has to resort to approximate methods. Quantum-classical approaches are particularly attractive, because classical mechanics usually captures the dynamics of the quantum system's environment with satisfactory accuracy, while offering linear scaling. Several intuitive and efficient quantum-classical approximations are available for simulating state populations. However, equilibrium correlation functions require the evaluation of the Boltzmann operator for all interacting degrees of freedom. Evaluation of this operator in a mixed quantum-classical representation presents a major challenge, making quantum-classical methods not directly suitable to this task.

In this chapter, we propose a non-equilibrium, factorized reactant density formulation of the reactive flux, which addresses both of the above issues. By removing the need for evaluating the Boltzmann density of the total Hamil-

tonian, this formulation is easily amenable to quantum-classical treatments. In addition, the non-equilibrium flux formulation directly yields the early-time transient dynamics and (when relevant) the rate coefficient associated with long-time exponential decay. This allows for a characterization of slow or fast reaction kinetics from a single calculation. We emphasize that the non-equilibrium flux expression is not an approximation, and that, if evaluated exactly, it yields the same reaction rate as the conventional equilibrium reactive flux formalism.

Section 6.2 describes the non-equilibrium reactive flux and its relation to population dynamics. The characteristics of the non-equilibrium flux are illustrated through model calculations in Section 6.3.

6.2 Reactive flux with non-equilibrium initial conditions

We denote the reactant and product states collectively as $|\mathrm{R}\rangle$ and $|\mathrm{P}\rangle$ respectively. Miller has shown that the (forward) rate constant for reactive processes in gas phase bimolecular collisions is given by the expression

$$k_f = \mathrm{Z_R^{-1}} \lim_{t\to\infty} \mathrm{Tr}\left(\hat{\mathrm{F}}\, e^{i\hat{\mathrm{H}}t/\hbar}\, e^{-\beta\hat{\mathrm{H}}/2}\, \hat{h}_\mathrm{R}\, e^{-\beta\hat{\mathrm{H}}/2}\, e^{-i\hat{\mathrm{H}}t/\hbar}\right) \tag{6.2.1}$$

where $\beta = 1/k_\mathrm{B}\mathrm{T}$ is the inverse temperature, $\mathrm{Z_R}$ is the partition function of the reactants, $\hat{h}_\mathrm{R} = |\mathrm{R}\rangle\langle\mathrm{R}|$ is an operator that projects onto reactants, and $\hat{\mathrm{F}}$ is the symmetrized flux operator,

$$\hat{\mathrm{F}} = \frac{i}{\hbar}\left[\hat{\mathrm{H}}, \hat{h}_\mathrm{R}\right]. \tag{6.2.2}$$

The dividing surface that separates reactants from products is perpendicular to the reaction coordinate, which defines the "system" with Hamiltonian $\hat{\mathrm{H}}_\mathrm{sys}$, while the remaining degrees of freedom constitute the "environment", defined by $\hat{\mathrm{H}}_\mathrm{env} = \hat{\mathrm{H}} - \hat{\mathrm{H}}_\mathrm{sys} - \hat{\mathrm{V}}_\mathrm{int}$.

For typical barrier crossing processes in the condensed phase, where the reactant-product complex is characterized by a double well potential (or by two bound diabatic surfaces, as in electron transfer reactions), Equation 6.2.1 must be modified to

$$k_f = \mathrm{Z_R^{-1}}\ \mathrm{Tr}\left(\hat{\mathrm{F}}\, e^{i\hat{\mathrm{H}}t/\hbar}\, e^{-\beta\hat{\mathrm{H}}/2}\, \hat{h}_\mathrm{R}\, e^{-\beta\hat{\mathrm{H}}/2}\, e^{-i\hat{\mathrm{H}}t/\hbar}\right)\Big|_{t\approx t_{plateau}} \tag{6.2.3}$$

where t_plateau is the "plateau time", when the initial transients have died out and the reactant population has just entered the slow, exponential decay. Further, Equation 6.2.3 is valid under the assumption that all non-reactive intra-well processes occur on a time scale much shorter than the time scale for completion of the reaction. This is often the case, as typical potential barriers separating reactants and products are significantly larger than the thermal energy. Under these conditions, the plateau time occurs relatively early, such that $k_f t_\mathrm{plateau} \ll 1$. On a longer time scale, the function inside the trace of Equation 6.2.3 is not constant but decays exponentially.

Rearranging the trace and exploiting the Hermitian character of the flux operator, Equation 6.2.3 can also be

written in the form

$$k_f = -\mathrm{F}_{\mathrm{eq}}\left(t_{\mathrm{plateau}}\right), \tag{6.2.4}$$

where

$$\mathrm{F}_{\mathrm{eq}}(t) = \mathrm{Z}_{\mathrm{R}}^{-1}\ \mathrm{Tr}\left(e^{i\hat{\mathrm{H}}t/\hbar}\, e^{-\beta\hat{\mathrm{H}}/2}\, \hat{h}_{\mathrm{R}}\, e^{-\beta\hat{\mathrm{H}}/2}\, e^{-i\hat{\mathrm{H}}t/\hbar}\, \hat{\mathrm{F}}\right)\Big|_{t\approx t_{plateau}} \tag{6.2.5}$$

Assuming that the coupling $\mathrm{V}_{\mathrm{int}}$ between the system and the environment is diagonal in position, the flux operator acts within the space of the system. Then Equation 6.2.5 can be rewritten in the form

$$\mathrm{F}_{\mathrm{eq}}(t) = -\,\mathrm{Tr}_{\mathrm{sys}}\left(\hat{\rho}_{\mathrm{eq}}^{\mathrm{red}}(t)\hat{\mathrm{F}}\right) \tag{6.2.6}$$

where $\hat{\rho}_{\mathrm{eq}}(t)$ is the reduced density operator of the quantum system,

$$\hat{\rho}_{\mathrm{eq}}^{\mathrm{red}}(t) = \mathrm{Tr}_{\mathrm{env}}\left(e^{-i\hat{\mathrm{H}}t/\hbar}\hat{\rho}_{\mathrm{eq}}(0)e^{i\hat{\mathrm{H}}t/\hbar}\right), \tag{6.2.7}$$

and the initial condition of the density is

$$\hat{\rho}_{\mathrm{eq}}(0) = \mathrm{Z}_{\mathrm{R}}^{-1}e^{-\beta\hat{\mathrm{H}}/2}\hat{h}_{\mathrm{R}}e^{-\beta\hat{\mathrm{H}}/2}. \tag{6.2.8}$$

According to Equation 6.2.6, the reaction rate is given by the (negative of) the expectation value of the flux operator in the plateau regime, with the initial density given by Equation 6.2.8.

Invoking Onsager's ideas, we argue that (after the initial transients have settled) the decay of the expectation value of the flux should approach its thermodynamic limit with the same rate, regardless of the intiial condition. This invariance has been used to show the equivalence of several commony used rate expressions that involve different symmetrizations of the Boltzmann-transformed flux. In this work, we consider replacing Equation 6.2.8 by a simpler factorized initial condition, which is physically meaningful and easier to evaluate. In particular, a factorized initial condition would allow a fully quantum mechanical treatment of the reaction coordinate and a classical (or quasiclassical) treatment of the environment by means of trajectories sampled from a phase-space distribution. The particular form we choose is designed to mimic the early state of the reactive process of interest. We choose a factorized initial condition that describes the isolated reactants,

$$\hat{\rho}_{\text{non-eq}}(0) = \hat{h}_{\mathrm{R}} \otimes \frac{e^{-\beta\hat{\mathrm{H}}_{\mathrm{env}}^{\mathrm{init}}}}{\mathrm{Z}_{\mathrm{env}}^{\mathrm{init}}}, \tag{6.2.9}$$

where $\hat{\mathrm{H}}_{\mathrm{env}}^{\mathrm{init}}$ is the Hamiltonian for the degrees of freedom of the environment in (exact or approximate) equilibrium with the system in the reactant state and $\mathrm{Z}_{\mathrm{env}}^{\mathrm{init}}$ is its partition function. In the particular case of an electron transfer reaction, $\hat{\mathrm{H}}_{\mathrm{env}}^{\mathrm{init}}$ is the Hamiltonian for the solvent equilibrated with respect to the quantum state describing the elec-

tron donor, thus the factorized density of Equation 6.2.9 describes the reactant state exactly in this case. We define the expectation value of the flux, subject to this new, non-equilibrium initial density,

$$\begin{aligned} \mathrm{F}_{\text{non-eq}}(t) &= -\operatorname{Tr}_{\text{sys}}\left(e^{-i\hat{\mathrm{H}}t/\hbar}\hat{\rho}^{\text{red}}_{\text{non-eq}}(0)e^{i\hat{\mathrm{H}}t/\hbar}\hat{\mathrm{F}}\right) \\ &= -\operatorname{Tr}_{\text{sys}}\left(\hat{\rho}^{\text{red}}_{\text{non-eq}}(t)\hat{\mathrm{F}}\right) \end{aligned} \tag{6.2.10}$$

It is easy to see that

$$\begin{aligned} \mathrm{F}_{\text{non-eq}}(t) &= \frac{i}{\hbar}\operatorname{Tr}\left(e^{-i\hat{\mathrm{H}}t/\hbar}\hat{\rho}_{\text{non-eq}}(0)e^{i\hat{\mathrm{H}}t/\hbar}\left[\hat{\mathrm{H}},\hat{h}_{\mathrm{R}}\right]\right) \\ &= \frac{\mathrm{d}}{\mathrm{d}t}\rho_{\mathrm{RR}}(t), \end{aligned} \tag{6.2.11}$$

where

$$\rho_{\mathrm{RR}}(t) = \langle \mathrm{R}|\hat{\rho}^{\text{red}}_{\text{non-eq}}(t)|\mathrm{R}\rangle \tag{6.2.12}$$

is the popualtion of the reactants with initial value equal to one, according to Equation 6.2.9. Thus $\mathrm{F}_{\text{non-eq}}(t)$ is equal to the time derivative of the reactant population at all times. Once the transients die out, the reactive process enters the exponential decay regime, where the reactant population decays according to the form

$$\rho_{\mathrm{RR}}(t) - \rho_{\mathrm{RR}}(\infty) = \left(\rho_{\mathrm{RR}}\left(t_{\text{exp}}\right) - \rho_{\mathrm{RR}}(\infty)\right)e^{-\left(k_f+k_b\right)\left(t-t_{\text{exp}}\right)}, \tag{6.2.13}$$

where t_{exp} indicates the onset of the exponential regime in the population dynamics and k_f and k_b are the forward and backward rates. The time derivative of the reactant population is

$$\frac{\mathrm{d}}{\mathrm{d}t}\rho_{\mathrm{RR}}(t) = -\left(k_f+k_b\right)\left(\rho_{\mathrm{RR}}\left(t_{\text{exp}}\right) - \rho_{\mathrm{RR}}(\infty)\right)e^{-\left(k_f+k_b\right)\left(t-t_{\text{exp}}\right)}. \tag{6.2.14}$$

The time t_{exp} may be longer than the plateau time. However, as long as there is a separation of time scales, it is much shorter than $\left(k_f+k_b\right)^{-1}$, thus Equation 6.2.14 will plateau. At the onset of the plateau regime, the reactant population has not yet changed from its initial value, thus $\rho_{\mathrm{RR}}\left(t_{\text{plateau}}\right) \approx 1$. It follows that

$$\mathrm{F}_{\text{non-eq}}(t_{\text{exp}}) = \left.\frac{\mathrm{d}}{\mathrm{d}t}\rho_{\mathrm{RR}}(t)\right|_{t=t_{\text{exp}}} = -\left(k_f+k_b\right)\left(1-\rho_{\mathrm{RR}}(\infty)\right) = -k_f \tag{6.2.15}$$

where the last equality is a consequence of the detailed balance condition. Thus, if there is a separation of time scales, the expectation value of the flux with the non-equilibrium initial condition corresponding to the reactant density will plateau to the negative of the forward reaction rate constant. Thus, in line with the discussion of Craig et al.,[14] the equilibrium and the non-equilibrium flux expressions have the same plateau value (and subsequent decay), although they are expected to differ at earlier times. The ability to use a factorized thermal density without affecting

the accuracy of the computed rate value is particularly useful in simulations employing quantum-classical methods.

Most importantly, the non-equilibrium flux expression with a factorized reactant density is particularly useful in the case of electron transfer reactions, where Equation 6.2.9 provides an exact description of the reactive species at the onset of the chemical process. Even when the lack of a clear separation of time scales causes a late onset of the exponential regime, i.e., the absence of a plateau and/or nonexponential kinetics, the non-equilibrium flux can still be employed to infer the evolving reactant population,

$$\rho_{\mathrm{RR}}(t) = 1 + \int_0^t \mathrm{F}_{\text{non-eq}}\left(t'\right) dt'. \tag{6.2.16}$$

If the transient dynamics survive long enough for the reactant population to drop substantially from its initial value, Equation 6.2.16 captures this early nonexponential dynamics faithfully, while the rate constant obtained from Equation 6.2.15 (along with the backward rate, which is available through the detailed balance condition) can be used to infer the subsequent population decay through an exponential function, i.e.,

$$\rho_{\mathrm{RR}}(t) = \begin{cases} 1 + \displaystyle\int_0^t \mathrm{F}_{\text{non-eq}}\left(t'\right) dt' & t < t_{\mathrm{exp}} \\ \rho_{\mathrm{RR}}(\infty) + \left(\rho_{\mathrm{RR}}\left(t_{\mathrm{exp}}\right) - \rho_{\mathrm{RR}}(\infty)\right) e^{-\left(k_f + k_b\right)\left(t - t_{\mathrm{exp}}\right)} & t > t_{\mathrm{exp}} \end{cases} \tag{6.2.17}$$

Given the intimate connection between the nonequilibrium flux and the population dynamics, an obvious question is whether one could obtain the same information by computing the population and evaluating its time derivative numerically. The main problem with that approach is that it can be unstable, as numerical derivatives are very sensitive to statistical noise. Since most simulation methods applicable to molecular/condensed phase systems employ Monte Carlo sampling,[15] it is preferable to differentiate the population expression analytically. By contrast, the integration procedure required for inferring the population from the non-equilibrium flux is stable. In fact integration tends to wipe out the effects of random noise that may be present in the derivative function.

As mentioned earlier, one of the difficulties associated with numerical evaluation of the equilibrium flux expressions is often the need to evaluate the Boltzmann operator in the appropriate representation. For example, if a mixed quantum-classical approximation to the time evolution is adopted, one needs to obtain the Wigner quantized phase space distribution[16] for the environment degrees of freedom in equilibrium with the quantum mechanical reaction coordinate. In the case of molecular systems with a well-defined harmonic zeroth order Hamiltonian, we have shown that the Wigner function can be obtained approximately from adiabatically switched trajectories.[17] However, accounting for the interaction between classical and quantum degrees of freedom presents a challenge. On the other hand, the use of a non-equilibrium flux expression with a factorized reactant density is easily amenable to a variety of numerical treatments and is ideally suited to quantum-classical methods. Even when the factorized form is only an approximation of the true reactant density, the procedure yields the exact rate. Additionally, when the density factorization is exact, as in the case of the electron transfer, integration of the non-equilibrium flux yields the early

population dynamics, which is crucial for a correct characterization of the reaction prior to the onset of exponential kinetics and when a plateau cannot be identified.

6.3 Numerical examples

We illustrate the ideas presented in Section 6.2 with several numerical examples on model symmetric two-level systems (TLSs) coupled to harmonic dissipative environments. The TLS Hamiltonian is given by

$$\hat{\mathrm{H}}_{\mathrm{sys}} = -\hbar\Omega \left(|\mathrm{R}\rangle\langle \mathrm{P}| + |\mathrm{P}\rangle\langle \mathrm{R}| \right), \tag{6.3.1}$$

while the harmonic bath and the system bath interaction have the usual form,

$$\hat{\mathrm{H}}_{\mathrm{env}} = \sum_j \frac{\hat{p}_j^2}{2m_j} + \frac{1}{2} m_j \omega_j^2 \hat{q}_j^2 \tag{6.3.2}$$

$$\hat{\mathrm{V}}_{\mathrm{int}} = -\sum_j c_j \hat{q}_j \left(|\mathrm{R}\rangle\langle \mathrm{R}| - |\mathrm{P}\rangle\langle \mathrm{P}| \right). \tag{6.3.3}$$

The bath is described by an Ohmic spectral density,[18]

$$\mathrm{J}(\omega) = \frac{\pi}{2} \xi \hbar \omega \exp\left(-\frac{\omega}{\omega_c} \right), \tag{6.3.4}$$

where ξ is the Kondo parameter and ω_c is the "cutoff" frequency, which corresponds to the maximum of Equation 6.3.4. The equilibrium flux was evaluated using the quasi-adiabatic propagator path integral[19] (QuAPI) methodology of complex-time flux correlation functions.[20,21] The non-equilibrium flux with a factorized initial condition was obtained by propagating the reduced density matrix using the iterative decomposition of the QuAPI expression.[22–24] The factorized initial condition is an exact description of the reactant species in the case of a TLS.

The parameters of the first example are chosen from earlier work,[25] where the TLS coupling corresponds to a tunneling splitting of $2\hbar\Omega = 0.001\,05\ \mathrm{cm}^{-1}$ and the bath cutoff frequency has the value $500\ \mathrm{cm}^{-1}$. These parameters are characteristics of many proton transfer or isomerization reactions, where a relatively high potential barrier leads to a small tunneling splitting, while the vibrational frequencies of the environment are much higher. Thus, there is a clear separation of time scales and one expects a well-defined flux plateau.

The equilibrium and non-equilibrium flux functions are compared in Figure 6.1. It is seen that both functions plateau in a fairly short time (of the order of the characteristic time scale ω_c^{-1} of the environment degrees of freedom). While the equilibrium flux appears to plateau somewhat earlier, as expected (given the equilibrium initial condition), the flux with a factorized reactant density does not take much longer to reach its plateau. The short-time behavior of the non-equilibrium flux differs somewhat, reflecting the true transient dynamics of the reactant population, and the difference between the two forms increases with the system-bath coupling strength. We also report the rates of this system at various temperatures and system-bath coupling strengths in Figure 6.2. The rate constants obtained

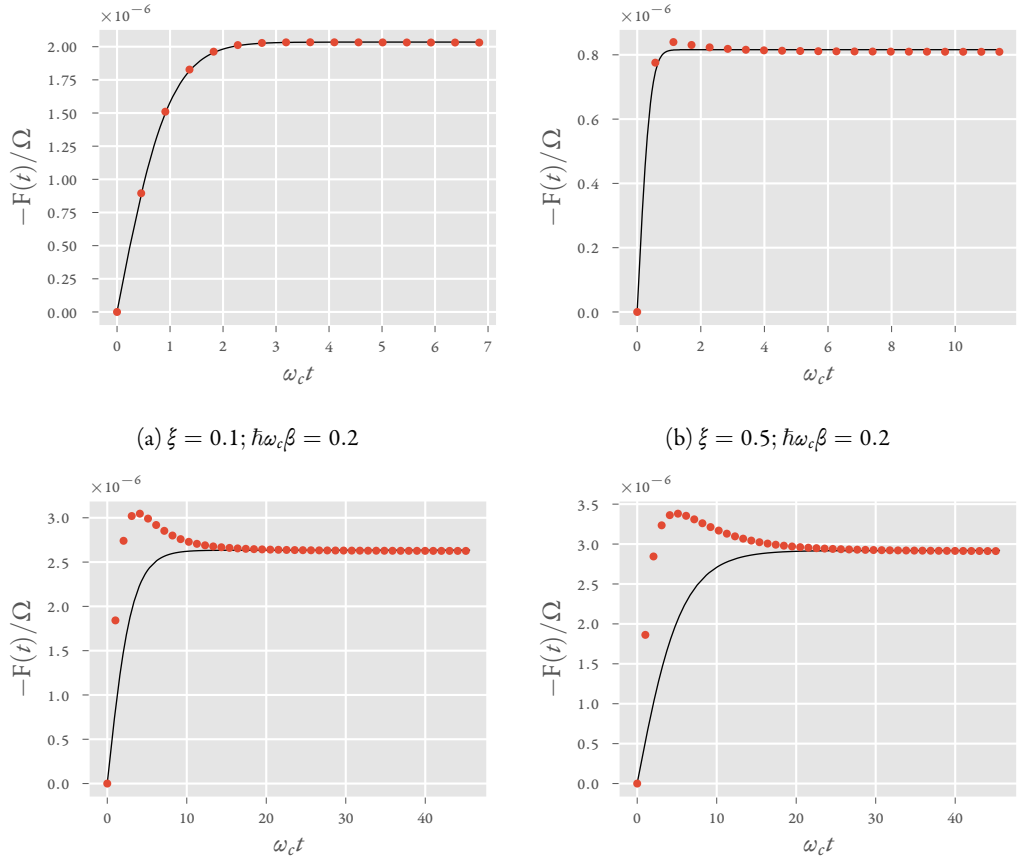

(a) $\xi = 0.1; \hbar\omega_c\beta = 0.2$

(b) $\xi = 0.5; \hbar\omega_c\beta = 0.2$

(c) $\xi = 0.5; \hbar\omega_c\beta = 5$

(d) $\xi = 0.5; \hbar\omega_c\beta = 10$

Figure 6.1: Comparison of the equilibrium and non-equilibrium flux functions Equation 6.2.5 and Equation 6.2.10, for the first dissipative TLS described in Section 6.3. The solid line shows the (negative of the) function with the equilibrium initial condition, while the red markers show the (negative of the) flux with the initial condition given by the reactant density.

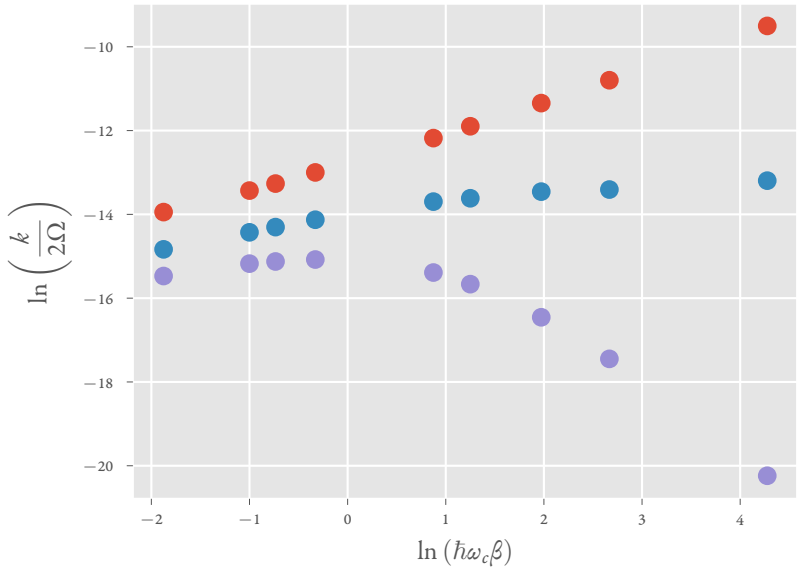

Figure 6.2: Consolidated rates using non-equilibrium flux. Red markers: $\xi = 0.1$, blue markers: $\xi = 0.5$, violet markers: $\xi = 1.5$.

from the plateau values of both flux functions agree with the results of Topaler and Makri.[25]

The second model employs parameters encountered in some utrafast condensed phase electron transfer reactions. Here the parameters are $\omega_c = 2.5\Omega$, $\hbar\omega_c\beta = 0.5$ and $\xi = 1.2$. Figure 6.3 shows the non-equilibrium flux as a function of time, along with its time integral, which is seen to be in excellent agreement with the reactant population obtained through the direct propagation of the reduced density matrix. The proximity of TLS and bath time scales leads to rapid population decay. Figure 6.3(a) shows that the flux reaches a large negative value around $\omega_c t \approx 1$. This region corresponds to an inflection point of the population, which shortly thereafter settles into an exponential decay with a constant rate. However since the duration of the transient dynamics is not negligible compared to the population decay time, the flux enters its exponential decay regime on the same time scale and thus does not display a plateau.

As a third example, we discuss the quantum-classical path integral[26–28] (QCPI) all-atom simulation of the ferrocene-ferrocenium self-exchange electron transfer reaction in liquid hexane.[29] This is an ultrafast reaction that completes in a few picoseconds. In this case, the non-exponential transient dynamics persist until the reaction is nearly complete, leading to much faster decay that the rate constant associated with the long-time exponential regime would seem to predict.

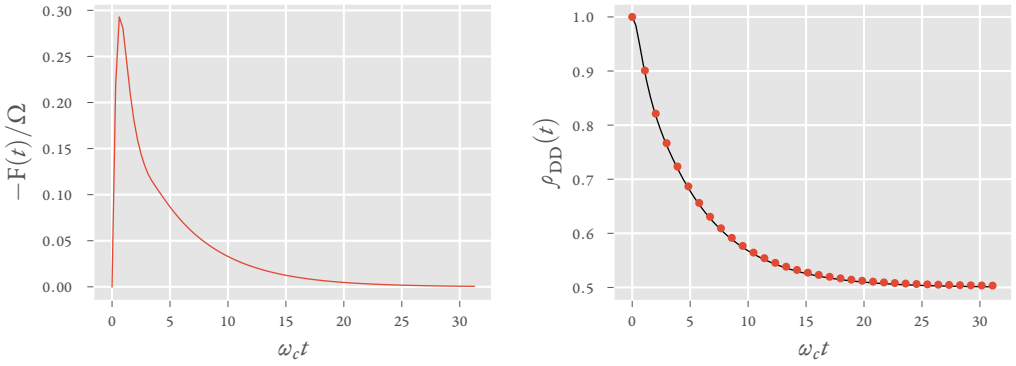

(a) Non-equilibrium flux as a function of time

(b) Dynamics of the population of reactant state

Figure 6.3: Non-equilibrium flux and population dynamics for the second dissipative TLS described in Section 6.3. Black line: time integral of the non-equilibrium flux function. Red markers: evolution of the initial populated state computed through propagation of the density matrix.

6.4 Discussion and concluding remarks

One of the flux formulations of reaction dynamics expresses the rate as the cross correlation function of a projector and the flux operator, or equivalently as the expectation value of the reactive flux with respect to a symmetrically "Boltzmannized" operator. These expressions involve the Boltzmann operator with respect to all degrees of freedom, whose computation often presents challenges, in particular if mixed quantum-classical methods are to be employed. To remove this obstacle, one would like to replace the Boltzmann operator by a factorized form, such that the quantum system and its environment may be treated at different levels of approximation. However, such a modification naturally leads to a different function.

Since a change of initial conditions does not affect the rate of approach to equilibrium, one may replace the Boltzmann operator by a non-equiibrium form without affecting the plateau value of the flux. As long as the real time dynamics is evaluated in a numerically exact manner, the non-equilibrium flux expression yields the *exact* value of the rate constant, irrespective of any approximations made to the initial thermal density. This feature offers considerable flexibility, allowing convenient approximations of the Boltzmann density without sacrificing accuracy in the computed value of the reaction rate. This flexibility is particularly valuable in simulations employing quantum-classical methods.

In particular, if the reactant density involves a single quantum state, as in the case of electron transfer reactions, the factorized initial condition describes the true initial state of the reactant species and the flux expression gives precisely the time derivative of the reactant population. Thus, in addition to its convenient factorized initial density, this flux expression yields the short-time transient dynamics and through its plateau value the rate of exponential decay, allowing characterization of slow or ultrafast reaction in a unified framework. The examples presented in Section 6.3 illustrate different types of ultrafast dynamics where determination of the rate through the equilibrium

flux may not be possible or where such a rate may not even be meaningful. The former happens when despite the population following exponential decay for the greater part, the flux does not plateau, and the latter is a common occurrence when the non-exponential population decay happens within a time that is shorter than the inverse of the long-time rate.

As expected, the non-equilibrium flux exhibits more pronounced transients and may settle to its plateau value somewhat slower compared to the equilibrium flux. However, the examples presented in Section 6.3 show that the plateau time is still reached quite rapidly. This is to be expected even in the case of very slow processes, since the plateau time of the non-equilibrium flux coincides with the onset of the exponential population decay, which occurs very early (on the time scale of intra-well dynamics) compared to the time for completion of the reaction. Thus, the use of the non-equilibrium flux expression does not require simulation of dynamics for very long times.

The non-equilibrium formulation of the reactive flux will facilitate simulations of fast and slow reactions in solution or biological systems. A particularly attractive possibility is its evaluation using rigorous QCPI methodology,[26,27] which treates the interaction between the quantum system and its classical environment in full detail and without approximation. Applications to charge transfer reactions are in progress.

Chapter 7

Near equilibrium initial condition for rate calculations using QCPI

7.1 Introduction

Chemical reactions in condensed phase polar environments can often be very sluggish with extremely long non-Markovian memories. Hence, following a reaction through to completion with methods for exact quantum dynamics may well be infeasible. Rate theory provides a very convenient alternative for cases when the dynamics is well represented by a exponential decay, reducing the cost of the computation by orders of magnitude. Various approximate and perturbative methods for calculating rates have been proposed, including the famous Marcus theory for the rate of electron transfer.[30,31] Expressions for exact quantum rates using thermal equilibrium flux correlation functions exist which do not suffer from the problems of transition state theories and perturbative approximations.[7,8]

Calculating the flux correlation function using exact quantum dynamics for atomistic reactions is challenging. Such reactions are generally treated under the mixed quantum-classical framework of methods, where the low dimensional reaction coordinates constitute a fully quantum mechanical system, and the remaining dimensions are relegated to a classical solvent. This leads to an interesting problem — any thermal correlation function requires estimation of a Boltzmannized operator, so we need to simultaneously equilibrate the quantum system with a quasi-classical solvent. In the previous chapter, we have shown that this is not strictly necessary for a rate calculation as it is independent of the initial condition. Various approximations to the initial density have been provided.[32,33] We also observe that simulation times required to reach the plateau of the flux function increases as the initial condition gets farther from the equilibrium. We have proposed a fully non-equilibrium initial condition that is solely determined by the physics of the system at hand in Chapter 6. This, of course, leads to longer simulation times, but also gives us valuable insights into the transients.

In this chapter, we explore another initial condition which approximates the coupled thermal equilibrium. A key feature in the methods which approximate the Boltzmannized initial condition[32,33] is that they ignore the system solvent coupling. This of course has the benefit of leading to very simple expressions, but it moves the initial condition further away from the equilibrium in cases where the system is strongly coupled with the solvent. In fact strong system-solvent couplings are the hallmark of slow condensed phase reactions where rate theory is most convenient because of substantial reduction of simulation times. Our non-equilibrium method, though compatible with QCPI, may prove to be less useful for such slow reactions. In Section 7.2, we derive a very simple expression for an approximate initial density that couples the system and the bath. We show numerical examples and comparisons with the non-

equilibrium method in Section 7.3.

7.2 Near equilibrium flux using QCPI

The QCPI formalism combines a fully quantum mechanical description of a low-dimensional "system" with a quasiclassical treatment of the system's multidimensional environment or solvent in a rigorous manner. Suppose $\hat{s}$ is the position operator of the system, and q, p constitute the phase-space coordinate of the solvent. Then the total Hamiltonian governing the dynamics has the form

$$\hat{\mathrm{H}} = \hat{\mathrm{H}}_0 + \hat{\mathrm{H}}_{\mathrm{env}}\left(q,p\right) + \hat{\mathrm{V}}_{\mathrm{int}}\left(\hat{s},q,p\right) \tag{7.2.1}$$

where

$$\hat{\mathrm{H}}_{\mathrm{env}} = \hat{\mathrm{T}}_{\mathrm{env}}\left(p\right) + \hat{\mathrm{V}}_{\mathrm{env}}\left(q\right) \tag{7.2.2}$$

The time-dependent reduced density matrix, under QCPI, is then given by

$$\rho_{\mathrm{red}}\left(s_{\mathrm{N}}^{\pm};\mathrm{N}\Delta t\right) = \int \mathrm{d}q_0\,\mathrm{d}p_0\,\mathrm{P}\left(q_0,p_0\right)\,\mathrm{Q}\left(q_0,p_0,s_{\mathrm{N}}^{\pm};\mathrm{N}\Delta t\right) \tag{7.2.3}$$

where P is the phase-space density of the solvent and Q contains all the dynamical effects arising from the system-solvent interaction, and is called the quantum influence function. It is calculated as a path sum over the system space

$$\begin{aligned}\mathrm{Q}\left(q_0,p_0,s_{\mathrm{N}}^{\pm};\mathrm{N}\Delta t\right) = \sum_{s_0^{\pm}}\sum_{s_1^{\pm}}\cdots\sum_{s_{\mathrm{N}-1}^{\pm}} &\left\langle s_{\mathrm{N}}^{+}\right|\hat{\mathrm{U}}_{\mathrm{ref}}\left(\mathrm{N}\Delta t,(\mathrm{N}-1)\Delta t;q_0,p_0\right)\left|s_{\mathrm{N\text{-}1}}^{+}\right\rangle\cdots\\ &\times\left\langle s_1^{+}\right|\hat{\mathrm{U}}_{\mathrm{ref}}\left(\Delta t,0;q_0,p_0\right)\left|s_0^{+}\right\rangle\rho_{\mathrm{red}}\left(s_0^{\pm};0\right)\left\langle s_0^{-}\right|\hat{\mathrm{U}}_{\mathrm{ref}}^{\dagger}\left(\Delta t,0;q_0,p_0\right)\left|s_1^{-}\right\rangle\cdots\\ &\times\left\langle s_{\mathrm{N}-1}^{-}\right|\hat{\mathrm{U}}_{\mathrm{ref}}^{\dagger}\left((\mathrm{N}-1)\Delta t,\mathrm{N}\Delta t;q_0,p_0\right)\left|s_{\mathrm{N}}^{-}\right\rangle\exp\left(\frac{i}{\hbar}\varphi\left(q_0,p_0,\left\{s_j^{\pm}\right\}\right)\right)\end{aligned} \tag{7.2.4}$$

where φ is the solvent backreaction on the system that appears as a path-dependent phase in QCPI and $\mathrm{U}_{\mathrm{ref}}$ is the solvent-driven reference propagator obtained by solving the Schrödinger equation for the system under the time-dependent reference Hamiltonian:

$$\hat{\mathrm{H}}_{\mathrm{ref}}\left(t;q_0,p_0\right) = \hat{\mathrm{H}}_0 + \hat{\mathrm{H}}_{\mathrm{env}}\left(s,q_{\mathrm{ref}}(t),p_{\mathrm{ref}}(t)\right) \tag{7.2.5}$$

$$\varphi\left(q_0,p_0,\left\{s_j^{\pm}\right\}\right) = \int \mathrm{d}t\left(\Delta\mathrm{V}_{\mathrm{int}}\left(q(t),p(t),\left\{s_j^{\pm}\right\}\right) - \Delta\mathrm{V}_{\mathrm{int}}\left(q_{\mathrm{ref}}(t),p_{\mathrm{ref}}(t),\left\{s_j^{\pm}\right\}\right)\right) \tag{7.2.6}$$

Here $q(t), p(t)$ define the trajectory of the solvent starting from an initial condition q_0, p_0 forced by the system path $\left\{s_j^{\pm}\right\}$. The reference trajectory, $q_{\mathrm{ref}}(t), p_{\mathrm{ref}}(t)$ starts from the same initial condition but is independent of the system path and subject only to "reference" forces that are given as ansatz of our choice. The method converges to

the correct answer irrespective of this choice, though certain choices can lead to easier convergence.

QCPI in the above formulation is perfect for applications where the initial condition is separable between the system and the solvent. If the system consists of two states, the reactant $|\mathrm{R}\rangle$ and the product $|\mathrm{P}\rangle$, and $\hat{h}_{\mathrm{R}} = |\mathrm{R}\rangle\langle\mathrm{R}|$, then the following represents the initial condition

$$\hat{\rho}(0) = \hat{h}_{\mathrm{R}} \otimes \frac{\exp\left(-\beta\hat{\mathrm{H}}_{\mathrm{env}}\right)}{\mathrm{Z}_{\mathrm{env}}} \tag{7.2.7}$$

where $\beta = \frac{1}{k_{\mathrm{B}}\mathrm{T}}$ is the inverse temperature. $\hat{h}_{\mathrm{R}}$ is projects onto the reactant surface. This separable initial condition is exact for electron transfer reactions where the system can be easily described by two states and the solvent is equilibrated to the reactant. QCPI has been successfully applied to studying the dynamics of an atomistic electron transfer reaction.[29]

For extremely slow reactions, it is not always computationally feasible to follow the dynamics of the reaction out to time scales where either the reaction is complete or the initial transients have died down and the exponential decay has set in. In such cases, the rate picture is more useful. Miller[7] has shown that the forward rate of a bimolecular reaction can be given in terms of a thermal correlation function[8]

$$k_f = \mathrm{Z}_{\mathrm{R}}^{-1} \lim_{t\to\infty} \mathrm{Tr}\left(\hat{\mathrm{F}} e^{i\hat{\mathrm{H}}t/\hbar} e^{-\beta\hat{\mathrm{H}}/2} \hat{h}_{\mathrm{R}} e^{-\beta\hat{\mathrm{H}}/2} e^{-i\hat{\mathrm{H}}t/\hbar}\right) \tag{7.2.8}$$

where Z_{R} is the reactant partition function and $\hat{\mathrm{F}}$ is the symmetrized flux operator defined by

$$\hat{\mathrm{F}} = \frac{i}{\hbar}\left[\hat{\mathrm{H}}, \hat{h}_{\mathrm{R}}\right] \tag{7.2.9}$$

The flux is defined with respect to a transition manifold normal to the reaction coordinate. The long time limit involved in Equation 7.2.8 proves to be computationally expensive, but is only relevant in gas phase reactions. It has been shown[20,25,34] that in the presence of a condensed phase environment, the rate equation gets modified to be the value at a "plateau" time. For harmonic baths, numerically exact equations for the resulting complex time correlation function can be obtained, and have been extensively studied.[20,25,34] However, such semi-analytic solutions are not possible for generic anharmonic environments, where quantum-classical propagation would be most useful.

To calculate the rate using Equation 7.2.8, a convenient representation of the simultaneously equilibrated system-solvent is required. In case of mixed quantum-classical methods, this amounts to a partial Wigner transform of the full Boltzmann operator in the space of the solvent degrees of freedom, while keeping the system in configuration space. Exact expressions for the case of spin-boson, utilizing Gaussian integrals have recently been calculated.[35] However, there can be no semi-closed form expression for the most general case of anharmonic solvents. We have recently described a simple method for approximating the Wigner density for a general Hamiltonian using classical trajectories,[17] and tested it successfully on multidimensional anharmonic Hamiltonians. However due to the difference between a discrete system and a continuous solvent, it is not a viable method for generating the coupled distribution.

We recall here the idea that the long time rate is independent of the initial condition chosen. The further the

initial condition is from equilibrium, the longer it takes for the flux correlation function to plateau, but it still rigorously gives the correct rate. This independence has been very successfully exploited[14,32,33] to come up with various initial conditions which make the flux methods amenable to mixed quantum-classical dynamics. We have already discussed a fully non-equilibrium initial condition[1] in Chapter 6. This has the added advantage of also giving the correct transients. We have tested the non-equilibrium flux method with QCPI to get the correct rates for various systems. In this chapter, however, we propose a different initial condition similar in spirit to the various separable initial conditions previously discussed, which captures much more of the system-solvent coupling while remaining amenable to quantum classical treatment. We also show that there is a significant decrease in the transient effects and speedup of the plateau time compared to the non-equilibrium version showing that we are approximating the full Boltzmann operator pretty well.

First we observe that the system-solvent entanglement cannot be ignored if the initial density needs to be close to the true Boltzmann operator. Let us start by deriving a path integral representation for the partial Wigner transform of the density operator over the solvent degrees of freedom.

$$\mathrm{W}\left(s_0^{\pm},q,p\right)=(2\pi\hbar)^{-\frac{1}{2}}\int_{-\infty}^{\infty}\mathrm{d}\xi\,\left\langle s_0^{+},q+\frac{\xi}{2}\middle|\exp\left(-\beta\hat{\mathrm{H}}\right)\middle|s_0^{-},q-\frac{\xi}{2}\right\rangle\exp\left(-i\frac{p\xi}{\hbar}\right) \tag{7.2.10}$$

To get the path integral representation, split the Boltzmann operator into N imaginary time slices such that $\tau=\frac{\beta}{\mathrm{N}}$. By subsequent application of the Trotter formula for small τ, we get

$$\exp\left(-\beta\hat{\mathrm{H}}\right)=\left(\exp\left(-\frac{\tau}{2}\hat{\mathrm{H}}_{\mathrm{env}}\right)\exp\left(-\tau\hat{\mathrm{H}}_{\mathrm{sys}}\right)\exp\left(-\frac{\tau}{2}\hat{\mathrm{H}}_{\mathrm{env}}\right)\right)^{\mathrm{N}} \tag{7.2.11}$$

and further as

$$\left(\exp\left(-\frac{\tau}{2}\hat{\mathrm{H}}_{\mathrm{env}}\right)\exp\left(-\tau\hat{\mathrm{H}}_{\mathrm{sys}}\right)\exp\left(-\frac{\tau}{2}\hat{\mathrm{H}}_{\mathrm{env}}\right)\right)^{\mathrm{N}}=\left(e^{-\frac{\tau}{2}\hat{\mathrm{T}}}e^{-\frac{\tau}{2}\hat{\mathrm{V}}_{\mathrm{tot}}}e^{-\tau\hat{\mathrm{H}}_{\mathrm{sys}}}e^{-\frac{\tau}{2}\hat{\mathrm{V}}_{\mathrm{tot}}}e^{-\frac{\tau}{2}\hat{\mathrm{T}}}\right)^{\mathrm{N}} \tag{7.2.12}$$

where $\hat{\mathrm{V}}_{\mathrm{tot}}=\hat{\mathrm{V}}+\hat{\mathrm{V}}_{\mathrm{int}}$.

Now, the path integral expression for $\mathrm{W}\left(s_0^{\pm},q,p\right)$ is given by

$$\begin{aligned}\mathrm{W}\left(s_0^{\pm},q,p\right)=(2\pi\hbar)^{-\frac{1}{2}}\int_{-\infty}^{\infty}\mathrm{d}\xi\sum_{s_1}\cdots\sum_{s_{\mathrm{N}-1}}\int_{-\infty}^{\infty}\mathrm{d}q_1\ldots\int_{-\infty}^{\infty}\mathrm{d}q_{\mathrm{N}}\,\left\langle q+\frac{\xi}{2}\middle|e^{-\frac{\tau}{2}\hat{\mathrm{T}}}\middle|q_1\right\rangle e^{-\frac{\tau}{2}\mathrm{V}_{\mathrm{tot}}\left(s_0^{+},q_1\right)}\\ \times\left\langle s_0^{+}\middle|e^{-\tau\hat{\mathrm{H}}_{\mathrm{sys}}}\middle|s_1\right\rangle e^{-\frac{\tau}{2}\mathrm{V}_{\mathrm{tot}}(s_1,q_1)}\left\langle q_1\middle|e^{-\tau\hat{\mathrm{T}}}\middle|q_2\right\rangle e^{-\frac{\tau}{2}\mathrm{V}_{\mathrm{tot}}(s_1,q_2)}\left\langle s_1\middle|e^{-\tau\hat{\mathrm{H}}_{\mathrm{sys}}}\middle|s_2\right\rangle\ldots\\ \times\left\langle s_{\mathrm{N}-1}\middle|e^{-\tau\hat{\mathrm{H}}_{\mathrm{sys}}}\middle|s_0^{-}\right\rangle e^{-\frac{\tau}{2}\mathrm{V}_{\mathrm{tot}}\left(s_0^{-},q_{\mathrm{N}}\right)}\left\langle q_{\mathrm{N}}\middle|e^{-\frac{\tau}{2}\hat{\mathrm{T}}}\middle|q-\frac{\xi}{2}\right\rangle\exp\left(-i\frac{p\xi}{\hbar}\right)\end{aligned} \tag{7.2.13}$$

Consider the matrix elements corresponding to the terminal two high-temperature factors, which involve the

difference coordinate ξ

$$\left\langle q+\frac{\xi}{2}\middle|\exp\left(-\frac{\tau}{2}\hat{\mathrm{T}}\right)\middle|q_1\right\rangle \propto \exp\left(-\frac{m}{\hbar^2\tau}\left(q+\frac{\xi}{2}-q_1\right)^2\right) \tag{7.2.14}$$

$$\left\langle q_{\mathrm{N}}\middle|\exp\left(-\frac{\tau}{2}\hat{\mathrm{T}}\right)\middle|q-\frac{\xi}{2}\right\rangle \propto \exp\left(-\frac{m}{\hbar^2\tau}\left(q-\frac{\xi}{2}-q_{\mathrm{N}}\right)^2\right). \tag{7.2.15}$$

We can ignore the normalization constants because in Monte Carlo,[15] the sampling function is autonormalized. Now, separating out the difference coordinate integral in Equation 7.2.13

$$\begin{aligned}\mathrm{W}\left(s_0^{\pm},q,p\right) = (2\pi\hbar)^{-\frac{1}{2}}\sum_{s_1}\cdots\sum_{s_{\mathrm{N}-1}}\int_{-\infty}^{\infty}\mathrm{d}q_1\ldots\int_{-\infty}^{\infty}\mathrm{d}q_{\mathrm{N}}\ \langle q|e^{-\frac{\tau}{2}\hat{\mathrm{T}}}|q_1\rangle\, e^{-\frac{\tau}{2}\mathrm{V_{tot}}\left(s_0^{+},q_1\right)}\\ \times\ \left\langle s_0^{+}\middle|e^{-\tau\hat{\mathrm{H}}_{\mathrm{sys}}}\middle|s_1\right\rangle e^{-\frac{\tau}{2}\mathrm{V_{tot}}(s_1,q_1)}\,\langle q_1|e^{-\tau\hat{\mathrm{T}}}|q_2\rangle\, e^{-\frac{\tau}{2}\mathrm{V_{tot}}(s_1,q_2)}\,\langle s_1|e^{-\tau\hat{\mathrm{H}}_{\mathrm{sys}}}|s_2\rangle\ldots\\ \times\ \left\langle s_{\mathrm{N}-1}\middle|e^{-\tau\hat{\mathrm{H}}_{\mathrm{sys}}}\middle|s_0^{-}\right\rangle e^{-\frac{\tau}{2}\mathrm{V_{tot}}\left(s_0^{-},q_{\mathrm{N}}\right)}\,\langle q_{\mathrm{N}}|e^{-\frac{\tau}{2}\hat{\mathrm{T}}}|q\rangle\\ \times\ \int_{-\infty}^{\infty}\mathrm{d}\xi\exp\left(-\frac{m}{2\hbar^2\tau}\xi^2-\xi\left(\frac{m}{\hbar^2\tau}\left(q_{\mathrm{N}}-q_1\right)+i\frac{p}{\hbar}\right)\right)\end{aligned} \tag{7.2.16}$$

The ξ integral in Equation 7.2.16 is what gives us the correct momentum distribution.

$$\begin{aligned}\int_{-\infty}^{\infty}\mathrm{d}\xi\exp\left(-\frac{m}{2\hbar^2\tau}\xi^2-\xi\left(\frac{m}{\hbar^2\tau}\left(q_{\mathrm{N}}-q_1\right)+i\frac{p}{\hbar}\right)\right) &= \sqrt{\frac{\pi\hbar^2\tau}{m}}\exp\left(\frac{\hbar^2\tau}{2m}\left(\frac{m}{\hbar^2\tau}\left(q_{\mathrm{N}}-q_1\right)^2+i\frac{p}{\hbar}\right)^2\right)\\ &= \sqrt{\frac{\pi\hbar^2\tau}{m}}\exp\left(\frac{m}{2\hbar^2\tau}\left(q_{\mathrm{N}}-q_1\right)^2\right)\right)\exp\left(-\tau\frac{p^2}{2m}+i\frac{p}{\hbar}\left(q_{\mathrm{N}}-q_1\right)\right)\end{aligned} \tag{7.2.17}$$

Substituting in Equation 7.2.16, it becomes

$$\begin{aligned}\mathrm{W}\left(s_0^{\pm},q,p\right) = (2\pi\hbar)^{-\frac{1}{2}}\sum_{s_1}\cdots\sum_{s_{\mathrm{N}-1}}\int_{-\infty}^{\infty}\mathrm{d}q_1\ldots\int_{-\infty}^{\infty}\mathrm{d}q_{\mathrm{N}}\, e^{-\frac{\tau}{2}\mathrm{V_{tot}}\left(s_0^{+},q_1\right)}\\ \times\ \left\langle s_0^{+}\middle|e^{-\tau\hat{\mathrm{H}}_{\mathrm{sys}}}\middle|s_1\right\rangle e^{-\frac{\tau}{2}\mathrm{V_{tot}}(s_1,q_1)}\,\langle q_1|e^{-\tau\hat{\mathrm{T}}}|q_2\rangle\, e^{-\frac{\tau}{2}\mathrm{V_{tot}}(s_1,q_2)}\,\langle s_1|e^{-\tau\hat{\mathrm{H}}_{\mathrm{sys}}}|s_2\rangle\ldots\\ \times\ \left\langle s_{\mathrm{N}-1}\middle|e^{-\tau\hat{\mathrm{H}}_{\mathrm{sys}}}\middle|s_0^{-}\right\rangle e^{-\frac{\tau}{2}\mathrm{V_{tot}}\left(s_0^{-},q_{\mathrm{N}}\right)}\,\langle q_{\mathrm{N}}|e^{-\frac{\tau}{2}\hat{\mathrm{T}}}|q\rangle\\ \times\exp\left(-\frac{2m}{\hbar^2\tau}\left(q-\frac{q_1+q_{\mathrm{N}}}{2}\right)^2\right)\exp\left(-\tau\frac{p^2}{2m}+i\frac{p}{\hbar}\left(q_{\mathrm{N}}-q_1\right)\right)\end{aligned} \tag{7.2.18}$$

From Equation 7.2.18, we see that the true momentum distribution, obtained by doing this integration is coupled

to the position distribution through q_1 and q_N. Here, the phase is unbound because there is no term holding q_1 close to q_N, which makes $\frac{p}{\hbar}(q_N - q_1)$ unbound, though p is bound by a Gaussian distribution. While sampling this distribution using Monte Carlo in multidimensional space, it is this phase term which gives rise to the so-called "sign problem". However, from our previous explorations of the Wigner phase space density in one-dimension,[17] we know that this correlation is low even in the most quantum of cases. So, instead of solving this integral exactly, we replace it by a more convenient distribution. If the solvent has a structure where a normal mode analysis is meaningful, insert the harmonic Wigner distribution for momentum

$$\mathrm{P}(p) \propto \exp\left(-\tanh\left(\frac{\hbar\omega\beta}{2}\right)\frac{p^2}{m\omega\hbar}\right) \tag{7.2.19}$$

otherwise we can use the classical Boltzmann factor for the momentum

$$\mathrm{P}(p) \propto \exp\left(-\beta\frac{p^2}{2m}\right) \tag{7.2.20}$$

Substituting one of the above choices for the momentum distribution into Equation 7.2.16, we get

$$\begin{aligned}\mathrm{W}\left(s_0^{\pm}, q, p\right) = (2\pi\hbar)^{-\frac{1}{2}} \sum_{s_1}\cdots\sum_{s_{N-1}}\int_{-\infty}^{\infty}\mathrm{d}q_1\ldots\int_{-\infty}^{\infty}\mathrm{d}q_N\ \langle q|e^{-\frac{\tau}{2}\hat{\mathrm{T}}}|q_1\rangle\, e^{-\frac{\tau}{2}\mathrm{V_{tot}}\left(s_0^+,q_1\right)} \\ \times\ \left\langle s_0^+\middle|e^{-\tau\hat{\mathrm{H}}_{\mathrm{sys}}}\middle|s_1\right\rangle e^{-\frac{\tau}{2}\mathrm{V_{tot}}(s_1,q_1)}\ \langle q_1|e^{-\tau\hat{\mathrm{T}}}|q_2\rangle\, e^{-\frac{\tau}{2}\mathrm{V_{tot}}(s_1,q_2)}\ \langle s_1|e^{-\tau\hat{\mathrm{H}}_{\mathrm{sys}}}|s_2\rangle\ldots \\ \times\ \left\langle s_{N-1}\middle|e^{-\tau\hat{\mathrm{H}}_{\mathrm{sys}}}\middle|s_0^-\right\rangle e^{-\frac{\tau}{2}\mathrm{V_{tot}}\left(s_0^-,q_N\right)}\ \langle q_N|e^{-\frac{\tau}{2}\hat{\mathrm{T}}}|q\rangle\,\mathrm{P}(p)\end{aligned} \tag{7.2.21}$$

Removing the resolution of identities, it is seen that Equation 7.2.21 is equivalent to

$$\mathrm{W}\left(s_0^{\pm}, q, p\right) \propto \mathrm{P}(p)\left\langle s_0^+, q\middle|\exp\left(-\beta\hat{\mathrm{H}}\right)\middle|s_0^-, q\right\rangle \tag{7.2.22}$$

Equation 7.2.22 can be evaluated easily using standard path integral Monte Carlo techniques. We notice that the phase space initial condition is no longer independent of the system initial condition. So, the separation of the initial density into a phase space distribution for the sovent degrees of freedom and a reduced density matrix for the system in Equation 7.2.3 and Equation 7.2.4 is no longer possible. Therefore we rewrite the QCPI equations for a coupled initial condition by removing the initial reduced density matrix from the expression for Q in Equation 7.2.4.

7.3 Numerical examples

Consider a standard two-level system (TLS) coupled to a harmonic bath. The Hamiltonian of the TLS in terms of the $|\mathrm{R}\rangle$ and $|\mathrm{L}\rangle$ is given by

$$\hat{\mathrm{H}}_0 = \hbar\Omega\left(|\mathrm{R}\rangle\langle\mathrm{L}| + |\mathrm{L}\rangle\langle\mathrm{R}|\right) \tag{7.3.1}$$

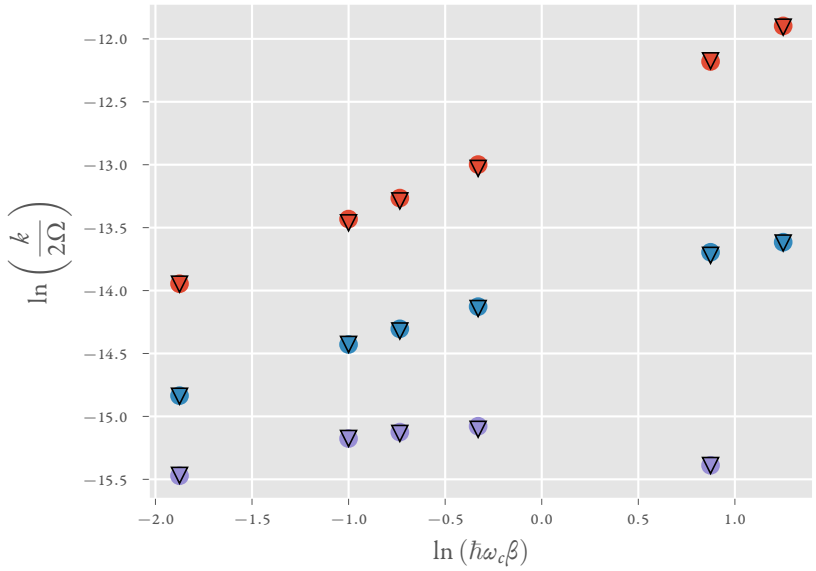

Figure 7.1: Consolidated rates. Comparisons between non-equilibrium method (filled circles) and near equilibrium (triangles). Red markers: $\xi = 0.1$. Blue markers: $\xi = 0.5$. Violet markers: $\xi = 1.5$.

which is coupled to a bath of harmonic oscillators through a bilinear coupling

$$\hat{\mathrm{H}}_{\mathrm{bath}} = \sum_j \frac{\hat{p}_j^2}{2} + \frac{1}{2} m_j \omega_j^2 \hat{x}_j^2 \tag{7.3.2}$$

$$\hat{\mathrm{V}}_{\mathrm{int}} = -\sum_j c_j \hat{x}_j \left(|\mathrm{R}\rangle\langle \mathrm{R}| - |\mathrm{L}\rangle\langle \mathrm{L}| \right) \tag{7.3.3}$$

The harmonic bath is characterized by an Ohmic spectral density[18]

$$\mathrm{J}(\omega) = \frac{\pi}{2} \hbar \xi \omega \exp\left(-\frac{\omega}{\omega_c} \right) \tag{7.3.4}$$

where ξ is the Kondo factor and ω_c is the cutoff frequency corresponding to the maximum of the Ohmic spectral density given in Equation 7.3.4. The parameters were taken from a previous paper by Topaler and Makri.[25] The TLS corresponds to a tunneling splitting of $2\hbar\Omega = 0.001\,05\,\mathrm{cm}^{-1}$ and the cutoff frequency is $\omega_c = 500\,\mathrm{cm}^{-1}$. These parameters, as mentioned in Chapter 6, are characteristic of many proton transfer and isomerization reactions. A high tunneling barrier leads to a small tunneling splitting, while the cutoff frequency is comparatively high. The bath was discretized into 300 oscillators using the logarithmic discretization procedure. QCPI was used for propagating the near equilibrium correlation function. Comparisons were made with the non-equilibrium flux method implemented using iQuAPI.[22,23]

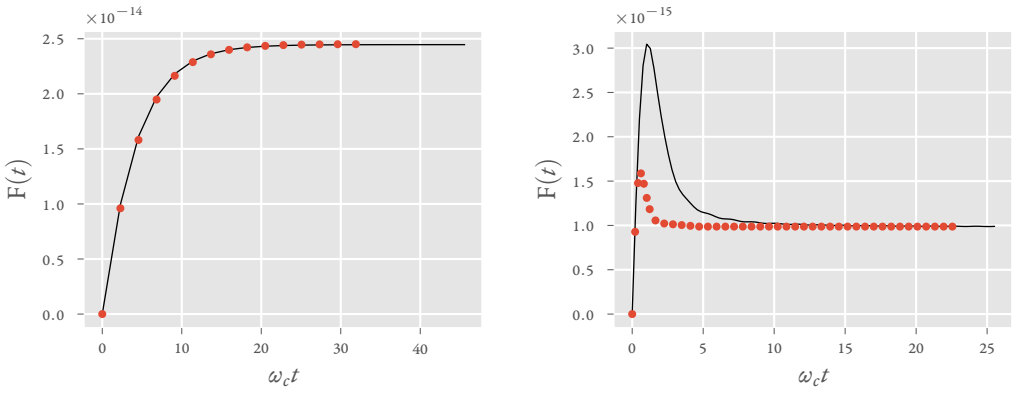

(a) $\xi = 0.1; \hbar\omega_c\beta = 2.40$

(b) $\xi = 1.5; \hbar\omega_c\beta = 2.40$

Figure 7.2: Flux as a function of time at room temperature. Black line: non-equilibrium initial condition. Red markers: near equilibrium initial condition.

In Figure 7.1, we compare the rates obtained using the two methods for a variety of parameters. We see that the rates are identical over the entire range of parameters. We expect that the plateau time would be much shorter because the initial conditions are much closer to the equilibrium Boltzmann distribution. To investigate this plateau time, in Figure 7.2, we look at Kondo parameters of $\xi = 0.1$ (low coupling) and $\xi = 1.5$ (high coupling). Both the figures are at room temperature ($\beta = 1052$). Notice that at the low coupling regime, Figure 7.2a, there is no difference between the near equilibrium flux correlation function and the non-equilibrium correlation function. However at high couplings, Figure 7.2b, there is observable difference owing to importance of transient effects. The near equilibrium initial conditions being closer to the true equilibrium density does not show as much transient behaviour as the non-equilibrium initial condition does. It also plateaus faster than its non-equilibrium counterpart.

7.4 Discussion and concluding remarks

In this chapter, we have discussed a way to create an initial condition for the flux correlation function that is close to the equilibrium density. This method plateaus to the correct rate much faster than the non-equilibrium initial condition. We also expect that it would plateau faster than other initial conditions that approximate the Boltzmannized operator.[14,32,33] We have shown that it mutes the transients substantially in very challenging parameter regimes. The near equilibrium initial condition also has a very elegant physical intuition behind it. It seems to indicate that at the dominant order, the system-solvent interaction affects the solvent position distribution. The momentum distribution remains comparatively unchanged. This is consistent with the understanding that the solvent equilibrates the system, and so should be centered on the various localized sites that the system can occupy. In fact, we are able to get the diagonal parts of the density matrix very accurately. The approximation is most severe in the off-diagonal terms, where the Wigner phase starts contributing.

With the PI-Wigner method for calculating the exact Wigner distribution discussed in Chapter 5, we should be able to directly couple the system to the bath and calculate the true equilibrium. This development is in progress. There are challenges associated with the "sign" problem in case of the off-diagonal terms of the system density matrix that need to be resolved. However the current initial condition, being approximate, does not suffer from such problems. Here we have just explored the flux correlation function with the intention of calculating the rate, which is guaranteed to be exact irrespective of the starting condition. So, the entire focus was on just decreasing the time scales of simulation. It would also be interesting to evaluate the near equilibrium initial condition as a starting point for approximating general correlation functions. There is a possibility that in the low coupling regimes this approximation might be remarkably accurate.

With this chapter, we conclude the work on rate theory. In Chapter 8, we discuss a new way of casting QCPI to provide exponential speedups while keeping all the advantages of solvent-driven propagators and dynamically consistent state hopping intact.

Chapter 8

Blip decomposition of QCPI under harmonic back reaction

8.1 Introduction

As we have been discussing, the QCPI method[26,27,29,36,37] provides a way to exactly incorporate the interaction between a fully atomistic solvent and a fully quantum mechanical system. This interaction makes the resultant dynamics non-Markovian. In a dissipative medium, this non-Markovian "memory" length is truncated. The memory length is determined by the correlation length of the solvent. The cost of QCPI grows exponentially with this memory length. A slow and sluggish solvent coupled with a system leads to long memories with short time steps, which can prove to be extremely challenging when starting with the full system as the reference.

Recent work[38–40] has enabled the use of "fully incoherent propagator" as a starting point of QuAPI instead of the bare system propagator. The bare system propagator uses all system paths. By the "fully incoherent" propagator or dynamics, we are referring to the phenomenon obtained by restricting the forward and the backward paths of the dynamics to be identical. For many reactions in strongly coupled solvents, especially where the dynamics is well described by a rate constant, the fully incoherent dynamics is a very good starting point. Exponential speedups over the old algorithm were observed even in cases where this blip-sum method was comparatively not as efficient. The motivation lay in the form of the influence functional for a harmonic bath.[22,23]

$$\mathrm{F}\left[\left\{s_j^{\pm}\right\}\right] = \exp\left(-\frac{1}{\hbar}\sum_{k=0}^{\mathrm{L}}\Delta s_k \sum_{l=0}^{k}\left(\mathrm{Re}\,\eta_{kl}\Delta s_l - 2i\,\mathrm{Im}\,\eta_{kl}\bar{s}_l\right)\right) \tag{8.1.1}$$

It can be seen that presence of multiple "blips", or points where the forward and the backward paths differ, leads to an exponential decrease in the probability amplitude. Thus the most important paths are those that do not have any blips. Therefore, it is very likely that the dynamics, in a strongly coupled environment, would be governed primarily by such fully "sojourn" paths. This is the first part of the method, which is the filtering on the basis of the number of blips. The second part of this method is dependent upon the observation that a fully sojourn path would not have any non-Markovian memory. So, it should be possible to sum over all such paths iteratively. This is achieved in what is called the implicit sojourn sum, which gives further speed up to all cases, irrespective of the number of blips required to converge the dynamics.

Developments in QCPI have significantly increased the time steps[36] that can be used and also successfully incor-

porated increasing portions of memory in the reference propagator, thereby further decreasing the effective memory.[37] With these improvements QCPI has already been used to study a fully atomistic system.[29] In this chapter we combine QCPI with the blip-summation method thereby further reducing the scaling of the method. In Section 8.2 we show how expressing the backreaction in an analytic form under the harmonic approximation and rearranging the terms can make it possible to implement an implicit sojourn sum algorithm. In Section 8.3, we go into details of the algorithm. Finally we present numerical examples in Section 8.4.

8.2 Blip decomposition of QCPI

The QCPI formalism combines a "reduced" dimensional, fully quantum mechanical system described by path integrals with a large dimensional solvent simulated using classical trajectories. The bare system is described by a D-dimensional Hamiltonian:

$$\hat{\mathrm{H}}_0 = \sum_{n,m}^{\mathrm{D}} h_{n,m} \left|\sigma_n\right\rangle\!\left\langle\sigma_m\right| \tag{8.2.1}$$

where σ_n represent the system DVR states, and the position operator in the system space is defined as

$$\hat{s} = \sum_{n} \sigma_n \left|\sigma_n\right\rangle\!\left\langle\sigma_n\right| \tag{8.2.2}$$

The total Hamiltonian has the form

$$\hat{\mathrm{H}} = \hat{\mathrm{H}}_0 + \hat{\mathrm{H}}_{\mathrm{sol}}\left(s, q, p\right) \tag{8.2.3}$$

where q, p are the solvent phase space points. Under QCPI, the reduced density matrix, ρ_{red} is given by

$$\rho_{\mathrm{red}}\left(s_{\mathrm{N}}^{\pm}; \mathrm{N}\Delta t\right) = \int \mathrm{d}q_0\, \mathrm{d}p_0\, \mathrm{P}\left(q_0, p_0\right)\, \mathrm{Q}\left(q_0, p_0, s_{\mathrm{N}}^{\pm}; \mathrm{N}\Delta t\right) \tag{8.2.4}$$

where P is the phase space density of the solvent and Q contains all the dynamical effects arising from the system-solvent interaction. It is calculated as a path integral over the system space.

$$\begin{aligned}
\mathrm{Q}\left(q_0, p_0, s_{\mathrm{N}}^{\pm}; \mathrm{N}\Delta t\right) = \sum_{s_{\mathrm{N}-1}^{\pm}} \sum_{s_{\mathrm{N}-2}^{\pm}} \cdots \sum_{s_0^{\pm}} & \left\langle s_{\mathrm{N}}^{+}\right|\hat{\mathrm{U}}_{\mathrm{ref}}\left(\mathrm{N}\Delta t, (\mathrm{N}-1)\Delta t; q_0, p_0\right)\left|s_{\mathrm{N\text{-}1}}^{+}\right\rangle \cdots \\
& \times \left\langle s_1^{+}\right|\hat{\mathrm{U}}_{\mathrm{ref}}\left(\Delta t, 0; q_0, p_0\right)\left|s_0^{+}\right\rangle \rho_{\mathrm{red}}\left(s_0^{\pm}; 0\right) \left\langle s_0^{-}\right|\hat{\mathrm{U}}_{\mathrm{ref}}^{\dagger}\left(\Delta t, 0; q_0, p_0\right)\left|s_1^{-}\right\rangle \cdots \\
& \times \left\langle s_{\mathrm{N}-1}^{-}\right|\hat{\mathrm{U}}_{\mathrm{ref}}^{\dagger}\left((\mathrm{N}-1)\Delta t, \mathrm{N}\Delta t; q_0, p_0\right)\left|s_{\mathrm{N}}^{-}\right\rangle \exp\left(\frac{i}{\hbar}\varphi\left(q_0, p_0, \left\{s_j^{\pm}\right\}\right)\right)
\end{aligned} \tag{8.2.5}$$

where φ is the solvent backreaction on the system that appears as a path-dependent phase, and $\mathrm{U}_{\mathrm{ref}}$ is the solvent-

driven reference propagator obtained by solving the time-dependent Schrödinger equation for the system propagator under a time dependent "reference" Hamiltonian

$$\hat{\mathrm{H}}_{\mathrm{ref}}\left(t;q_0,p_0\right)=\hat{\mathrm{H}}_0+\hat{\mathrm{H}}_{\mathrm{sol}}\left(s,q_{\mathrm{ref}}(t),p_{\mathrm{ref}}(t)\right) \tag{8.2.6}$$

$$\varphi\left(q_0,p_0,\left\{s_j^{\pm}\right\}\right)=\int \mathrm{d}t\left(\Delta\mathrm{H}_{\mathrm{sol}}\left(\left\{s_j^{\pm}\right\},q(t),p(t)\right)-\Delta\mathrm{H}_{\mathrm{sol}}\left(\left\{s_j^{\pm}\right\},q_{\mathrm{ref}}(t),p_{\mathrm{ref}}(t)\right)\right) \tag{8.2.7}$$

where $(q_{\mathrm{ref}},p_{\mathrm{ref}})$ is the reference phase-space trajectory of the solvent with the initial conditions (q_0,p_0). This reference trajectory feels is evolved under system forces corresponding to $\left\{s_j^{\mathrm{ref}}\right\}$ chosen as an ansatz. $(q(t),p(t))$ is the phase-space trajectory of the solvent under the system forces with the same initial conditions.

Let us rewrite Equation 8.2.5 in terms of a super-operator, L defined as

$$\begin{aligned}\mathrm{L}_j\left(s_{j+1}^{+},s_{j+1}^{-},s_j^{+},s_j^{-};q_0,p_0\right)&=\left\langle s_{j+1}^{+}\middle|\hat{\mathrm{U}}\left(\left(j+1\right)\Delta t,j\Delta t;q_0,p_0\right)\middle|s_j^{+}\right\rangle\\&\times\left\langle s_j^{-}\middle|\hat{\mathrm{U}}^{\dagger}\left(\left(j+1\right)\Delta t,j\Delta t;q_0,p_0\right)\middle|s_{j+1}^{-}\right\rangle\end{aligned} \tag{8.2.8}$$

$$\begin{aligned}\mathrm{Q}\left(q_0,p_0,s_{\mathrm{N}}^{\pm};\mathrm{N}\Delta t\right)&=\sum_{s_{\mathrm{N}-1}^{\pm}}\sum_{s_{\mathrm{N}-2}^{\pm}}\cdots\sum_{s_0^{\pm}}\mathrm{L}_{\mathrm{N}-1}\left(s_{\mathrm{N}}^{\pm},s_{\mathrm{N}-1}^{\pm};q_0,p_0\right)\mathrm{L}_{\mathrm{N}-2}\left(s_{\mathrm{N}-1}^{\pm},s_{\mathrm{N}-2}^{\pm};q_0,p_0\right)\cdots\\&\times\mathrm{L}_0\left(s_1^{\pm},s_0^{\pm};q_0,p_0\right)\left\langle s_0^{+}\middle|\hat{\rho}_{\mathrm{red}}\left(0\right)\middle|s_0^{-}\right\rangle\exp\left(\frac{i}{\hbar}\varphi\left(q_0,p_0,\left\{s_j^{\pm}\right\}\right)\right)\end{aligned} \tag{8.2.9}$$

$\mathrm{L}_j\left(s_{j+1}^{+},s_{j+1}^{-},s_j^{+},s_j^{-};q_0,p_0\right)$ will also be written as $\mathrm{L}_j\left(s_{j+1}^{\pm},s_j^{\pm};q_0,p_0\right)$. L_j is a tensor and is represented in the system's basis as a $\mathrm{D}^2\times\mathrm{D}^2$ matrix. The notation $\left\{s_j^{\pm}\right\}$ is used to denote the entire path. j in this expression is a dummy variable without any signficance.

Under harmonic backreaction, the backreaction is obtained from the harmonic bath obtained from the solvent. All effects of anharmonicity is preserved in full atomistic detail in the propagator. In this case the phase becomes independent of the initial condition of the solvent mode. It can be shown that the path dependent backreaction is of the form[41]

$$\varphi\left(\left\{s_j^{\pm}\right\}\right)=\sum_{k=0}^{\mathrm{N}}\sum_{k'=0}^{k}\Delta s_k\left[\left(\bar{s}_{k'}-s_{k'-1}^{\mathrm{ref}}\right)\gamma_{kk'}^{(0)}+\left(\bar{s}_{k'}-s_{k'}^{\mathrm{ref}}\right)\gamma_{kk'}^{(1)}\right] \tag{8.2.10}$$

We list here the γ coefficients for convenience:

$$\gamma_{00}^{(1)}=\gamma_{\mathrm{NN}}^{(0)}=\sum_j\frac{c_j^2}{m_j\omega_j^3}\left(\frac{\omega_j\Delta t}{2}-\sin\left(\frac{\omega_j\Delta t}{2}\right)\right) \tag{8.2.11}$$

$$\gamma_{00}^{(0)}=\gamma_{\mathrm{NN}}^{(1)}=0 \tag{8.2.12}$$

$$\gamma_{kk}^{(0)}=\sum_j\frac{c_j^2}{m_j\omega_j^3}\left(\frac{\omega_j\Delta t}{2}+\sin\left(\frac{\omega_j\Delta t}{2}\right)-\sin\left(\omega_j\Delta t\right)\right) \tag{8.2.13}$$

$$\gamma_{kk}^{(1)} = \gamma_{00}^{(1)} \tag{8.2.14}$$

$$\gamma_{\mathrm{N}0}^{(1)} = \sum_j \frac{4c_j^2}{m_j\omega_j^3} \sin^2\left(\frac{\omega_j\Delta t}{4}\right) \sin\left(\left(\mathrm{N} - \tfrac{1}{2}\right)\omega_j\Delta t\right) \tag{8.2.15}$$

$$\gamma_{k0}^{(1)} = \sum_j \frac{4c_j^2}{m_j\omega_j^3} \sin\left(\frac{\omega_j\Delta t}{4}\right) \sin\left(\frac{\omega_j\Delta t}{2}\right) \sin\left(\left(k - \tfrac{1}{4}\right)\omega_j\Delta t\right) \tag{8.2.16}$$

$$\gamma_{\mathrm{N}0}^{(0)} = \gamma_{k0}^{(0)} = 0 \tag{8.2.17}$$

$$\gamma_{\mathrm{N}k}^{(0)} = \sum_j \frac{4c_j^2}{m_j\omega_j^3} \sin^2\left(\frac{\omega_j\Delta t}{4}\right) \sin\left(\left(\mathrm{N} - k\right)\omega_j\Delta t\right) \tag{8.2.18}$$

$$\gamma_{\mathrm{N}k}^{(1)} = \sum_j \frac{4c_j^2}{m_j\omega_j^3} \sin^2\left(\frac{\omega_j\Delta t}{4}\right) \sin\left(\left(\mathrm{N} - k - \tfrac{1}{2}\right)\omega_j\Delta t\right) \tag{8.2.19}$$

$$\gamma_{kk'}^{(0)} = \sum_j \frac{4c_j^2}{m_j\omega_j^3} \sin\left(\frac{\omega_j\Delta t}{4}\right) \sin\left(\frac{\omega_j\Delta t}{2}\right) \sin\left(\left(k - k' + \tfrac{1}{4}\right)\omega_j\Delta t\right) \tag{8.2.20}$$

$$\gamma_{kk'}^{(1)} = \sum_j \frac{4c_j^2}{m_j\omega_j^3} \sin\left(\frac{\omega_j\Delta t}{4}\right) \sin\left(\frac{\omega_j\Delta t}{2}\right) \sin\left(\left(k - k' - \tfrac{1}{4}\right)\omega_j\Delta t\right) \tag{8.2.21}$$

Substituting Equation 8.2.10 in Equation 8.2.9 and rearranging, we get

$$\begin{aligned}
\mathrm{Q}\left(q_0, p_0, s_{\mathrm{N}}^{\pm}; \mathrm{N}\Delta t\right) = &\sum_{s_{\mathrm{N}-1}^{\pm}} \sum_{s_{\mathrm{N}-2}^{\pm}} \cdots \sum_{s_0^{\pm}} \left(\mathrm{L}_{\mathrm{N}-1}\left(s_{\mathrm{N}}^{\pm}, s_{\mathrm{N}-1}^{\pm}; q_0, p_0\right) \exp\left(\frac{i}{\hbar}\varphi_{\mathrm{N}}\left(\left\{s_j^{\pm}\right\}\right)\right)\right) \\
&\times \left(\mathrm{L}_{\mathrm{N}-2}\left(s_{\mathrm{N}-1}^{\pm}, s_{\mathrm{N}-2}^{\pm}; q_0, p_0\right) \exp\left(\frac{i}{\hbar}\varphi_{\mathrm{N}-1}\left(\left\{s_j^{\pm}\right\}\right)\right)\right) \cdots \\
&\times \left(\mathrm{L}_0\left(s_1^{\pm}, s_0^{\pm}; q_0, p_0\right) \exp\left(\frac{i}{\hbar}\varphi_1\left(\left\{s_j^{\pm}\right\}\right)\right)\right) \\
&\times \exp\left(\frac{i}{\hbar}\varphi_0\left(\left\{s_j^{\pm}\right\}\right)\right) \left\langle s_0^{+}\right| \rho_{\mathrm{red}}(0) \left|s_0^{-}\right\rangle
\end{aligned} \tag{8.2.22}$$

where we have decomposed the full backreaction as a sum over

$$\varphi_k\left(\left\{s_j^{\pm}\right\}\right) = \sum_{n=k}^{\mathrm{N}} \Delta s_n \left[\left(\bar{s}_k - s_{k-1}^{\mathrm{ref}}\right)\gamma_{nk}^{(0)} + \left(\bar{s}_k - s_k^{\mathrm{ref}}\right)\gamma_{nk}^{(1)}\right] \tag{8.2.23}$$

The expression for Q, as written in Equation 8.2.22 makes it trivial to incorporate iterative propagation. Suppose the memory length is N time steps. Then using the fact that the γ coefficients, and consequently the backreaction, do not couple the time points beyond a distance of N, $\mathrm{Q}\left(q_0, p_0, s_{\mathrm{N}+1}^{\pm}; (\mathrm{N}+1)\Delta t\right)$ is given as

$$\mathrm{Q}\left(q_0, p_0, s_{\mathrm{N}}^{\pm}; (\mathrm{N}+1)\Delta t\right) = \sum_{s_{\mathrm{N}}^{\pm}} \sum_{s_{\mathrm{N}}^{\pm}} \cdots \sum_{s_1^{\pm}} \left(\mathrm{L}_{\mathrm{N}}\left(s_{\mathrm{N}+1}^{\pm}, s_{\mathrm{N}}^{\pm}; q_0, p_0\right) \exp\left(\frac{i}{\hbar}\varphi_{\mathrm{N}}\left(\left\{s_j^{\pm}\right\}\right)\right)\right)$$

$$\times \left(\mathrm{L}_{\mathrm{N}-1}\left(s_{\mathrm{N}}^{\pm}, s_{\mathrm{N}-1}^{\pm}; q_0, p_0\right) \exp\left(\frac{i}{\hbar}\varphi_{\mathrm{N}-1}\left(\left\{s_j^{\pm}\right\}\right)\right)\right)\cdots$$
$$\times \sum_{s_0^{\pm}} \left[\left(\mathrm{L}_0\left(s_1^{\pm}, s_0^{\pm}; q_0, p_0\right) \exp\left(\frac{i}{\hbar}\varphi_1\left(\left\{s_j^{\pm}\right\}\right)\right)\right)\right.$$
$$\left. \times \exp\left(\frac{i}{\hbar}\varphi_0\left(\left\{s_j^{\pm}\right\}\right)\right) \left\langle s_0^{+}\middle|\rho_{\mathrm{red}}(0)\middle|s_0^{-}\right\rangle \right] \tag{8.2.24}$$

If the entire memory is being spanned, the $\gamma_{k,k'}$ coefficients depend only on the difference $k - k'$. The inner-most sum can then be computed iteratively as matrix-vector multiplications, thus keeping the number of paths constant. In the first step of iteration, we sum over $s_0^{\pm}$ and get paths depending on $s_1^{\pm}$ through $s_{\mathrm{N}+1}^{\pm}$. In the second step, we sum over $s_1^{\pm}$ getting paths depending on $s_2^{\pm}$ through $s_{\mathrm{N}+2}^{\pm}$. The computational complexity, therefore, grows linearly with time steps after the memory has been spanned.

8.3 Efficient implementation of blips in QCPI

QCPI generally starts with the solvent driven reference and corrects the dynamics thereon. It has been seen that using the fully incoherent limit, where the forward and backward system paths are identical can prove to be very useful. Subsequently paths are included according to increasing number of blips. Since interaction between two blips leads to an exponential decay in the amplitude of a path, the significance of a path decreases with increasing blips within the span of memory.

There are D^{N} such fully sojourn paths where D is the number of system DVR states and N is the number of time steps. Since for all these paths $\Delta s = 0$ for all time points, the backreaction $\varphi = 1$.

$$\mathrm{Q}^{(0)}\left(q_0, p_0, s_{\mathrm{N}}^{\pm}; \mathrm{N}\Delta t\right) = \sum_{s_{\mathrm{N}-1}^{\pm}} \sum_{s_{\mathrm{N}-2}^{\pm}} \cdots \sum_{s_0^{\pm}} \mathrm{T}_{\mathrm{N}-1}^{(00)}\left(s_{\mathrm{N}}^{\pm}, s_{\mathrm{N}-1}^{\pm}; q_0, p_0\right) \mathrm{T}_{\mathrm{N}-2}^{(00)}\left(s_{\mathrm{N}-1}^{\pm}, s_{\mathrm{N}-2}^{\pm}; q_0, p_0\right)\cdots$$
$$\times \mathrm{T}_0^{(00)}\left(s_1^{\pm}, s_0^{\pm}; q_0, p_0\right) \left\langle s_0^{+}\middle|\rho_{\mathrm{red}}(0)\middle|s_0^{-}\right\rangle \tag{8.3.1}$$
$$\mathrm{T}_j^{(00)}\left(s_{j+1}^{\pm}, s_j^{\pm}; q_0, p_0\right) = \mathrm{L}_j\left(s_{j+1}^{\pm}, s_j^{\pm}; q_0, p_0\right) \exp\left(\frac{i}{\hbar}\varphi_{j+1}\left(\left\{s_k^{\pm}\right\}\right)\right)$$
$$\times \delta\left(s_{j+1}^{+} - s_{j+1}^{-}\right) \delta\left(s_j^{+} - s_j^{-}\right) \tag{8.3.2}$$

The phase terms in the expression for $\mathrm{Q}^{(0)}$ are all unity because there are no blips. $\Delta s_j = 0$ for all j. So, the zero blips paths can be solved together using iterated matrix-vector products. The (00) in $\mathrm{T}^{(00)}$ indicates that it transfers a sojourn to a sojourn. The computational cost grows as $\mathrm{O}\left(\mathrm{ND}^4\right)$, because $\mathrm{T}^{(00)}$ is a $\mathrm{D}^2 \times \mathrm{D}^2$ matrix whereas the number of paths in the naïve algorithm grows as $\mathrm{O}\left(\mathrm{D}^{\mathrm{N}}\right)$. In fact, we can utilize the sparseness of the $\mathrm{T}^{(00)}$ matrix and come up with a $\mathrm{O}\left(\mathrm{ND}^2\right)$ algorithm for computing the iterative matrix-vector products. This is important for increasing the number of system states. However, here we are interested in systems of a fixed dimensionality. So, the observation of key importance here is that the dependence on the number of time steps is linear and not exponential.

Now consider a path where a blip exists at a time index k

$$\begin{aligned}\mathrm{Q}^{(1)}\left(q_0,p_0,s_\mathrm{N};\mathrm{N}\Delta t\right) = &\sum_{s^{\pm}_{\mathrm{N}-1}}\sum_{s^{\pm}_{\mathrm{N}-2}}\cdots\sum_{s^{\pm}_{0}}\mathrm{T}^{(00)}_{\mathrm{N}-1}\left(s^{\pm}_{\mathrm{N}},s^{\pm}_{\mathrm{N}-1};q_0,p_0\right)\mathrm{T}^{(00)}_{\mathrm{N}-2}\left(s^{\pm}_{\mathrm{N}-1},s^{\pm}_{\mathrm{N}-2};q_0,p_0\right)\cdots\\ &\times\mathrm{T}^{(00)}_{k+1}\left(s^{\pm}_{k+2},s^{\pm}_{k+1};q_0,p_0\right)\mathrm{T}^{(01)}_{k}\left(s^{\pm}_{k+1},s^{\pm}_{k};q_0,p_0\right)\mathrm{T}^{(10)}_{k-1}\left(s^{\pm}_{k},s^{\pm}_{k-1};q_0,p_0\right)\cdots\\ &\times\mathrm{T}^{(00)}_{0}\left(s^{\pm}_{1},s^{\pm}_{0};q_0,p_0\right)\left\langle s^{\pm}_{0}\middle|\rho_{\mathrm{red}}\left(0\right)\middle|s^{\pm}_{0}\right\rangle\end{aligned} \tag{8.3.3}$$

$$\mathrm{T}^{(10)}_{j}\left(s^{\pm}_{j+1},s^{\pm}_{j};q_0,p_0\right) = \begin{cases}\mathrm{L}_j\left(s^{\pm}_{j+1},s^{\pm}_{j};q_0,p_0\right)\exp\left(\frac{i}{\hbar}\varphi_{j+1}\left(\left\{s^{\pm}_{k}\right\}\right)\right), & \text{if } s^{+}_{j+1}\neq s^{-}_{j+1}, s^{+}_{j}=s^{-}_{j}\\ 0, \quad \text{otherwise}\end{cases} \tag{8.3.4}$$

$$\mathrm{T}^{(01)}_{j}\left(s^{\pm}_{j+1},s^{\pm}_{j};q_0,p_0\right) = \begin{cases}\mathrm{L}_j\left(s^{\pm}_{j+1},s^{\pm}_{j};q_0,p_0\right)\exp\left(\frac{i}{\hbar}\varphi_{j+1}\left(\left\{s^{\pm}_{k}\right\}\right)\right), & \text{if } s^{+}_{j+1}=s^{-}_{j+1}, s^{+}_{j}\neq s^{-}_{j}\\ 0, \quad \text{otherwise}\end{cases} \tag{8.3.5}$$

Now, if there is more than one blip in a path, the only case that is left to be considered is that of two consecutive blips. In that case the transfer matrix would be

$$\mathrm{T}^{(11)}_{j}\left(s^{\pm}_{j+1},s^{\pm}_{j};q_0,p_0\right) = \begin{cases}\mathrm{L}_j\left(s^{\pm}_{j+1},s^{\pm}_{j};q_0,p_0\right)\exp\left(\frac{i}{\hbar}\varphi_{j+1}\left(\left\{s^{\pm}_{k}\right\}\right)\right), & \text{if } s^{+}_{j+1}\neq s^{-}_{j+1}, s^{+}_{j}\neq s^{-}_{j}\\ 0, \quad \text{otherwise}\end{cases} \tag{8.3.6}$$

It is known that the number of paths required to span all blips over N time steps would be $\binom{\mathrm{D}+1}{2}^{\mathrm{N}}$ which is significantly less than $\mathrm{D}^{2\mathrm{N}}$.[38–40] The benefit increases when the environment is significantly coupled to the system, and very few blips are required for convergence. However there are benefits even in case of a weakly coupled solvent.

8.4 Numerical examples

We illustrate the bQCPI method with numerical examples on the standard spin-boson model. In terms of left ($|\mathrm{L}\rangle$) and right ($|\mathrm{R}\rangle$) states, the two-level system (TLS) Hamiltonian is given by

$$\hat{\mathrm{H}}_{\mathrm{sys}} = -\hbar\Omega\left(|\mathrm{R}\rangle\langle\mathrm{L}| + |\mathrm{L}\rangle\langle\mathrm{R}|\right) \tag{8.4.1}$$

while the harmonic bath interacting with the system has the standard bilinear coupling

$$\hat{\mathrm{H}}_{\mathrm{env}} = \sum_j \frac{\hat{p}_j^2}{2m_j} + \frac{1}{2}m_j\omega_j^2\hat{x}_j^2 \tag{8.4.2}$$

$$\hat{\mathrm{V}}_{\mathrm{int}} = -\sum_j c_j\hat{x}_j\left(|\mathrm{R}\rangle\langle\mathrm{R}| - |\mathrm{L}\rangle\langle\mathrm{L}|\right) \tag{8.4.3}$$

The bath is described by a spectral density. Here we use the standard Ohmic form[18]

$$J(\omega) = \frac{\pi}{2}\xi\hbar\omega \exp\left(-\frac{\omega}{\omega_c}\right) \tag{8.4.4}$$

where ξ is the Kondo parameter and ω_c is the "cutoff" frequency corresponding to the maximum of Equation 7.3.4. The spectral density was discretized using logarithmic discretization using 60 oscillators.

The dynamics is calculated using the bQCPI method and results are compared to the converged QCPI or QuAPI calculations. In Figure 8.1, we show the results for three different regimes, along with the effect of adding paths containing the given number of blips. We notice that the relative importance of a path decreases dramatically with the number of blips. All the parameters tested in Figure 8.1 have very fast baths, which is not the ideal case to study the improvements obtained through blip summation.

In Figure 8.1a, we consider a system strongly coupled to a fast bath at a high temperature: $\omega_c = 2.5\Omega; \xi = 1.2; \hbar\Omega\beta = 0.2$. Of all the cases in Figure 8.1, it is here that we gain maximally from the blip summation approach. Convergence was reached with a time step of $\Omega\Delta t = 0.5$, and a memory length spanning $3\Delta t$. The fully incoherent limit itself was pretty close. On adding just one blip, we reached convergence using just 9 paths. Without blips, a $k_{\max} = 3$ calculation would need 256 paths. Even when all blips were considered, bQCPI required just 81 paths. This is a result of the scaling of the full calculation going down from $D^{2(k_{\max}+1)}$ to $\binom{D+1}{2}^{(k_{\max}+1)}$ when using the blip summation algorithm ($k_{\max}$ here represents the memory length, and D the system dimensionality). The next two examples are in regimes which do not magnify the efficiency obtained from blips. The low coupling strength implies that the relative importance of paths with more blips would not decrease as dramatically with the number of blips present, leading to convergence only being achieved at relatively high number of blips. However, there is still an enormous cost saving that happens allowing us to go to higher memories more easily. In Figure 8.1b and 8.1c, since temperature and coupling are low, the cost of adding an additional blip to the path amplitude is not huge. So, a large number of blips are required to converge the results. Calculations were done with a memory of $k_{\max} = 10\Delta t$, which would generally require 4^{11} paths. At converged number of blips, for Figure 8.1b roughly 0.2% paths were used (upto 4 blips considered). For Figure 8.1c, roughly 0.5% of all the paths were used with convergence being achieved at 5 blips. Given that there is no longer the exponential proliferation of classical trajectories with time, because of harmonic backreaction with analytical coefficients, the cost of calculation is further decreased from standard QCPI.

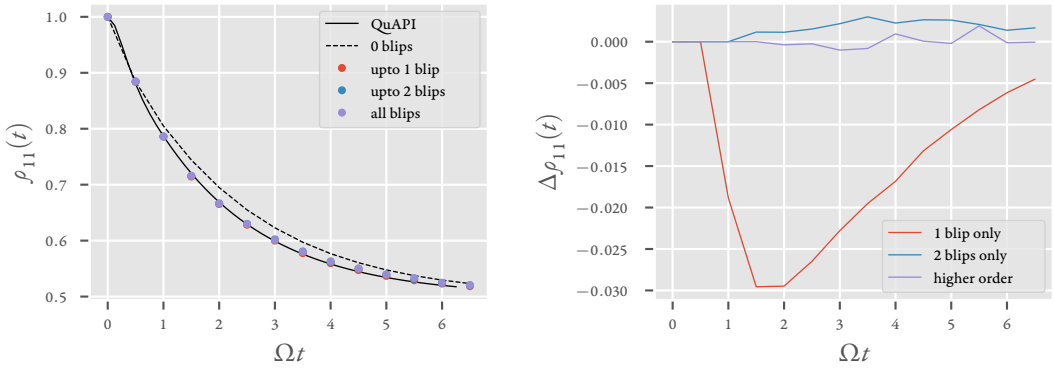

(a) $\omega_c = 2.5\Omega; \xi = 1.2; \hbar\Omega\beta = 0.2$

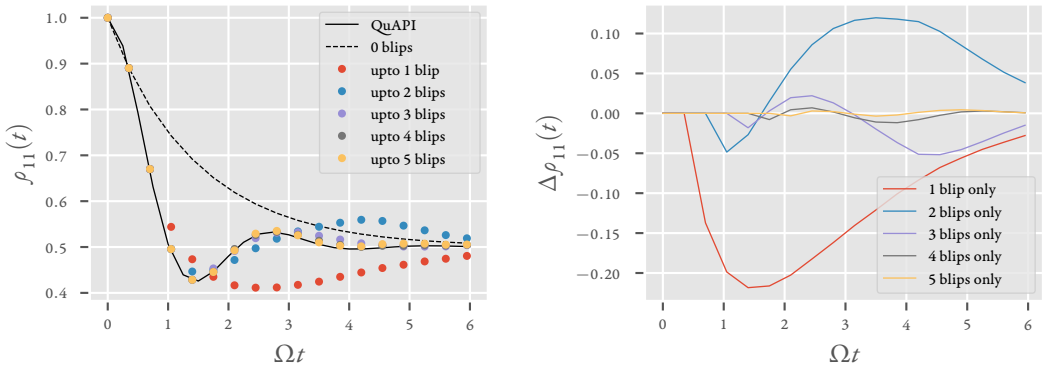

(b) $\omega_c = 2.5\Omega; \xi = 0.6; \hbar\Omega\beta = 2.5$

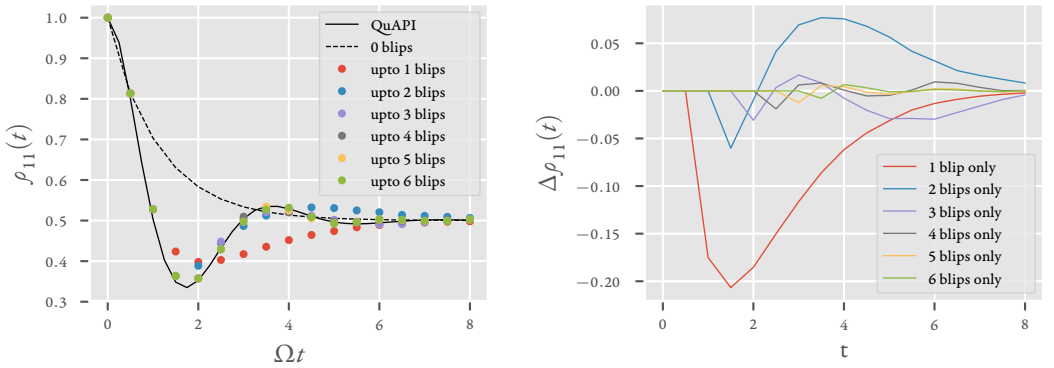

(c) $\omega_c = 5\Omega; \xi = 0.3; \hbar\Omega\beta = 5$

Figure 8.1: Examples of the dynamics of a two-level system coupled to a harmonic bath at various parameters. Left panel shows the dynamics at various levels; Right panel shows the corrections due to separate number of blips.

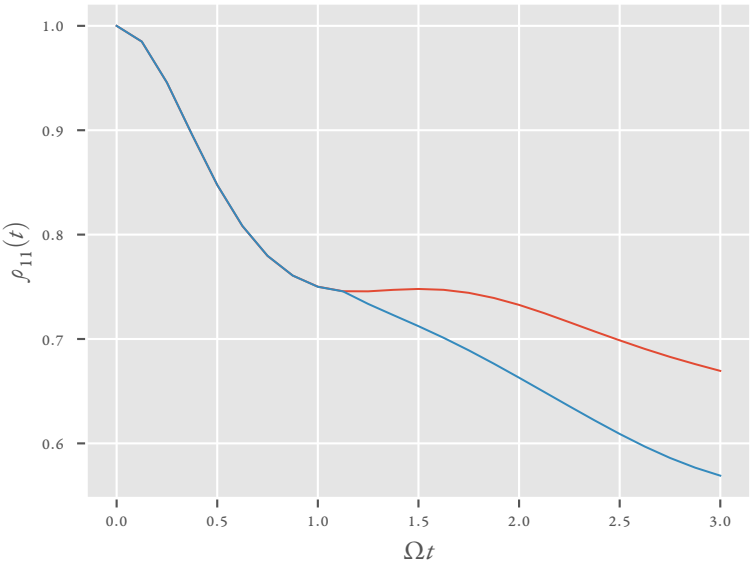

Figure 8.2: Comparison between converged calculations with DCSH (red solid line) with calculations without DCSH (blue solid line) with $\Delta t = 0.125$ and $k_{\max} = 9$. The harmonic bath is characterized by $\omega_c = \Omega; \xi = 2; \hbar\Omega\beta = 1$.

Finally we want to ensure that the bQCPI procedure can take advantage of the various hopping schemes. To that end, in Figure 8.2, we consider a case of a sluggish bath $\omega_c = \Omega$ with a high coupling $\xi = 2$ at a moderate temperature $\hbar\Omega\beta = 1$. We compare the fully converged dynamically consistent state hopping (DCSH) results to the random hopping results with a reference forced by the mean surface at the same parameters ($\Delta t = 0.125; k_{\max} = 9$). The non-DCSH results are completely unconverged. QCPI captures all the real memory implicitly in the solvent driven reference propagators. The only portion, therefore, that leads to the exponential growth of paths is the quantum part of memory. As discussed by Walters and Makri,[37] DCSH is one way to capture more of the quantum memory into the solvent driven reference propagators. Further, it has been shown that keeping the reference consistent with the branching scheme leads to reduction of spurious memory. Thus, the bQCPI with the DCSH reference and branching leads to low amount of memory in comparison to any other. The bQCPI method is also setup to take full advantage of future improvements in reference and branching schemes.

8.5 Discussion and concluding remarks

We have developed here a methodology for combining the blip summation method with QCPI. The goal is to ensure through this combination that the main advantages of QCPI remain intact. We want to have larger time steps and shorter memories that can be obtained through QCPI, while taking advantage of improved scaling that blip

summation can give. We have successfully derived the method and shown its improved convergence at a variety of parameters. Like the original blip summation method for QuAPI, the maximum benefit is obtained when the bath is sluggish and strongly coupled to the system. This also happens to be the case where the dynamics has long timescales and can afford very short time steps. For such processes, it can be seen that bQCPI converges with very few paths. Even in the most unfavorable parameter regime, where the solvent is fast or not strongly coupled to the system, we show that bQCPI still has much better scaling properties. This exponential speedup increases as the number of states used to represent the system increases. This is especially beneficial for long reactions. We expect bQCPI to also be useful for calculating the rate in cases where it is still infeasible to carry out simulation of the full dynamics over the entire time scale.

References

[1] A. Bose and N. Makri, "Non-equilibrium reactive flux: A unified framework for slow and fast reaction kinetics", J. Chem. Phys. **147**, 152723 (2017).

[2] R. Kubo, "Statistical Mechanical Theory of Irreversible Processes. I. General Theory and Simple Applications to Magnetic and Conduction Problems", J. Phys. Soc. Japan **12**, 570–586 (1957).

[3] T. Yamamoto, "Quantum statistical mechanical theory of the rate of exchange chemical reactions in the gas phase", J. Chem. Phys. **33**, 281–289 (1960).

[4] J. C. Keck, "Variational Theory of Chemical Reaction Rates Applied to 3-Body Recombinations", J. Chem. Phys. **32**, 1035–1050 (1960).

[5] J. C. Keck, "Variational Theory of Reaction Rates", in *Adv. chem. phys.* Vol. XIII (1967), pp. 85–121.

[6] R. Kapral, "Internal relaxation in chemically reacting fluids", J. Chem. Phys. **56**, 1842–1847 (1972).

[7] W. H. Miller, "Quantum mechanical transition state theory and a new semiclassical model for reaction rate constants", J. Chem. Phys. **61**, 1823 (1974).

[8] W. H. Miller, S. D. Schwartz, and J. W. Tromp, "Quantum mechanical rate constants for bimolecular reactions", J. Chem. Phys. **79**, 4889–4898 (1983).

[9] D. Chandler, "Statistical mechanics of isomerization dynamics in liquids and the transition state approximation", J. Chem. Phys. **68**, 2959 (1978).

[10] D. Chandler, *Introduction to Modern Statistical Mechanics* (Oxford University Press, 1987).

[11] P. Hänggi, P. Talkner, and M. Borkovec, "Reaction-rate theory: Fifty years after Kramers", Rev. Mod. Phys. **62**, 251–341 (1990).

[12] W. H. Miller, "Spiers Memorial Lecture Quantum and semiclassical theory of chemical reaction rates", Faraday Discuss. **110**, 1–21 (1998).

[13] E. Pollak and J.-L. Liao, "A new quantum transition state theory", J. Chem. Phys. **108**, 2733 (1998).

[14] I. R. Craig, M. Thoss, and H. Wang, "Proton transfer reactions in model condensed-phase environments: Accurate quantum dynamics using the multilayer multiconfiguration time-dependent Hartree approach", J. Chem. Phys. **127**, 144503 (2007).

[15]N. Metropolis, A. W. Rosenbluth, M. N. Rosenbluth, A. H. Teller, and E. Teller, "Equation of State Calculations by Fast Computing Machines", J. Chem. Phys. **21**, 1087–1092 (1953).

[16]E. Wigner, "Calculation of the Rate of Elementary Association Reactions", J. Chem. Phys. **5**, 720–725 (1937).

[17]A. Bose and N. Makri, "Wigner phase space distribution via classical adiabatic switching", J. Chem. Phys. **143**, 114114 (2015).

[18]A. Caldeira and A. Leggett, "Path integral approach to quantum Brownian motion", Phys. A Stat. Mech. its Appl. **121**, 587–616 (1983).

[19]N. Makri, "Improved Feynman propagators on a grid and non-adiabatic corrections within the path integral framework", Chem. Phys. Lett. **193**, 435–445 (1992).

[20]M. Topaler and N. Makri, "Quasi-adiabatic propagator path integral methods. Exact quantum rate constants for condensed phase reactions", Chem. Phys. Lett. **210**, 285–293 (1993).

[21]J. Shao and N. Makri, "Iterative path integral calculation of quantum correlation functions for dissipative systems", Chem. Phys. **268**, 1–10 (2001).

[22]N. Makri and D. E. Makarov, "Tensor propagator for iterative quantum time evolution of reduced density matrices. I. Theory", J. Chem. Phys. **102**, 4600–4610 (1995).

[23]N. Makri and D. E. Makarov, "Tensor propagation for iterative quantum time evolution of reduced density matrices. II. Numerical methodology", J. Chem. Phys. **102**, 4611–4618 (1995).

[24]N. Makri, "Numerical path integral techniques for long time dynamics of quantum dissipative systems", J. Math. Phys. **36**, 2430–2457 (1995).

[25]M. Topaler and N. Makri, "Quantum rates for a double well coupled to a dissipative bath: Accurate path integral results and comparison with approximate theories", J. Chem. Phys. **101**, 7500–7519 (1994).

[26]R. Lambert and N. Makri, "Quantum-classical path integral. I. Classical memory and weak quantum nonlocality", J. Chem. Phys. **137**, 22A552 (2012).

[27]R. Lambert and N. Makri, "Quantum-classical path integral. II. Numerical methodology", J. Chem. Phys. **137**, 22A553 (2012).

[28]N. Makri, "Quantum-classical path integral: A rigorous approach to condensed phase dynamics", Int. J. Quantum Chem. **115**, 1209–1214 (2015).

[29]P. L. Walters and N. Makri, "Quantum-Classical Path Integral Simulation of Ferrocene-Ferrocenium Charge Transfer in Liquid Hexane", J. Phys. Chem. Lett. **6**, 4959–4965 (2015).

[30]R. A. Marcus, "On the Theory of Electron-Transfer Reactions. VI. Unified Treatment for Homogeneous and Electrode Reactions", J. Chem. Phys. **43**, 679–701 (1965).

[31]R. A. Marcus, "Theory of electron-transfer reaction rates of solvated electrons", J. Chem. Phys. **43**, 3477–3489 (1965).

[32]L. Chen and Q. Shi, "Quantum rate dynamics for proton transfer reactions in condensed phase: The exact hierarchical equations of motion approach", J. Chem. Phys. **130**, 134505 (2009).

[33]H. Wang, D. E. Skinner, and M. Thoss, "Calculation of reactive flux correlation functions for systems in a condensed phase environment: A multilayer multiconfiguration time-dependent Hartree approach", J. Chem. Phys. **125**, 174502 (2006).

[34]M. Topaler and N. Makri, "Path Integral Calculation of Quantum Nonadiabatic Rates in Model Condensed Phase Reactions", J. Phys. Chem. **100**, 4430–4436 (1996).

[35]A. Montoya-Castillo and D. R. Reichman, "Path integral approach to the Wigner representation of canonical density operators for discrete systems coupled to harmonic baths", J. Chem. Phys. **146**, 024107 (2017).

[36]T. Banerjee and N. Makri, "Quantum-classical path integral with self-consistent solvent-driven reference propagators", J. Phys. Chem. B **117**, 13357–13366 (2013).

[37]P. L. Walters and N. Makri, "Iterative quantum-classical path integral with dynamically consistent state hopping", J. Chem. Phys. **144**, 044108 (2016).

[38]N. Makri, "Blip decomposition of the path integral: Exponential acceleration of real-time calculations on quantum dissipative systems", J. Chem. Phys. **141**, 134117 (2014).

[39]N. Makri, "Blip-summed quantum–classical path integral with cumulative quantum memory", Faraday Discuss. **195**, 81–92 (2016).

[40]N. Makri, "Iterative blip-summed path integral for quantum dynamics in strongly dissipative environments", J. Chem. Phys. **146**, 134101 (2017).

[41]P. L. Walters, A. Bose, and N. Makri, "Iterative evaluation of the quantum-classical path integral within a quadratic treatment of the back reaction", J. Chem. Phys. to be Submitt. (2018).

Chapter 9

Conclusion

Quantum dynamics in condensed phase remains an extremely challenging and exciting field. The exponential proliferation of paths with complex weights of unit norm is the source of the dynamical "sign" problem in the path integral description. This makes it impossible to use the single most useful method for doing multidimensional integrals, namely Monte Carlo. Various approximations have been developed over the years to try to tackle this problem.

In our group, of late QCPI has been a very effective framework for doing exact quantum dynamical simulations of a system coupled to a (quasi)classical solvent. Recent developments have made it feasible to do ultrafast atomistic simulations with QCPI. However for slow reactions, following the dynamics out to the very end can be still very difficult. So, the broad starting goal was to use QCPI to calculate the rate using the equilibrium flux correlation functions. As a first step towards this goal, we started by looking at methods to calculate the Wigner function of the solvent. We first proposed the adiabatic switching Wigner method (ASW) which is an approximate method based on classical trajectories. It is extremely simple to implement and surprisingly accurate, with a nice additional feature that the ASW distribution is temporally invariant under propagation using classical trajectory. Normally the Wigner function is not invariant under classical mechanics. This causes the lack of time invariance of thermodynamic quantities, leakage of ZPE and other issues. The ASW distribution in spite of being approximate is therefore immune to these problems. We then applied the ASW method to a couple of atomistic Hamiltonians in normal modes and in Cartesian coordinates. We also looked at various spectra, invariance of thermodynamics, and compared the accuracy over a range of temperatures and anharmonicities to exact PIMC results. The ASW method seems to be very promising for cases where an approximate Wigner distribution would suffice, especially with the goal of launching classical trajectories. It would be interesting to see the use of ASW with QCPI for solvents with *ab initio* Hamiltonians in the coming future.

Returning to the problem of calculating the rate using QCPI, we could not use ASW to simultaneously equilibrate the solvent with a fully quantum system. So a new formulation of the rate theory was needed. To this end, we developed the non-equilibrium flux method, which completely got rid of the dependence on the thermal Boltzmann density operator. This allows us to start with initial conditions governed by the physics of the system, and simulate in such a manner that we can get both the pre-exponential transients and the subsequent long time rate constant. This unification of the fast and slow timescales is very important from the perspective of ultrafast reactions where the transients can in fact be essential to the dynamics. During this work, we realized that the rate is independent of the initial condition. The closer this initial condition is to the true Boltzmann density, the faster we get the rate.

Now, because we are starting from a completely non-equilibrium initial condition, we have to simulate to longer time scales. Of course this is still doable, but unnecessary when we are not interested in the transients. Utilizing this independence, we constructed a new PIMC-based density which couples the system and the solvent and very closely approximates the Boltzmann density. This is the foundation of the near equilibrium flux correlation function. We show that it gives significantly less transients than the non-equilibrium correlation function.

These methods of approximating the Wigner function of a solvent coupled with a quantum system leads back to the question — is it is possible to mitigate the "sign" problem of the Wigner transform sufficiently to allow an exact computation through Monte Carlo for a general multidimensional Hamiltonian? We realized that using the relation between Husimi function and the Wigner function, we can derive a path integral expression which can be pretty efficiently sampled by Monte Carlo and systematically converged to the exact Wigner function. This is extremely exciting for multiple reasons. Unlike in case of ASW, we no longer need a good zeroth Hamiltonian. Nor are we limited to having all degrees of freedom governed by classical mechanics. We are working on ways to use PI-Wigner to calculate the exact Wigner function for a solvent interacting with a quantum system. Applications to liquids can also prove to be very interesting.

Finally, all the methods for rate calculation that we have derived are based on QCPI. So, the bottleneck of all these methods is QCPI, speeding which up boosts all calculations, direct dynamics or rate. With solvent driven reference propagators and DCSH, QCPI is already very powerful. We worked on incorporating the blip-summation method in QCPI under the harmonic backreaction framework, which gives exponential benefit to scaling. Now the scaling of QCPI is quite comparable to that of classical molecular dynamics in cases where the system is highly coupled to the solvent. It should, therefore, now be extremely easy to use QCPI for simulating charge transfer in highly polar solvents.

The work described in this dissertation leads very easily into multiple domains of exciting research in both QCPI and quasiclassical trajectory based studies, many of which are being pursued currently.